Growth and Characterization of Cubic InGaN and InGaN/GaN Quantum Wells

Dem Department Physik

der Universität Paderborn

zur Erlangung des akademischen Grades eines

Doktors der Naturwissenschaften

vorgelegte

Dissertation

von

Shunfeng Li

Paderborn, Juni 2005

Abstract

Due to the high symmetry of the cubic III-nitride crystal unit, physical properties of the cubic III-nitrides were predicted theoretically, which are superior to those of their thermodynamically stable hexagonal counterparts. High quality c-InGaN layers and quantum structures, which form the active layers of optoelectronic devices are indispensable for realization of the highly efficient blue and green emission from c-III nitride based LEDs and Laser diodes. In this thesis, the epitaxy of high quality c-InGaN layers and InGaN/GaN wells (QWs) is optimized and the influence of various growth parameters on their structural and optical properties is investigated.

The Molecular Beam Epitaxy (MBE) of c-GaN, as well as efforts to grow thick c-GaN layers by Metal Organic Chemical Vapor Deposition (MOCVD) on top of MBE grown c-GaN buffer layers are briefly introduced. The influence of the indium and gallium fluxes on the MBE of high quality c-InGaN is studied extensively. Indium is observed to incorporate into the c-InGaN films only when the gallium flux is reduced significantly below the value needed for stoichiometric c-GaN growth. A decrease of the surface roughness of the InGaN layers and an increase of their photoluminescence intensity per unit thickness at the transition from metal-flux limited to active nitrogen-limited growth is observed. A pronounced reduction of the growth rate is observed when indium is involved in the growth. In order to explain these effects, it is supposed that excess indium atoms present on the InGaN surface due In segregation are the reason for the growth rate reduction. Based on these investigations, a recipe for the growth of high quality c-InGaN is proposed. High-resolution X-ray diffraction and Raman measurements show that InGaN layers grown on 3C-SiC substrates have better structural quality than those grown on GaAs substrates. Photoluminescence excitation (PLE) spectroscopy and photoluminescence (PL) measurements reveal that the emission from c-InGaN layers originates from highly localized structures in these layers. The room temperature PL spectra of c-$In_xGa_{1-x}N$ grown on 3C-SiC substrates are dominated by two preferential peaks at around 2.4 eV and 2.6 eV with a slight red shift with increasing x in the range of $0<x<0.2$. Depth resolved cathodoluminescence and PLE demonstrate the existence of In-rich phases, which are found by transmission electron microscopy (TEM) to be oriented along the growth direction. By thermal annealing experiments, stability of these inclusions in the c-InGaN layer is investigated, revealing that they are stable even at annealing temperatures above the growth temperatures, which allows some conclusions on the mechanism of their formation.

The PL emission intensity from c- InGaN/GaN single quantum wells is found to increase with increasing well thickness, which proves the absence of polarization fields in cubic III-nitrides. The InGaN/GaN MQWs were grown with a growth interruption after the InGaN well growth allowing excess In atoms to evaporate yielding sharp InGaN/GaN interfaces. With this growth procedure, highly efficient c-InGaN/GaN MQWs with 515nm room temperature PL emission (FWHM 240meV) and clear superlattice peaks in X-ray diffraction patterns have been realized. Finally, the effect of a c-AlGaN/GaN Bragg-mirror micro-cavity on the 520nm green emission from c-InGaN/GaN MQWs has been demonstrated for the first time.

List of Figures

Figure 2.1 Schematic drawing of MBE system 8
Figure 2.2 Ga atom flux versus the corresponding Ga BEP 9
Figure 2.3 In atomic flux versus the corresponding In BEP 10
Figure 2.4 Schematic drawing of the Philips X´Pert MRD 10
Figure 2.5 X-ray scattering geometry 11
Figure 2.6 Reciprocal space map for Bragg reflection measurements 12
Figure 2.7 Schematic drawing of photoluminescence setup 14
Figure 2.8 Schematic drawing of cathodoluminescence setup 15
Figure 2.9 Schematic drawing of photoluminescence excitation setup 16

Figure 3.1 Ga/N ratio versus substrate temperature for c-GaN growth 21
Figure 3.2 Typical HRXRD linescan on cubic GaN samples grown on GaAs and 3C-SiC substrates 22
Figure 3.3 Room temperature PL spectra of GaN layers grown on GaAs and 3C-SiC substrates 23
Figure 3.4 XRD rocking curves on c-GaN layers 24
Figure 3.5 XRD rocking curve on GaN (002) reflexes of MOCVD GaN thick buffer layer and layer after MBE GaN growth on it 25

Figure 4.1 Schematic drawing of ordered and disordered phases 29
Figure 4.2 Binodal (solid) and spinodal (dashed) curves for the $Ga_{1-x}In_xN$ system 30
Figure 4.3 Spontaneous and piezoelectric polarization field in the III-nitride and the crystal configuration 32
Figure 4.4 Band profile and carriers distribution in cubic and hexagonal InGaN/GaN quantum well 32
Figure 4.5 Reaction pathways for the deposition of In-based nitride compounds 35
Figure 4.6 RHEED patterns of c-InGaN layers 37
Figure 4.7 Transition time interval of surface reconstruction after shuttering the metal flux dependence on In flux 38
Figure 4.8 XRD ω-2θ scans of the (002)-Bragg reflex of c-InGaN/GaN/SiC samples 39
Figure 4.9 The RMS surface roughness of c-InGaN versus indium flux 40
Figure 4.10 Indium mole fraction of InGaN layers as a function of the In flux 41
Figure 4.11 a) Room temperature PL spectra of c-InGaN. b) PL peak energy and PL intensity per unit thickness as a function of the indium flux 42
Figure 4.12 Indium molar fraction of c-InGaN layers as a function of the gallium flux 43
Figure 4.13 Indium molar fraction of c-InGaN layers grown on GaAs substrate as a function of the gallium flux 44
Figure 4.14 Normalized growth rate of InGaN to GaN versus In mole fraction x 45
Figure 4.15 Schematic drawing InGaN surface reaction process and surface morphology on InGaN (001) surface 46
Figure 4.16 The 20 × 20 μm^2 typical AFM picture on surface of c-InGaN 49
Figure 4.17 The 20 × 20 μm^2 typical AFM picture on surface of GaN 49
Figure 4.18 XRD (-1-13) and (002) RSM around GaN and InGaN reflexes 50
Figure 4.19 XRD (-1-13) RSM of InGaN grown on 3C-SiC substrate and GaAs substrates 51
Figure 4.20 The calculated critical thickness of c-$In_xGa_{1-x}N$ on GaN versus the In mole fraction x 52

Figure 4.21 HRXRD ω-2θ scan on InGaN/GaN samples with different In mole fraction using GaAs substrate 54
Figure 4.22 HRXRD ω-2θ scan on InGaN/GaN samples with different In mole fraction using 3C-SiC substrates 54
Figure 4.23 Relation between the ratio of the FWHM difference of InGaN and GaN to the FWHM of GaN and the indium mole fraction 55
Figure 4.24 Transmission electron microscopy on InGaNDH1112 56
Figure 4.25 Raman spectra of c-InGaN 58
Figure 4.26 Typical Raman spectra from c-InGaN using 3C-SiC substrate #1149 and GaAs substrate #868 59
Figure 4.27 InGaN LO phonon frequency versus In mole fraction 59
Figure 4.28 Low temperature PL spectra on c-InGaN samples 63
Figure 4.29 a) 7K PL measurement on $In_{0.13}Ga_{0.87}N$#1154 by various light wavelength excitation from the lamp. B) 7K PL at excitation light of 2.54eV and PLE measurement 63
Figure 4.30 Low temperature (7K) PL spectra and PLE spectra 64
Figure 4.31 PLE measurement on $In_xGa_{1-x}N$ with different x at 7K 65
Figure 4.32 InGaN band gap versus In mole fraction x 67
Figure 4.33 Room temperature PL spectra from $In_xGa_{1-x}N$ with different x 68
Figure 4.34 PL peak energy and band gap of $In_xGa_{1-x}N$ versus In mole fraction 69
Figure 4.35 Temperature dependent PL spectra from $In_{0.06}Ga_{0.94}N$ 70
Figure 4.36 PL peak energy versus temperature from the $In_{0.06}Ga_{0.94}N$ 71
Figure 4.37 PL intensity of the 2.4 eV and 2.6 eV peaks . versus 1000/T 72
Figure 4.38 a) PL spectra of $In_{0.13}Ga_{0.87}N$ DH#1162 from 5K to 300K, b) PL peak energy versus 1000/T, the arrenhius plot, c) PL peak energy versus temperature 73
Figure 4.39 Depth resolved CL spectra on $In_{0.05}Ga_{0.95}N$ #868 74
Figure 4.40 Schematical drawing of electron distribution in the InGaN samples 75
Figure 4.41 CL emission peaks energy versus penetration depth 75
Figure 4.42 CL intensity ratio versus the electron penetration depth 76
Fig.4.43 distribution of the electron in InGaNDH#1231 at various voltages 76
Figure 4.44 Room temperature depth resolved CL spectra from InGaNDH#1231 77
Figure 4.45 CL emission peak energy versus penetration depth 78
Figure 4.46 Annealing temperature on InGaN sample versus keeping time 79
Figure 4.47 (-1-13) Reciprocal space maps on annealed sample InGaNDH#1124 80
Figure 4.48 Room temperature PL spectra before and after thermal annealing 81

Figure 5.1 Finite depth quantum well conduction band profile 83
Figure 5.2 Schematicall drawing on InGaN/GaN SQW and MQW samples 85
Figure 5.3 Room temperature PL spectra of InGaN/GaN single quantum well with different well thickness grown on GaAs substrates 86
Figure 5.4 Room temperature PL spectra of InGaN/GaN single quantum well grown on 3C-SiC substrates 86
Figure 5.5 Calculated and experimental transition energy versus with well thickness 87
Figure 5.6 Integrated PL intensity ratio of the InGaN SQW samples versus the InGaN well thickness 88
Figure 5.7 RHEED pattern of the InGaN growth, a) before growth interruption, b) after growth interruption 89
Figure 5.8 HRXRD (-1-13) reciprocal space map on InGaN/GaN MQWs 90
Figure 5.9 HRXRD (002) ω-2θscans of a) type A sample, b) type B 90
Figure 5.10 Room temperature PL spectra of the two different type of samples 91
Figure 5.11 The ω-2θ of (002) and (004) reflex of the InGaNMQW1219 92
Figure 5.12 a) XRD patterns of InGaN/GaN MQWs#1219 93

Figure 5.13 300K and 2K PL spectra of $In_{0.12}Ga_{0.88}N$ MQW#1212 94
Figure 5.14 Room temperature and 2K PL spectra of $In_{0.13}Ga_{0.87}N$MQW1213 95
Figure 5.15 Room temperature and 2K PL spectra of $In_{0.13}Ga_{0.87}N$MQW1218 96
Figure 5.16 In mole fraction and thickness of the InGaN wells versus different growth time.....97
Figure 5.17 PL peak energy versus well thickness 97
Figure 5.18 Room temperature PL spectra of $In_{0.07}Ga_{0.93}N$SQW#1111 and $In_{0.12}Ga_{0.88}N$ MQW#1212 98
Figure 5.19 Schematic layer sequence of nitride based RCLED 100
Figure 5.20 Schematic drawing of cubic AlGaN/GaN DBR 102
Figure 5.21 Reflectivity measurement and simulation results on the 15folds c-AlGaN/GaN DBR 102
Figure 5.22 The resonant cavity structure without top mirror 103
Figure 5.23 Angular dependent room temperature PL spectra of resonant cavity structure 104
Figure 5.24 Schematic drawing of the angular dependent PL measurement...............................104

List of Tables

Table 1.1 Basic parameters of hexagonal and cubic GaN 5
Table 2.1 The atomic weight, atomic number and material density of GaN and InN 15
Table 3.1 Summary of substrates for hexagonal and cubic growth and its results 20
Table 4.1 Basic physic and parameter of hexagonal and cubic InN...28
Table 4.2 Information of the c-InGaN samples for varying indium and Gallium flux.................36
Table 4.3 InGaN samples with different Ga flux by using GaAs substrates................................44
Table 4.4 Samples information of c-InGaN for characterization...48

Contents

1 Introduction 3

2 Growth and characterization methods 7
2.1 Growth methods 7
2.1.1 Molecular beam epitaxy (MBE) 7
2.1.2 Metalorganic chemical vapor deposition (MOCVD) 9
2.2 X-ray diffraction 10
2.3 Luminescence 12
2.3.1 Photoluminescence 13
2.3.2 Cathodoluminescence 14
2.4 Photoluminescence excitation spectroscopy 16

3 **Cubic GaN growth 19**
3.1 Selection of substrates for cubic GaN growth 19
3.2 Brief introduction of cubic GaN growth 19
3.2.1 Diagram of surface reconstruction transition in cubic GaN growth 19
3.2.2 Structural quality of c-GaN grown on 3C-SiC and GaAs substrates 21
3.2.3 MOCVD growth of c-GaN 23
3.2.4 MBE growth of c-GaN on MOCVD thick c-GaN layer 24

4 Growth and Characterization of cubic InGaN 27
4.1 Review of InGaN growth 27
4.2 Some remarkable issues of c-InGaN 29
4.2.1 Alloy order and disorder 29
4.2.2 Phase separation 30
4.2.3 In segregation 30
4.2.4 Polarization fields in III-nitirdes 31
4.2.5 Stokes like shift 33
4.2.6 InGaN bandgap bowing and InN bandgap 34
4.3 Competitive processes in InGaN growth 34
4.4 Cubic InGaN growth 35
4.4.1 C-InGaN growth with varying In flux 37
4.4.2 C-InGaN growth with different Ga flux 41
4.4.3 Discussion and modeling of c-InGaN growth 45
4.4.4 Determination of c-InGaN growth parameters 46
4.5 Surface properties 48

4.6 Structural properties 50
  4.6.1 Determination of the strain and In mole fraction in c-InGaN 50
  4.6.2 Critical thickness 51
  4.6.3 High resolution X-ray diffraction linescan of c-InGaN 53
  4.6.4 Transmission electron microscopy results 56
  4.6.5 Raman scattering measurements 57
4.7 Optical properties of c-InGaN 61
  4.7.1 Photoluminescence excitation spectroscopy measurement on c-InGaN 61
  4.7.2 Band gap determination of c-InGaN 66
  4.7.3 Photoluminescence measurement on c-InGaN 67
  4.7.4 Depth-resolved cathodoluminescence measurement 73
4.8 Thermal annealing results of c-InGaN 78

5 Growth and properties of c-InGaN/GaN quantum wells and application 83
5.1 Quantum size effect in finite depth quantum well 83
5.2 Sample description 85
5.3 Optical properties of single quantum well 85
5.4 Photoluminescence intensity changing with well thickness 88
5.5 Cubic InGaN/GaN multiple quantum wells 89
  5.5.1 Growth interruption in c-InGaN/GaN quantum wells growth 89
  5.5.2 Simulation of X-ray diffraction pattern 91
  5.5.3 Photoluminescence of InGaN/GaN multiple quantum wells 94
  5.5.4 InGaN/GaN multiple quantum wells with different well growth time 96
  5.5.5 Comparison of single and multiple quantum wells 98
5.6 Application of c-InGaN multiple quantum wells in a resonant cavity structure 99
  5.6.1 Resonant cavity light emitting diodes 99
  5.6.2 AlGaN/GaN distributed Bragg reflector 101
  5.6.3 Combined structure of c-InGaN/GaN multiple quantum wells and c-AlGaN/GaN distributed Bragg reflectors 103

6 Conclusions 107

Bibliography 111

Publications

Acknowledgements

Curriculum Vitae

1. Introduction

In the last decade, III-nitrides have emerged to be new promising materials for optoelectronic and electronic applications [1,2]. Due to their superior physical and chemical properties, III-nitride, i.e. GaN and its alloys have been successfully applied in new short wavelength emitting optoelectronic devices.

The emission wavelength of InN and GaN alloy covers the whole visible light range from ultraviolet to infrared [3]. Therefore, the alloy can be used as the active region of the visible light emitting diode and laser diode, which have extensive commercial applications, such as full-color screen, reading and writing on high volume digital versatile disk (DVD) and optical communication. One of the ambitious goals of scientists is to replace the conventional light sources by the highly efficient III-nitride based solid-state light sources. Up to now, a white LED with a luminous efficiency close to 80lm/W has already been demonstrated in laboratory [4], which is much higher than the conventional incandescent lamp, about 7-20lm/W. White LEDs are believed to have the potential for the luminous efficiencies exceeding 300lm/W [5]. Realization of GaN based LED as domestic luminescent light source is expected within a few years of the future. If it is done, huge amounts of energy consumption will be conserved due to its high luminous efficiency. In nitride based laser diodes application, the new, so-called “Blue ray” DVD standard has been established and will be launched later this year, 2005.

For the electronic devices, benefiting from its high melting point temperature, high breakdown voltage, GaN is believed to be suitable in high power, high frequency devices application. Due to the excellent chemical inertness and mechanical properties of III nitrides, GaN based electronic devices are suitable to work in hostile environment, for example, strong caustic environments and the outer space. The high electron mobility transistors (HEMT) [6,7] and field effect transistors (FET) [8,9] have been realized with the materials of AlGaN/GaN.

The research on GaN started in the early twenties of last century. In 1928, the first GaN powder was synthesized by Johnson through the reaction of metallic Ga and NH_3[10]. In 60’s to 70’s, more attentions were put into the research on GaN synthesis and physical properties [11]. The first GaN based device was Zn doped metal-insulating-semiconductor (MIS) light emitting diode fabricated by Pankove et al in 1971[12]. This work was based upon GaN doped with zinc and using indium contacts. It emitted at 475nm under working voltage of 60-100 Volts with very low efficiency.

The invention and application of new crystal synthesis facilities in 70’s and 80’s such as metalorganic chemical vapor deposition (MOCVD) and molecular beam epitaxy (MBE) had boosted the development of GaN research. However, quality of the III-nitride layers was still not satisfactory to the requirement of the devices. In 1986, Amano et al[13] suggested a two steps growth procedure to improve the quality of the GaN layer by inserting a low temperature AlN nucleation layer prior to the GaN growth. Nakamura et al[14] found that the GaN low temperature nucleation layer worked even better in the high quality GaN layer growth. After this breakthrough, the GaN quality was dramatically improved, which built a basis for the realization of GaN based device.

The highly efficient GaN based devices came to birth only after solving the P type doping problem. Magnesium (Mg) is the most widely used acceptor in p type doping of GaN. Amano et al[15] found that Mg atoms were activated by the low energy electrons irradiation when they used cathodoluminescence to investigate the Mg doped GaN. In 1991, Akasaki et al[16] succeeded in the first p-n homojunction blue LED with good turn-on characteristic using the treatment of low energy electron beam irradiation (LEEBI) on the Mg doped samples. In 1992, Nakamura[17] obtained the p type doping of GaN simply by annealing the as-grown Mg-doped GaN samples at 700°C-800°C in a N_2 atmosphere. The emission wavelength of this LED was 430nm with forward voltage of 4V at 20mA[18]. Nakamura suggested that the Mg atoms could be compensated by hydrogen atoms to a complex as whole in the MOCVD growth. Annealing can break these complexes and activate the Mg atoms to be acceptors. The Mg doped GaN layer grown by MBE shows p type without any post growth treatment. Now, the hole concentrations in Mg doped p type GaN have reached to an order of $10^{18}/cm^3$ [19,20]. This result paved the road for further laser diode application.

In 1997, Nakamura reported the first continuous wave InGaN/GaN multiple quantum wells blue laser diode with life time of 20-30min[21,22]. At end of 1997, the lifetime of Nakamura's laser diode had been increased to 10000 hours [23]. Up to Now, several other groups or companies have also fabricated the InGaN based laser diode using sapphire, GaN epitaxial lateral overgrowth (ELOG) template or SiC substrates [24,25].

Most of the GaN based devices are fabricated based on hexagonal (wurtzite) GaN. However, GaN can also crystallize in metastable cubic configuration (zinc-blende). Work on cubic III-nitrides is motivated by the potential advantages that these materials would offer for (opto-) electronic applications, compared to the commonly employed hexagonal nitrides, once they can be synthesized in sufficiently high quality, listed in the following:

1. Zinc-blende structure is a centro-symmetry structure. Thus no polarization exists in the cubic modification, unlike the hexagonal configuration [26].
2. A higher saturated electron drift velocity has been predicted [27] for cubic nitrides as a result of the reduced phonon scattering rate due to the higher degree of crystal symmetry.
3. A smaller electron effective mass has been reported for c-GaN [28] and a better amenability to p-type doping as well as a lower hole mass are to be expected [29].
4. Output facets of lasers can be obtained by simple cleavage in combination with technologically relevant substrates like GaAs, GaP, Si.
5. The cubic GaN has lower band gap than h-GaN. This is a benefit for the In incorporation to get long wavelength visible light emission.

The basic parameters of hexagonal and cubic GaN are shown in the following table.

	Wurtzite GaN	Zinc-blende GaN
Band gap energy	3.39eV 300K[30] 3.47eV 0K[31]	3.23eV 300K [32] 3.299 eV 0K[33]
Lattice constant (300K)	3.189 A(a) 5.186A (c) [31]	4.52 300K [34]
Debye temperature	600K	600K
Optical phonon Energies(300K)	91.2meV [31]	87.3 meV [31]
Infrared refractive Index	2.3 300 K[35]	2.3 300K [31]
Effective electron mass m_e	0.20 m_o 300 K[31]	0.13m_o 300 K[31]
Effective hole masses (heavy) m_{hh}	1.4 m_o [36]	0.84 m_o [37]
Effective hole masses (light)	0.3m_0 [36]	0.16m_o [37]
Thermal expansion coefficient	5.59×10^{-6} K^{-1}, a 3.17×10^{-6} K^{-1} c [38]	
Electron affinity		4.1 eV 300 K [31]
Cohesive energy		8.96 eV (calculated) [39]

Table 1.1 Basic parameters of hexagonal and cubic GaN

Due to the potentially good physical properties of cubic III nitride, researchers are continuously working on growing high quality cubic III nitride [40,41]. However, there are difficulties, which inhibit the development of cubic III nitrides and device application.

1) Lack of proper substrates

Now, for cubic GaN growth, the widely employed substrates are GaAs [42,43] and 3C-SiC [44,45]. The GaAs substrate has too large lattice mismatch to cubic GaN layer (20%) despite the same crystal polarity. The 3C-SiC substrate offers less lattice mismatch to cubic GaN (3.7%). Small lattice mismatch results in low dislocation density in the epitaxial layer. However, 3C-SiC is one poly type of SiC crystals, which is difficult to achieve with high material quality. Yet another critical factor which influences the growth of cubic GaN layers is thermal expansion coefficient difference between the substrate and the c-GaN epilayer. Large thermal expansion coefficient leads to cracks when the samples are cooled down from growth temperature to room temperature, e.g. hexagonal GaN layer grown on Si substrate tends to have cracks [46].

2) Metastability of cubic III- nitrides

The cubic (zinc-blende) phase of III-nitrides is a metastable phase, which makes the high quality cubic material growth difficult. Metastability of cubic GaN demands the lower growth temperature, e.g. about 200°C lower than hexagonal GaN. Low growth temperature in c-GaN leads to insufficient diffusion of the surface adatoms, which may result in inferior structural quality compared to high temperature grown hexagonal (wurztize) GaN. Investigation on the cubic GaN growth revealed that the MBE growth of cubic GaN has to be performed at metal rich condition [40]. Otherwise, at N-rich condition the hexagonal GaN growth will occur in c-GaN growth. In contrast, hexagonal GaN can be grown at high temperature in both N rich and metal rich conditions.

In device applications, especially optoelectronic devices, InGaN alloy is a necessary material for active region in visible light emission devices. Due to the large lattice constant and binding energy differences between GaN and InN, there are many remarkable phenomena in InGaN, which make high quality InGaN growth quite difficult. Therefore, the investigation on the InGaN growth and properties is very important to realize highly efficient optoelectronic devices.

This thesis reports the work on cubic III-nitride growth, or more specifically, on the growth and characterization of cubic InGaN and c-InGaN/GaN quantum wells. Chapter 2 begins with a description of the growth and characterization methods utilized, followed by a short introduction on the c-GaN growth in Chapter 3. In chapter 4, the growth of c-InGaN layer has been investigated. A recipe for InGaN growth is proposed. Versatile experimental methods, such as X-ray diffraction, transmission electron microscopy, photoluminescence, photoluminescence excitation measurement and cathodoluminescence have been performed to reveal the optical and structural properties of the c-InGaN layer. Chapter 5 mainly includes the work about the c-InGaN/GaN quantum wells. The growth procedure has been optimized. Optical and structural properties are investigated. Application of InGaN/GaN MQWs in a resonant cavity structure has been tested. Finally, the conclusions were made in chapter 6.

2. Growth and characterization methods

This chapter begins with a brief introduction of our growth methods. For in-depth understanding on the semiconductor material, post-growth characterizations are necessary to carry out the optical and structural properties of the semiconductor material. Several characterization methods are described in this chapter.

2.1 Growth methods

The growth methods, which frequently appear in the literature for III-nitrides are molecular beam epitaxy (MBE) [47,48] and metalorganic chemical vapor deposition (MOCVD) [49].

2.1.1 Molecular beam epitaxy (MBE)

MBE is a sophisticated and widely adopted crystal growth method, which has been discussed in many textbook and papers [50]. It is a non-thermodynamic equilibrium growth method, in which the kinetic processes dominate the growth. MBE growth is normally performed with a relatively low growth temperature. Thanks to the high vacuum growth chamber, plenty of in-situ characterization tools such as reflection high energy electron diffraction (RHEED), scanning tunneling microscopy (STM) help to control the growth even with a mono-atomic layer precision and make online characterization without exposure in the air. Thus one can get good interface and sound material quality with MBE growth. Another advantage of MBE growth is that the dissociation efficiency of the N_2 molecule is not influenced by growth temperature, unlike the case of MOCVD growth, which is good for high In concentration InGaN growth.

If not mentioned, all the cubic III-nitride samples in this work were grown by Riber 32 MBE system equipped with an Oxford research CARS25 radio frequency plasma source for activated nitrogen atoms (shown in Fig. 2.1). The effusion cells are mounted onto the growth chamber between 5 to 32 degrees from the horizontal plane. A liquid-nitrogen cooled cryoshroud is used to minimize the background pressure inside the growth chamber. The typical background pressure with cryoshroud on is 10^{-10} mbar. This ensures the low background doping in the semiconductor. The loading of the sample holder is done via a load lock in order to avoid deterioration of the vacuum in the growth chamber.

Six ABN35 standard elemental sources are mounted onto the MBE growth chamber such that their axes converge on the center of the substrate in the growth position. Five ports are occupied by Ga, Al, In, Si, Mg and C sources. The beam equivalent pressure of elemental species is measured by a Bayard-Alpert gauge hooked onto the backside of the substrate manipulator. The plasma source from activated nitrogen atoms is water-cooled and operated with an inductively coupled radio frequency (RF) of 13.65 MHz at power of 130-500W. Typical flow rates of the N_2 gas were 0.2-0.7 sccm, resulting in N background pressure of about 2×10^{-5} mbar.

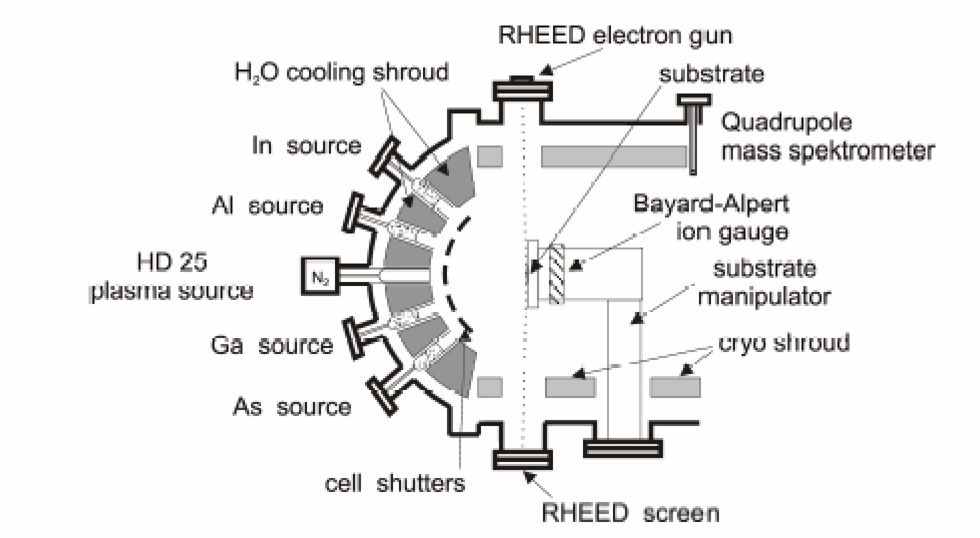
RHEED electron gun
H$_2$O cooling shroud
substrate
Quadrupole mass spektrometer
In source
Al source
Bayard-Alpert ion gauge
HD 25 plasma source
N$_2$
substrate manipulator
Ga source
cryo shroud
As source
cell shutters
RHEED screen

Figure 2.1 Schematic drawing of MBE system.

The *in-situ* RHEED is used to online check the growth. The high energy beam (with energy of 16keV) is scattered by the sample surface to a fluorescence screen. A CCD camera and computer system is employed to capture the graph and make spatial or time-dependent analysis. The rest gas level is monitored by Quadrupole mass spectrometer (QMS). Our QMS can monitor the species up to an atomic mass of 200 amu.

The 3C-SiC or GaAs substrates were cut into small pieces with size of 10×10 mm^2. The same size and substrate preparation were adopted in order to get a high reproducibility of the growth temperature between the different samples. The real temperature of growing surface was calibrated by the indium (In) and lead (Pb) melting point. Via this procedure, the relation between the thermocouple reading temperature and the real sample surface temperature during growth can be established. As a special case for GaAs substrate, the surface temperature can be calibrated also by the surface reconstruction transition from (2×4) to (3×1) at real temperature 660°C when the beam equivalent pressure (BEP) ratio of As to Ga was kept at about 13.

The BEP of metal fluxes were measured by ion gauge. The relation between the flux of the species atoms and their BEP can be expressed by the Knudsen formula:

$$\frac{F}{A} = \frac{N_{Avo} * p}{\sqrt{2 * \pi * M_{mol} * k_B * T}} \tag{2.1}$$

where p is the beam equivalent pressure, F is the flux of atoms, A is the cell aperture. M_{mol} is the mass per mole for the species. T is the source temperature.

The Ga atomic flux can be also measured by the RHEED intensity oscillation of GaAs growth at As rich condition. In this way, the relation of Ga atom flux and its corresponding BEP can be achieved. Figure 2.2 shows the flux of Ga versus its BEP.

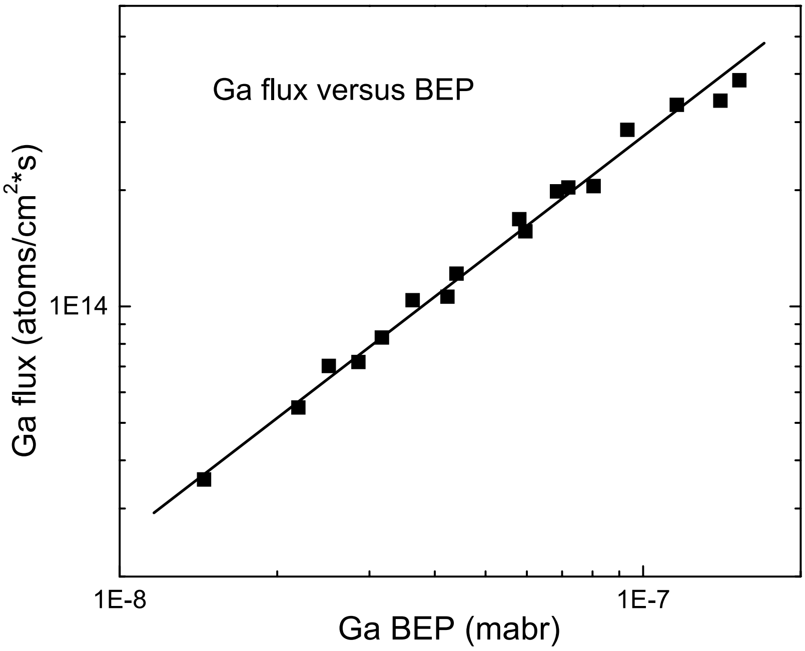

Figure 2.2 Ga atom flux versus its corresponding Ga BEP

Due to the difficulty of observing RHEED intensity oscillation in InGaAs growth, the flux of In atoms has to be calculated in another way. The determination of the atomic flux of In can be achieved by using the BEP of Ga as a calibration point. The relative sensitivity of the Bayard-Alpert ion gauge in the MBE growth chamber is dependent on the atomic number of the species, i.e. Ga, In and Al 1.7, 2.45 and 0.92 [51]. This allows the determination of the elemental flux for In versus its corresponding BEP. The flux of In atoms versus its BEP is plotted Fig 2.3.

In the following, I will use the unit of monolayer/second (ml/s), which is corresponding to the flux (atoms/cm^2/s) in a relation of $1ml/s = 9.79\times10^{14} atoms/s/cm^2$.

2.1.2 Metalorganic chemical vapor deposition (MOCVD)

In MOCVD, the substrate wafer is placed on a graphite susceptor inside a reaction vessel and heated by a radio frequency induction heater. The growth temperature depends on the type of compounds grown, for example, 1000-1100°C for h-GaN growth. Growth occurs in an atmosphere of hydrogen or nitrogen gas at a pressure of 100 to 1000 mbar. The growth precursors decompose via contact with the hot substrate and form epitaxial layers. Group V precursors are NH_3 for GaN while group III are Trimethylgallium (TMGa) or Triethylgallium (TEGa). MOCVD has advantages of high temperature and high growth rate for GaN growth over MBE. An Aixtron MOCVD equipment was used to perform cubic GaN growth at Linz University. A detailed description of this MOCVD system can be found in the Ph.D thesis of K. Schmidegg [52].

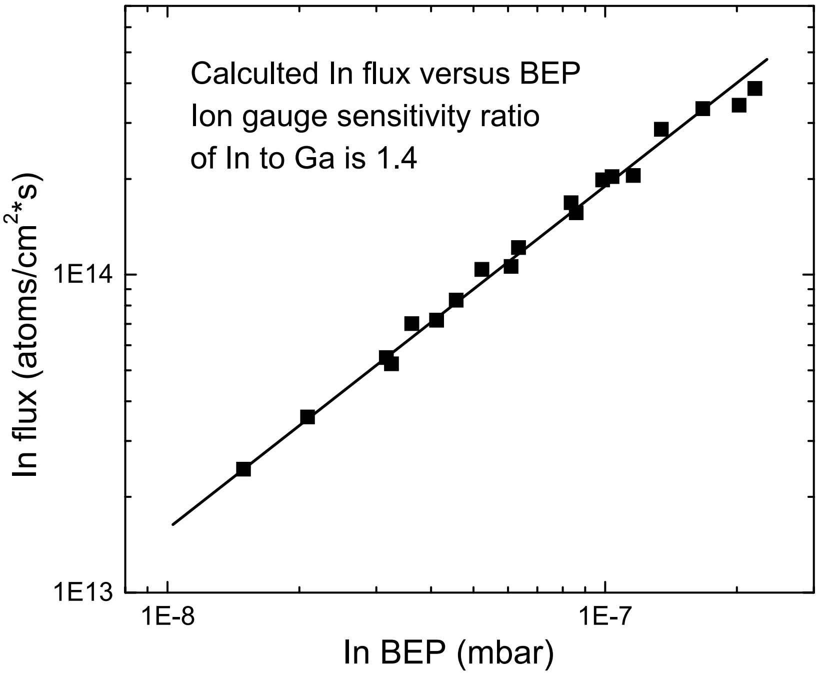

Figure 2.3 In atomic flux versus the corresponding In BEP.

2.2 X-ray diffraction

Conventional high resolution X-ray diffraction has been developed into a powerful tool for nondestructive ex-situ investigation of the epitaxial layers and structures.
The information, which is obtained from diffraction patterns, concerns the composition and uniformity of the layers, their thickness, the built-in strain and strain relaxation, and the crystalline perfection related to their dislocation density.

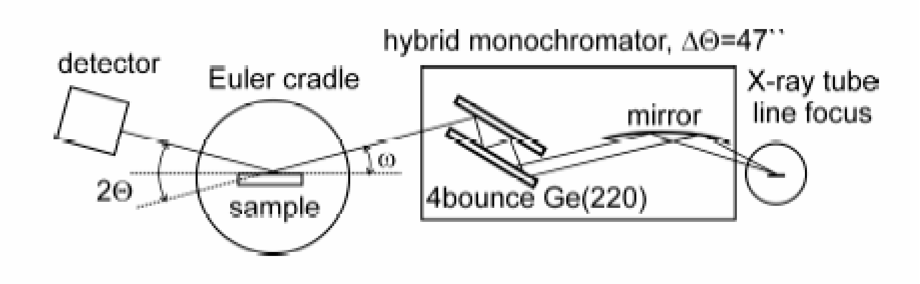
hybrid monochromator, ΔΘ=47''
detector
Euler cradle
X-ray tube
line focus
mirror
ω
2Θ
sample
4bounce Ge(220)

Figure 2.4 Schematic drawing of the Philips X´Pert MRD consisting of the X-ray tube, hybrid monochromator, Euler cradle and detector.

A Philips X'pert material research diffractometer was used in our experiments equipped with a copper anode (shown in Fig. 2.4). The $K_{\alpha 1}$ radiation from the anode at a wavelength of 1.54056Å was selected for the diffraction experiments. The hybrid monochromator was composed by a graded parabolic mirror and a (220) channel-cut Germanium crystal. This Ge crystal removes the $Cu_{K\alpha 2}$ component from the beam. The line focus combined with the hybrid monochromator gives a low beam divergence of only 47 arcsec with high intensity. The samples are mounted onto an Euler cradle, which allows an independent variation of the incident angle (ω), the diffraction angle (2θ), the angle around the surface normal (φ) and the angle around an in-plane horizontal direction (ψ). Measurements were performed with a 1/16° slit in front of the detector, called "double axis" configuration, which yields the resolution of 3 arcmin. High resolution (20 arcsec) was achieved in the so-called "triple axis" configuration with a secondary Ge (220) crystal monochromator in front of the detector.

The lattice spacing of the epitaxial layer grown on a substrate with known substrate constant is determined by the differentiation of Bragg's law:

$$\frac{\Delta d}{d_{hkl}} = -\frac{\Delta\theta}{\tan\theta_B} \tag{2.2}$$

where d_{hkl} is the known spacing of lattice plane with Miller indices (hkl) and θ_B is the corresponding Bragg angle. Δd and Δθ are the difference of the lattice constant and the diffraction angle between the known substrates and epilayers respectively. In figure 2.5, the scattering geometry is shown. φ denotes the angle between the lattice plane (hkl) and the surface. k_i is the incident and k_s is the scattered wavevector.

The Bragg diffraction is called "symmetric" if φ = 0, i.e. the diffraction planes are parallel to the surface. For φ ≠ 0, the Bragg diffraction is defined as "asymmetric".

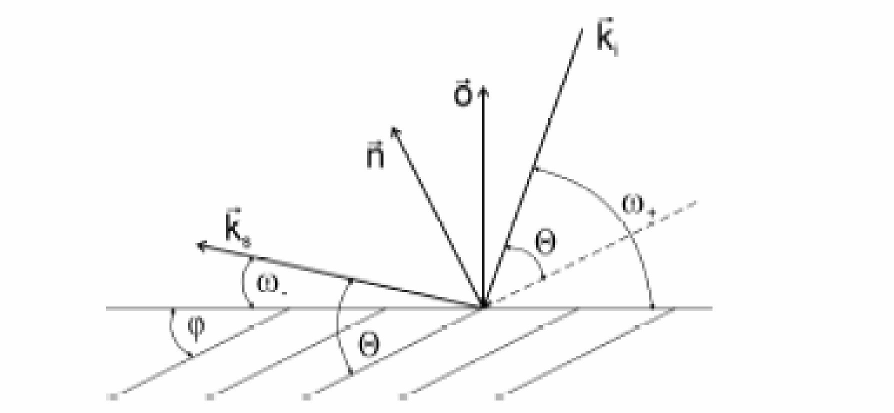

Figure 2.5: X-ray scattering geometry. $\mathbf{k_i}$: incident wavevector, $\mathbf{k_s}$: scattered wavevector, **o** : surface normal, **n** : normal on reflecting planes, Θ: Bragg angle, φ: angle between surface and reflecting plane.

The linescan modes were adopted in our routine XRD measurement, i.e. "ω-2θ scan" and "ω scan". For "ω-2θ scan", the detector is rotated twice as fast and in the same direction around the diffractometer axis as the sample. In reciprocal space, this motion corresponds to change of k_s in the following way: the tip of the vector k_s moves along the reciprocal vector G_{hkl}. During the motion, the angle ω between the incident beam and the sample surface changes. For asymmetric (hkl) Bragg reflections ($\omega = \theta \pm \varphi$, +: corresponds to high incidence angle and – to the low incidence) the corresponding ω-2θ -scan direction runs also radial from the origin (000) of the reciprocal space along G_{hkl}.

In the ω -scan, the detector is in fixed position and the sample is rotated, i.e. ω. In reciprocal space, this corresponds to a path nearly perpendicular to the equivalent *ω-2θ* -scan. The scan direction is transversal in reciprocal space and thus the so-called rocking curve is obtained.

The Ewald sphere construction and reciprocal map is shown in Fig. 2.6. G_{hkl} denotes the reciprocal lattice vector and ω is the angle between the incident wavevector k_i and the surface plane:

$$k_s = k_i + G_{hkl} \tag{2.3}$$

In the map, for example, the rocking of around (004) is the motion of the wave vector tip in the horizontal direction. Whereas, for ω-2θ scan, the tip of wave vector goes along (001) direction.

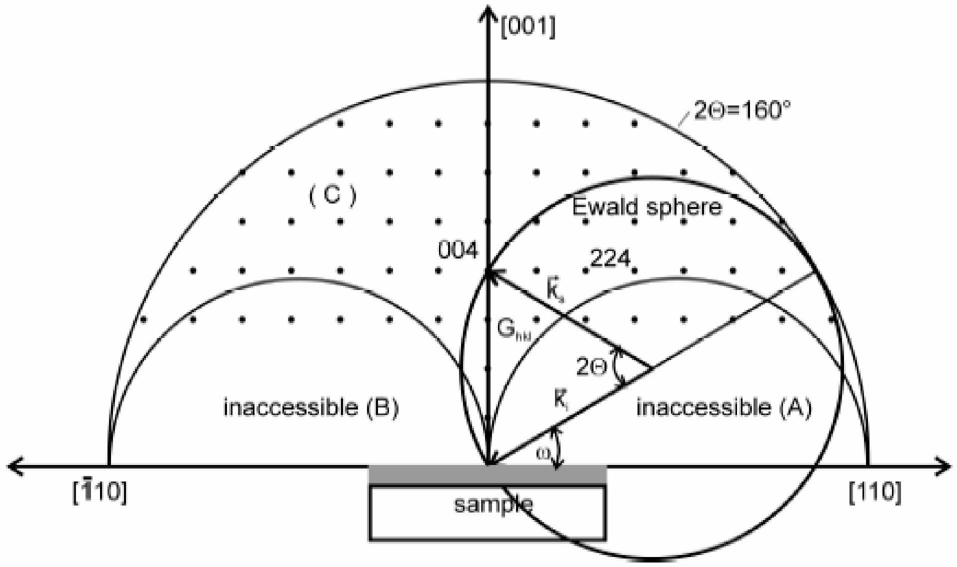

Figure 2.6 Reciprocal space map showing accessible range for Bragg reflection measurements. The radius of the outer semicircle is limited by the maximum diffractometer angle (2θ = 160°). The two inner regions defined by the two semicircles are not accessible in the Bragg case.

2.3 Luminescence

Generally, luminescence refers to emission of the electromagnetic radiation due to the recombination of excess electrons and holes generated by the external excitation. The main requirement for the luminescence emission is that the system not be at equilibrium. According to the mode of excitation, the different types of luminescence are specific in the following:

Photoluminescence (PL) —excited of excess carriers by incident photons, i.e. laser light.
Cathodoluminescence (CL) — excited by the incident electron, i.e. the electron bream in the scanning electron microscopy.
Electroluminescence (EL) — the carriers are injected through an external applied electric field.

2.3.1 Photoluminescence (PL)

PL is a routine and powerful method for characterization of direct band gap semiconductors. Through PL spectra, one can get information about the semiconductor material quality, the unintentional doping level, and the impurity energy level and so on.
The excited carriers are in non-equilibrium condition so that the carrier recombination process has to occur to reach the equilibrium with light emission. The fundamental transitions, those occurring at or near band edges are listed as follows [53]:

i. The band-to-band transition (e, h). This process is the typical interband transition that generates the intrinsic luminescence. The electrons in the conduction band directly recombine with the holes in valence band with emission of photons, which has the energy identical to the band gap of the direct semiconductor.
ii. Free exciton (X). If the material is sufficiently pure, the excited electron and hole can bind together by the Coulomb interaction into a quasi-hydrogenic exciton, which then recombine, emitting a sharp spectral line.
iii. Bound exciton. In the presence of impurities, bound exciton may be obtained. The free exciton can be localized on a neutral or ionized donor or acceptor, giving rise to the so-called exciton impurity complex. When these recombine, their emission is characterized by a narrow spectral width with lower photo energy than that of the free energy.
iv. Donor to acceptor transition (D^0, A^0). When both donor and acceptor impurities are present in the semiconductor, coulomb interaction between donor and acceptor modifies the binding energy (compared to the isolated-impurity case) such that the energy separating the paired donor and acceptor states is

$$h\nu = E_g - E_A - E_D + \frac{q^2}{\varepsilon r} \tag{2.4}$$

v. Free to bound transition. When the temperature is high enough to ionize the impurities, the low temperature donor-acceptor transition may evolve into the pure free to bound transition or spilt into two transitions, the DAP transition and free to bound transition. The peak energy position of free to bound transition is given by

$$h\nu_p = E_g(T) - E_i + \frac{1}{2}k_B T \qquad (2.5)$$

where E_i is the impurity binding energy and $\frac{1}{2}k_B T$ term results from the thermal distribution of free carriers in their bands

Our PL setup, which is shown in figure 2.7 allows the measurements of PL, as a function of the sample temperature and the excitation intensity. The luminescence is excited by the 325nm (3.815eV) line of continuous-wave He-Cd laser. A Fabry-Perot interference filter is used in order to remove the plasma line from the 325nm laser line. The laser power measured after the filter is about 4mW. The laser is then focused onto a mirror reflecting the light onto the sample fixed in the cryostat. The excited light is collected with an exit lens and dispersed in a Spex 270M monochromator equipped with a 1200 line grating and with a focal length of 27cm. The detection system consists of a GaAs photomultiplier tube and a photon counting system, controlled by a computer system. The energy resolution of this system is 0.2nm.

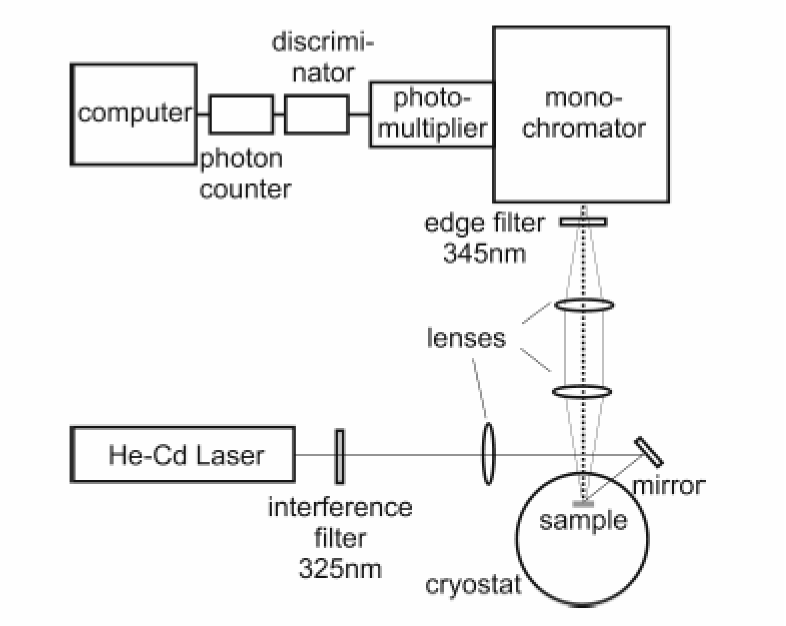

Figure 2.7 Schematic drawing of photoluminescence setup.

The cryostat allows the temperature-dependent measurement in temperature the range of 2K-300K.

2.3.2 Cathodoluminescence

The cathodoluminescence system was intensively discussed in reference[54]. A simple drawing is depicted in figure 2.8 to show our CL system. The CL is based on the Oxford CL302 light collector and a Zeiss DM950 scanning electron microscopy. The temperature can be varied from T = 70K to room temperature. The light excited by the electron beam was collected with a parabolic mirror and coupled into a UV optical fiber connected to a 50cm Spex monochromator or focused into a R457 photomultiplier for panchromatic CL imaging with sensitivity range of 160-850nm. The light was detected by a photo counting unit controlled by the computer.

By varying acceleration voltage of the electron beam, the penetration depth can be changed to get the sample information from the position with different depth. The range of electron penetration depth was estimated by the model suggested by Kanaya and Okayama[55]. The penetration depth is expressed as:

$$R_e = \frac{0.0276 * A}{\rho * Z^{0.889}} * E_b^{\ 1.67} (\mu m) \tag{2.6}$$

Where E_b is electron beam energy given in keV. A is the atomic weight in g/mol, and Z is the atomic number. ρ is the material density in g/cm^3.

In a focus mode, the excited volume can be approximated as a sphere. The vertical length of this sphere is defined as the penetration depth R_e. Defocusing the electron beam to a much larger diameter than R_e results in an excitation "cylinder" of height R_e. The values of A, Z and ρfor GaN and InN are listed in table 2.1.

Table 2.1 The atomic weight, atomic number and material density of GaN and InN.

parameters	A(g/mol)	Z	**ρ(g/cm^3)**
GaN	83.73	38	6.06
InN	128.81	46	6.76

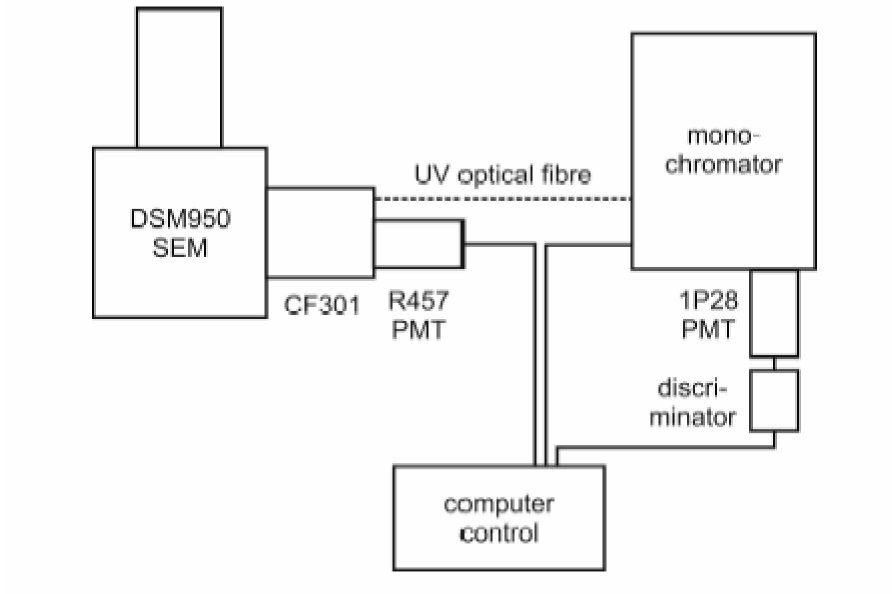

Figure 2.8 Schematic drawing of cathodoluminescence setup.

For $In_xGa_{1-x}N$, one can get the data with In mole content of x.

$$A_{In_xGa_{1-x}N} = A_{GaN} * (1-x) + A_{InN} * x \tag{2.7}$$

$$Z_{In_xGa_{1-x}N} = Z_{GaN} * (1-x) + Z_{InN} * x \tag{2.8}$$

$$\rho_{In_xGa_{1-x}N} = \rho_{GaN} * (1-x) + \rho_{InN} * x \tag{2.9}$$

2.4 Photoluminescence excitation spectroscopy (PLE)

Photoluminescence excitation is a technique combining the properties of both PL and optical absorption. The PLE system is depicted in figure 2.9. The light source is a 1000W Xe lamp. The white light from the lamp was dispersed by the monochromator A into monochromatic light, then projected on the sample in the cryostat, where the temperature can be varied from 7K to 300K. The excited light was collected and coupled to the second monochromator, B and detected by photomultipler tube. The lock-in technology has been adopted to increase the signal-noise ratio. In PLE measurement, the excitation light wavelength is tuned by the monochromator A, and the monochromator B is set at a constant wavelength position (Normally at the position of PL peak which one is interested). The excitation light with continuously varying wavelength after monochromator A shines on the sample. When the light energy is close or above the bandgap of InGaN, the excitation light can be strongly absorped and generate electron and hole pairs. The electrons and holes can recombine radiatively, then the intensity of luminescent light, which has the wavelength identical to the setting of monochromator B is recorded. Thus, the spectrum of the intensity of interested wavelength versus the energy of the excited light is obtained.

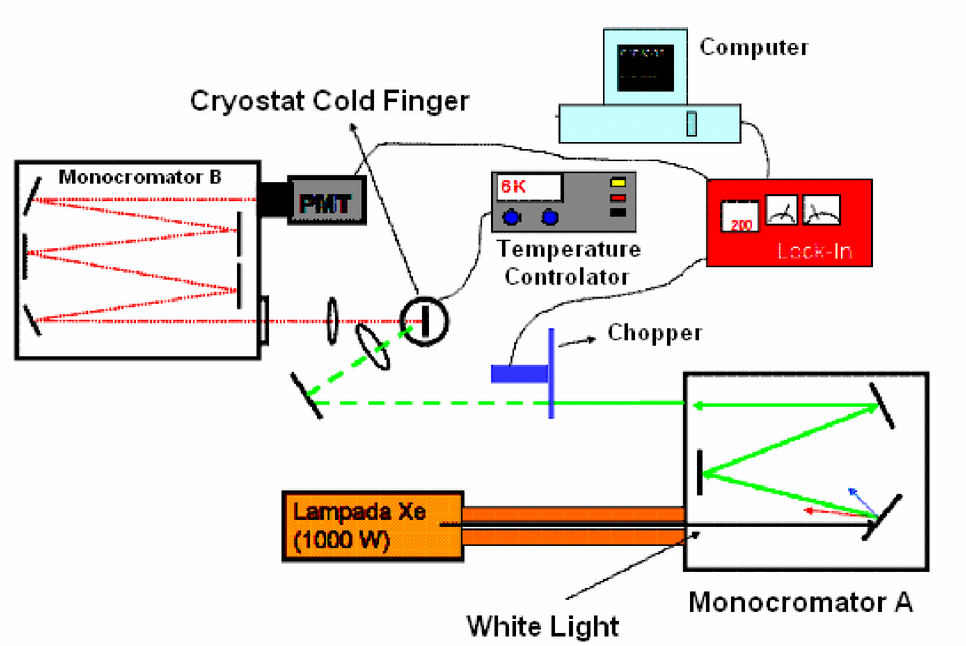

Figure 2.9 Schematic drawing of photoluminescence excitation setup.

Although the shape of the PLE spectrum mimics the shape of absorption spectrum, the intensities of the different features do not represent actual absorption strengths. Rather, they reflect the effect that such absorption has on the recombination efficiency of the PL feature on which the analyzing spectrometer is centered. Thus, absorption in regions where recombination is very efficient could, in principle, produce features in the PLE spectrum that have considerable intensity, even in cases where the volume fraction occupied by these regions is so small as to render them undetectable by other techniques, like XRD.

3. Cubic GaN growth

3.1 Selection of substrates for cubic GaN growth

Many different kinds of substrates have been used to grow nitrides, such as sapphire [1,56], 6H-SiC [57,58], Si [46], GaN [24,59], GaAs [42,60], 3C-SiC [44,45], ZnO [61,62], r-plane Al_2O_3 [63], GaP [64], MgO [65] and $MgAl_2O_4$[66,67]. The frequently used substrates in the literature are sapphire, 6H-SiC and Si for hexagonal GaN, and GaAs and 3C-SiC for cubic GaN. The substrate data, the typical GaN quality grown on it, and the advantages and disadvantages of each substrate are summarized in Table 3.1.

3.2 Brief introduction of cubic GaN growth

In our work, we use GaAs and 3C-SiC substrates for cubic GaN MBE growth. Since the InGaN layer and structures are grown on a GaN buffer layer, the GaN quality is critical for InGaN growth. Growth of GaN has been extensively discussed in the Ph.D thesis of B. Schottker[68]. Here, only some basic knowledge about cubic GaN growth is presented.

3.2.1 Diagram of surface reconstruction transition in cubic GaN growth

The cubic GaN is a metastable phase, and is grown at slightly metal rich conditions [40]. Through well-defined stoichiometric growth conditions, high purity GaN can be obtained at proper growth temperature. Therefore, the precise control of the cubic GaN growth condition is critical to achieve high quality GaN.

In MBE c-GaN growth, the nitrogen source parameters are normally kept constant during the growth. With increasing the growth temperature, the Ga atoms sticking probability decreases. More supplied Ga is needed to compensate the enhanced desorption of Ga atoms by the increasing growth temperature. When the Ga is deficit, the surface reconstruction evolves from c(2×2) at Ga rich condition to (2×2) at N rich condition. Accompanying with that, a sharp half order streak line between the main RHEED streaks will occur.

The experiments were performed on GaAs substrate. The flux of active nitrogen atoms was calculated from the c-GaN growth rate, which is calculated from the interference fringes in reflectance measurements and the growth time. The growth temperature was elevated by the temperature calibration from the GaAs growth. Nitrogen plasma source working parameters are constant, with 130W and 0.2sccm, which gave the growth rate of 70nm/h.

Table 3.1 Summary of substrates for hexagonal and cubic GaN growth and the results.

Substrate	Lattice constant and mismatch	Thermal expansion coefficient 10^{-6} °C^{-1}	FWHM of XRD rocking curve	Advantage (+) and disadvantage (-)
Sapphire (Al_2O_3)	a=0.4765nm c=1.300 16%	7.5 [69] (in-plane)	1.6arcmin[1] 1.9arcmin[56]	+ Stable at high temperature + Moderate cost -Large lattice mismatch -Insulating
6H-SiC	a = 0.3073nm c = 1.005nm 3.4%	4.3(a) 4.7(c) [70]	5 arcmin[58,71]	+High temperature + Conductive substrate
GaN	a=0.3189nm c=0.5186nm $\sim$0	5.59(a) 3.17(c) [72]	3.2arcmin (0004) [59] 20 arcsec [73]	+Lattice match + High temperature - Difficult to grow
Si(111)	0.5431nm -16.9%	2.6 [74]	11 arcmin[75] 14 arcsec[76]	+ Cheap substrate + High temperature - Large difference in thermal expansion coefficient -Non-polarity
GaAs	0.56533nm -20%	5.73 [77]	20arcmin[78] 18arcmin[79]	+Easily cleaved +Polar compound +Moderate cost +Conductive -High lattice mismatch -Unstable at high temperature
3C-SiC	0.43596nm 3.7%	3.8 [32]	>14 arcmin[80,81]	+Smaller lattice mismatch +Stable at high temperature -Difficult to get high quality material

The Ga flux was measured by GaAs growth oscillations at 600°C, in which the GaAs growth was performed at V/III BEP ratio of 13, and reasonably assuming the Ga sticking coefficient of 1. The GaN growth was initiated with a 600°C grown 5nm GaN nucleation layers, followed by 720°C grown GaN layers. Then, both the growth temperature and Ga flux were varied to achieve the stiochoimetric growth condition for cubic GaN. The transition boundary of the surface reconstruction in c-GaN growth, i.e. the relation between the growth temperature and the Ga/N ratio for stoichiometric c-GaN growth, is shown in Fig.3.1 (the original work can be found in Schikora's paper [40]).

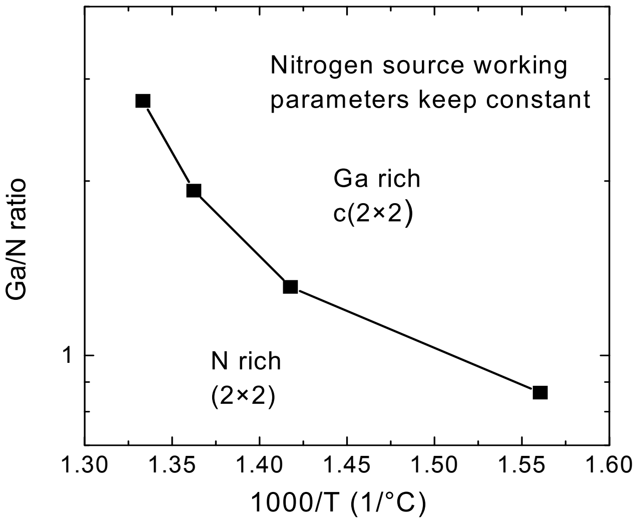

Figure 3.1 Surface reconstruction transition boundary induced by Ga/N ratio versus substrate temperature for c-GaN growth.

In stiochiometric growth condition, the Ga/N ratio decreases with the growth temperature. Apart from this line, either the metal rich or the N rich growth will occur, which will lead to surface metal droplets, rough surface, or hexagonal GaN inclusions.

3.2.2 Structural quality of c-GaN grown on 3C-SiC and GaAs substrates

In this work, two kinds of substrates, GaAs(001) and 3C-SiC(001) were used for the growth of cubic GaN. Despite the fact that 3C-SiC substrates are difficult to get, 3C-SiC substrate has some advantages over GaAs substrate. The lattice mismatch of 3C-SiC to GaN (3.7%) is much smaller than GaAs to c-GaN (20%) (table 3.1). Beside that, the 3C-SiC substrate is stable at higher growth temperature of 800°C. In the contrary, strong decomposition of GaAs substrate will occur at this temperature.

The advantages of 3C-SiC substrate deliver better quality in cubic GaN growth. Figure 3.2 shows XRD patterns on two typical GaN samples grown on 3C-SiC (#1075) and GaAs (#918), respectively. The thickness of the GaN layers were calculated from the reflectance measurements, which gave a GaN thickness of 560nm for the sample using GaAs substrate and 630nm for using 3C-SiC substrate.

Figure 3.2 (a) demonstrates the XRD ω-2θ scans around GaN (002) reflexes on both two GaN samples on GaAs and 3C-SiC substrates. GaN Bragg peak appears around 20°. Fitting by pseudo-Voigt function gives a full width of half maximum (FWHM) of 6.5 arcmin and 9.4 arcmin for GaN on 3C-SiC and GaAs, respectively. The XRD rocking curve of GaN Bragg peaks on these two GaN samples are depicted in Fig. 3.2 b). The X-ray rocking curve (XRC) FWHM of GaN on 3C-SiC substrate is 21.7 arcmin. For GaN on GaAs substrate, the XRC FWHM is 44 arcmin, which is significantly higher than GaN on 3C-SiC. The ω-2θ FWHM is believed to reflect the inhomogeneous strain, the mosaic crystal size effects along the growth direction. Beside the inhomogeneous strain and mosaic crystal size effects, the dislocation density mostly influences FWHM of the rocking curve [82]. It can be seen that less dislocation density and more homogeneous layers can be obtained by using 3C-SiC substrates. The FWHM ratio of ω-2θ scan to rocking curve is 30% for GaN on 3C-SiC and 21% for GaN on GaAs, which means the rocking curve broadening is mostly influenced by the dislocation density in the GaN layer.

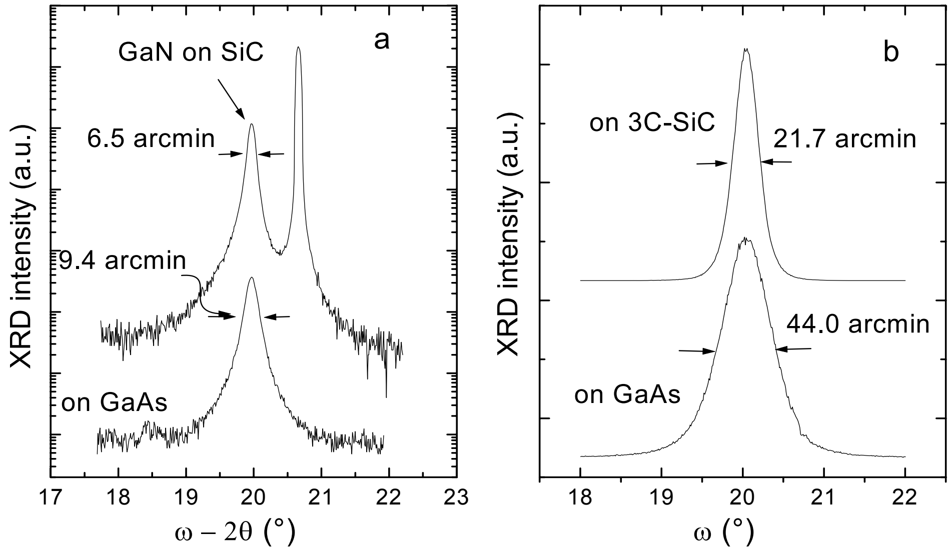

Figure 3.2 Typical HRXRD linescans on cubic GaN samples grown on GaAs and 3C-SiC substrates, respectively. a) ω-2θ scan, b) rocking curve.

The room temperature PL spectra were also measured on these two GaN samples and plotted in Fig.3.3. The upper curve is the PL spectrum of the GaN grown on GaAs substrate, and the lower spectrum comes from GaN grown on 3C-SiC. The dominant peak at 3.2eV originates from the near band gap emission of c-GaN. The peaks at 2.1eV and 2.5eV in GaN grown on GaAs substrate are due to deep level impurities. The broad peak shoulder in the PL spectrum of GaN on 3C-SiC substrate at around 2.9 eV may come from the residual carbon impurity in the GaN layer. The linewidth of GaN emission for GaN on 3C-SiC is 66meV, which is slightly smaller than GaN on GaAs substrate (78meV). The difference in FWHM of the optical emission is much smaller than the contrast in the FWHM of X-ray rocking curve, which hints that the PL emission broadening may have a different origin from the XRD peak broadening.

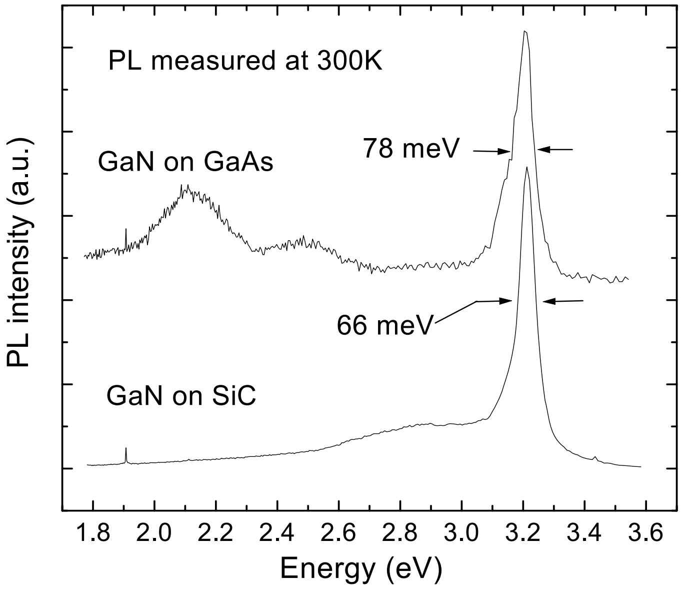

Figure 3.3 Room temperature PL spectra of GaN layers grown on GaAs and 3C-SiC substrates.

3.2.3 MOCVD growth of c-GaN

MOCVD is another important growth method for semiconductor layers. It is favored in GaN growth by its high temperature and high growth rate. Additionally, it is well known that the dislocation density in GaN decreases monotonically with increase of the layer thickness [83]. The combination of these two growth methods, MOCVD and MBE may help to get high quality thick GaN layer utilizing the advantages of both methods. In order to realize that, we performed a growth procedure as follows:

1. A thin GaN buffer was grown on GaAs substrate by MBE with a thickness of 100-450nm.
2. MOCVD epitaxy was initiated on this MBE grown c-GaN buffer layer. A thicker c-GaN layer by MOCVD growth then was obtained.
3. The MOCVD GaN thick layers then were used as buffer layers for further MBE epitaxy.

This c-GaN growth procedure allows one to take advantage of the high temperatures, and high growth rates of MOCVD with the added benefit of good surface control as seen in MBE.

A brief introduction of some experimental results will be given here. A 100 nm GaN buffer layer was initially grown by MBE. Following a 5 minute c-GaN nucleation layer growth at 570°C, the substrate temperature was risen to 720°C to grow GaN layer. This GaN layer was then put into the reactor of MOCVD equipment at University of Linz where the substrate temperature increased to 800°C at H_2 atmosphere.

From 750°C to 800°C, the NH_3 gas was delivered to the reactor for 2 minutes to etch away a thin layer of GaN thereby exposing a fresh c-GaN surface. Then c-GaN was grown with TMGa of 8 sccm and NH_3 gas of 0.5 slm, which provided a V/III ratio of 630. A more detailed description of this growth procedure may be found in ref[84].

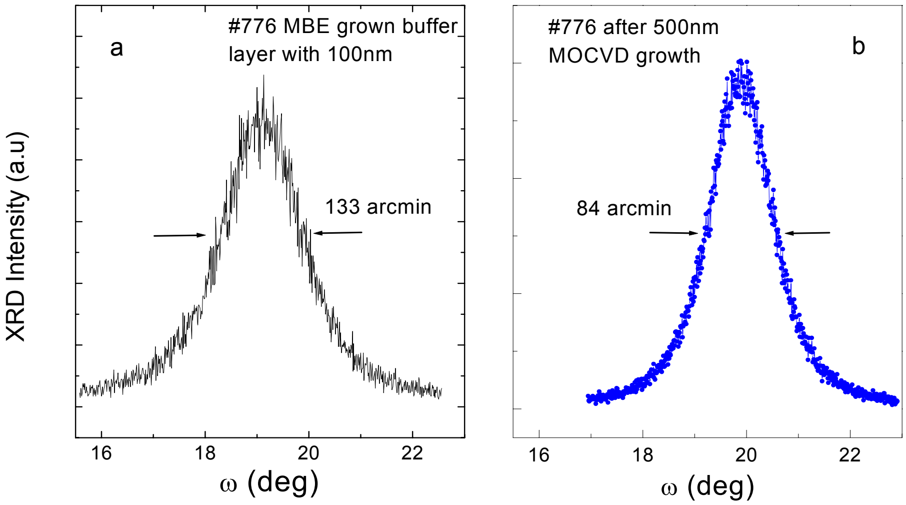

Figure 3.4 XRD rocking curves on c-GaN layers before a) and after b) MOCVD growth

In-situ optical characterization methods such as spectroscopic ellisometry and reflectometry were used to obtain growth information online. An ultra-high growth rate of 10 µm/h, which is two orders higher than MBE growth rate, was achieved and calculated from *in-situ* ellipsometry measurements. Finally a 500 nm MOCVD c-GaN layer was successfully grown on 100 nm GaN MBE buffer layer.

The HRXRD (002) rocking curves, which were measured before and after MOCVD growth are shown in Figure 3.4. The FWHM of the rocking curve decreased from 133 arcmin for 100 nm MBE c-GaN to 84 arcmin for 600 nm MOCVD c-GaN layer. The huge decrease in the FWHM signifies that the dislocation density significantly decreases due to an increasing thickness.

The rocking curve FWHM of this sample was higher than the average value from the MBE grown 600nm c-GaN layer (about 40-50 arcmin). However, after optimizing the growth, the FWHM of the c-GaN (002) rocking curve decreased to 31 arcmin (#869) with a thickness of about 1.1µm, which is in the average value of a MBE c-GaN layer of identical thickness. The growth rate for this layer, which is much lower in MBE (typically 80 nm/hr), was kept at approximately 2-3µm/h in MOCVD growth.

3.2.4 MBE growth of c-GaN on thick MOCVD c-GaN layer

We have also used MOCVD grown c-GaN layer as a substrate for MBE growth of GaN and InGaN. This MOCVD buffer layer had a thickness of 990nm.

RHEED patterns of the MOCVD growth GaN layer before MBE growth had a strongly spotty feature, indicating the rough surface of the MOCVD grown GaN layer. After the de-oxidation of the surface by the flashing Ga flux at 750°C, a 450nm MBE GaN layer was deposited followed by a 20nm InGaN layer at 630°C.

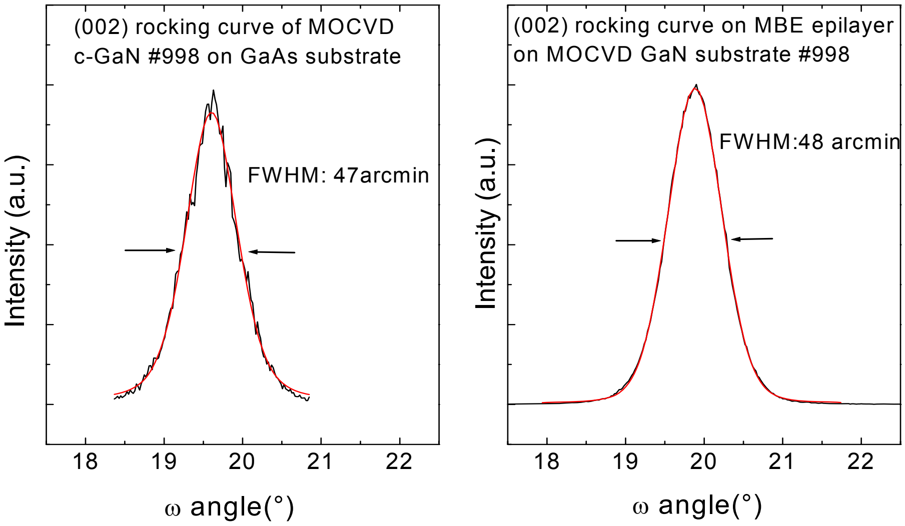

Figure 3.5 XRD rocking curve on GaN (002) reflexes of MOCVD GaN thick buffer layer and layer after MBE GaN growth on it.

At the end of MBE GaN growth, the RHEED patterns were streakier than initial readings, showing good control of surface quality by MBE growth. The XRD rocking curves of GaN by MOCVD and MBE growth are shown in figure 3.5. In the (002) rocking curve, the MOCVD grown c-GaN layer had FWHM of 47 arcmin. After MBE epitaxy on this GaN buffer, the FWHM did not decrease and kept at 48 arcmin, revealing no further decreasing of dislocation density.

The InGaN grown on this MBE/MOCVD GaN layer had comparable optical properties to the InGaN layers on the MBE grown GaN layer. All the works have demonstrated the feasibility of thick MOCVD c-GaN layers as substrates for MBE growth of c-GaN layers.

4. Growth and characterization of cubic InGaN

High quality InGaN, which acts as the active layer of the optoelectronic devices for blue, green or even yellow emission by means of tuning the indium composition, is critical for realization of high brightness LEDs and laser diodes. For this purpose, the growth and properties of InGaN based double heterostructures and quantum structures have been extensively investigated [85,1]. Although InGaN devices have been commercially realized, the growth and properties of this material still have not been well understood.

The high quality InGaN growth suffers from high volatility of In atoms, low InN binding energy, and large lattice mismatch between InGaN and GaN. Some indium related processes contribute to growth difficulties and analysis of InGaN structures, such as In segregation, InGaN phase separation and localized structure formation. Due to the metastability of the cubic III-nitrides, the c-InGaN growth has to be performed under metal-rich conditions, which further exacerbates the aforementioned problems.

The wurtzite and zinc-blende InN band gaps are still under discussion. The theoretical and experimental data of the InN band gap range from 0.6eV to 2.0eV[3]. Even with the 2.0eV of InN band gap, the InGaN with different In composition can cover the light wavelength range from red to ultraviolet. By varying the In mole fraction in InGaN layer, the highly efficient InGaN/GaN heterostructure or quantum wells can be obtained with targeted light wavelength. Some properties of hexagonal and cubic InN are listed in table 4-1.

In this chapter, after a review of InGaN growth and an introduction of other interesting topics related to InGaN, cubic InGaN growth will be discussed in detail. Also reported are results from structural and optical characterization of c-InGaN samples grown at the University of Paderborn.

4.1 Review of InGaN growth

InGaN demonstrates itself as the most mysterious material in group III-nitrides, in that many indium-induced problems makes the growth of high quality InGaN considerably difficult.

1. Low In-N binding energy. The calculated In-N binding energy is 1.93eV, which is much smaller than Ga-N (2.24eV) and Al-N binding energy (2.88eV)[39]. The weak In-N bond requires low growth temperature for In incorporation to avoid the decomposition of InGaN. From 550°C-650°C (the growth temperature used for c-InGaN MBE growth) the Indium sticking coefficient decreases from 1 to close to 0[86], which is much lower than Ga atoms in InGaN growth [87]. The cubic GaN MBE

growth temperature is about 700-750°C. In order to get significant In incorporation, the growth temperature needs to be decreased.

The low sticking coefficient of indium atoms demands high In flux for InGaN growth, which brings difficulties in controlling the stoichiometry of the InGaN growth. Indium segregation will be enhanced by high In flux, which has been proven by many researchers [88,89].

Table 4.1 Basic parameters of hexagonal and cubic InN

	InN (hexagonal)	InN (cubic)
Band gap	0.7 eV [90] 1.4 eV [91]	0.58 eV [92]
Dielectric constant (static)	15.3 , 300 K[32]	
Effective electron mass m_e	$0.11 m_o$ 300 K[93] $0.12 m_o$ Calculated effective electron mass[94]	
Effective hole masses (heavy)m_h	1.63 m_o , 300 K[95] 0.5 m_o , calculated	
Effective hole masses (light) m_{lp}	0.27 m_o , 300 K[95] 0.17 m_o , calculated	
Lattice constant	0.3533 A (a) 300 K 0.5693 A (c) 300 K [32]	0.497nm [96]
Optical phonon energy	73 meV , 300 K [32]	
Infrared refractive index	2.9 300K [32]	2.9 300K
Thermal expansion, linear	$\alpha_a = 3.8 \cdot 10^{-6}$ °C^{-1} $\alpha_c = 2.9 \cdot 10^{-6}$ °C^{-1} [32]	
Piezoelectric constant	e_{31} -0.57 C m^{-2} e_{33} 0.97 C m^{-2} [97]	

However, low In flux delivers a rough InGaN surface. Both In segregation and rough surface have to be avoided by controlling the surface stoichiometry to achieve high quality InGaN structures growth.

2. Low growth temperature tends to degrade the InGaN quality due to the insufficient diffusion of the metal atoms. By compromising between crystal quality and the In incorporation, the optimal growth temperature in MBE for cubic InGaN is set around 580°C-650°C[98,51]. Another source of growth related problems is In segregation which leads to inferior interface or surface quality which deteriorates quantum well and heterostructure growth.

3. The lattice mismatch between InGaN and GaN increases with increasing In mole fraction of InGaN. When the InGaN layer is grown thicker than the critical thickness, the strain will be relieved via generation of dislocations, which degrade the device's performance. There are several models for calculation the critical thickness of the lattice mismatch system [99,100], which will be discussed in the following text. The InN

lattice constant is a useful parameter to calculate the In composition in InGaN. Unfortunately, it is still a disputed topic up to now. There are no reliable experimental data on cubic InN lattice constant. Here, we use a InN lattice constant of 0.498nm from the theoretical calculation performed by Marques [101].

4.2 Some remarkable issues of c-InGaN

The In based III-nitrides have some extraordinary optical and structural properties. Here we briefly introduce these topics and extensively ongoing discussion.

4.2.1 Alloy order and disorder

Alloy order and disordered are both common and well studied in metallic alloy. In general, the majority of III-V ternary and quaternary alloys are predicted to be thermodynamically unstable at a low growth temperature and show a tendency towards clustering and phase separation [102,103]. Thus atomic ordering is usually not expected to occur. However such a phenomenon was theoretically predicted and observed in many III-V alloys since the middle of 1980s [104,105,106,107]. In the ordered phases, the atoms can be regularly aligned in the alloy lattice at a specific composition in a short or long range, as shown in Fig.4.1

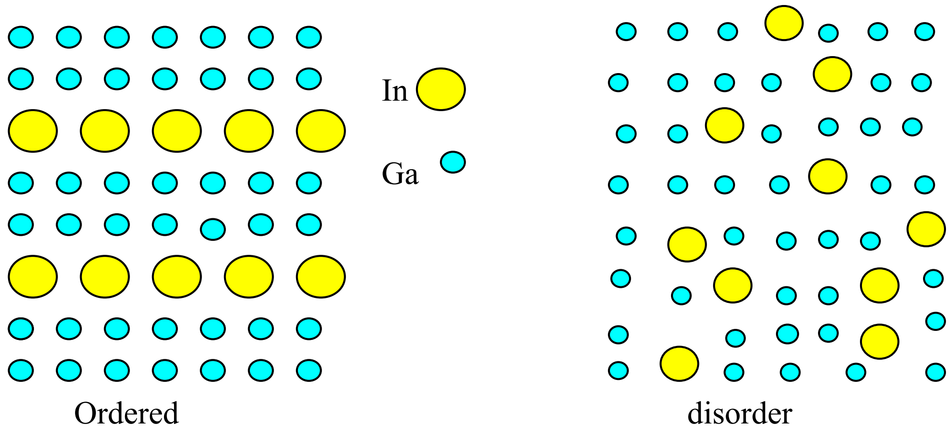

Figure 4.1 Schematic drawing of ordered and disordered phases.

The ordered phases can be detected by electron or X-ray diffraction. It shows the footprint of itself at the forbidden reflection in electron or X-ray diffraction. In the case of AlGaN, it has been shown that for some MBE growth conditions, ordering of the aluminum and gallium atoms on the metal hcp sublattice can take place [108]. It was deduced from observations of forbidden X-ray diffraction peaks in wurtzite AlGaN. Ruterana et al[109] have suggested the h-InGaN ordering phase by diffraction method in TEM. Teles et al have studied the cubic InGaN systems by combining the first-principle total energy calculations, a concentration-dependent cluster-based model and the Monte Carlo simulations. It is suggested that in the strained cubic InGaN, there are several ordered phases, which are preferentially formed in InGaN with minus excess binding energy [110]. The ordered phase with higher In composition than the In composition around it may constitute a type of strong localized structures.

4.2.2 Phase separation

Due to the immiscibility of InN and GaN, at normally employed InGaN growth temperature, it is predicted in theory that InGaN layer with high In content will separate into two phases with different In molar contents. This is called phase separation. Phase separation is a thermodynamic equilibrium process in InGaN growth. Ho and Stringfellow [111] have investigated the miscibility gap of InGaN alloy by calculating the mixing enthalpy of InN and GaN using a modified valence-force-field model. The calculated phase diagram is shown in figure 4.2. In this figure, the solid miscibility boundary is determined by the first derivative of the mixing free energy of InN and GaN, $\partial(\Delta G)/\partial x = 0$. The spinodal points (dash line) are determined by the second derivate of ΔG, $\partial^2(\Delta G)/\partial x^2 = 0$. The bimodal line surrounds the broad immiscibility region. For example, at the growth temperature of 700°C, the alloy is immiscible in the range $0.06 \le x \le 0.94$, the alloy in this range is subjected to phase separation into the $In_{0.06}Ga_{0.94}N$ and $In_{0.94}Ga_{0.06}N$ regions in thermodynamic equilibrium. Some authors have shown some experimental evidences for the existence of phase separation in InGaN by the high resolution XRD measurement [112,113].

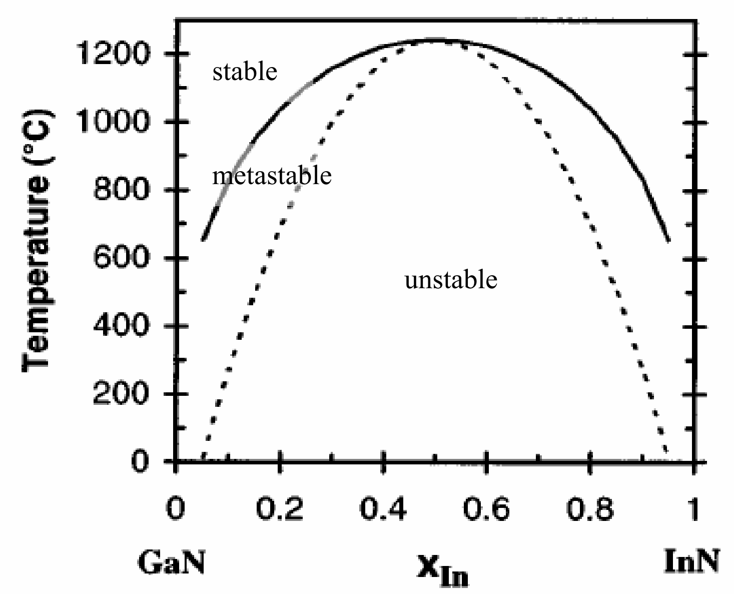

Figure 4.2 Binodal (solid) and spinodal (dashed) curves for the $Ga_{1-x}In_xN$ system, calculated assuming a constant average value for the solid phase interaction parameter. After Ho and stringfellow [111]

4.2.3 In segregation

Due to the In segregation effect, in indium based III-V compound, the ternary alloys with relative high In content may have an In content profile composed by a desired In content layer and a higher In content surface layer. Sometimes if the In content is very high, even a floating In metal layer will appear on the surface. This is known as the In segregation effect. It is argued that the bulk binding energy difference between column III atoms is the reason for the segregation effect. Elastic strain may also play an important role in the segregation process.

In Indium based III-Nitride, this effect is related to the bond length difference of GaN, AlN, and InN (i.e. largest atoms will be pushed to surface and the In atom radius is larger than that of Ga and Al atoms). The segregation process occurs in the following way: Column III atoms, i.e. Ga atoms, impinge on the growing surface and travel sizable distances to seek a lower energy configuration. The impinging atoms can exchange with surface atoms, i.e. In atoms, by thermal process (probably at defect sites). If the segregation efficiency is high, the exchange process will repeat along the growing front. This will give a thin layer (one monolayer or less) of higher In content than in the InGaN layer. In III-nitride alloys, segregation effects will be even stronger because the binding energy difference in nitrides are higher than in the arsenides and phosphides [114].

The segregation processes was found to be very sensitive to the III/V ratio and the growth temperature [88,47]. It has strong influence on the interface due to the top $In_xGa_{1-x}N$ layer having a higher x induced by surface segregation effects.

4.2.4 Polarization fields in III-nitrides

Due to non-centro-symmetric configuration and ionic binding, the h-nitrides exhibit large piezoelectric effects under strain along the c-direction, and spontaneous polarization ($\boldsymbol{P_{sp}}$) at hetero-interfaces. The genesis of the polarization is two folds: the piezoelectric effects and the difference in spontaneous polarization between AlN, GaN, and InN even in the absence of strain.

Polarization depends on the polarity of the crystal, namely whether the bonds along the c-direction are from cation sites to anion sites or visa versa. Figure 4.3 show the polarization field in hexagonal GaN, AlGaN and InGaN. In fig.4.3 a), the crystal configuration of h-GaN, the direction of Ga cation to N anion in the bond parallel to the growth direction is the same with the z direction. This polarity is said to Ga polarity. The polarity of the crystal gives rise to an internal electric field due to the interaction between Ga cation and N anion, which is called polarization field. If the strain exists in the system, it will modify the electric field by changing the spacing between Ga plane and N plane. This strain induced additional electric field is called piezoelectric field. Shown in the fig. 4.3 b) and c) is the spontaneous and piezoelectric ($\boldsymbol{P_{pz}}$) polarization field along the growth direction in h-AlGaN and InGaN. In the contrary, zinc-blende (cubic) has symmetric configuration along growth direction of (001) (shown in Fig. 4.3 d) There is no polarization field in the growth direction.

Due to the polarization field difference in GaN and InGaN, or GaN and AlGaN, the band diagram and the carrier distribution will be influenced by these electric fields.

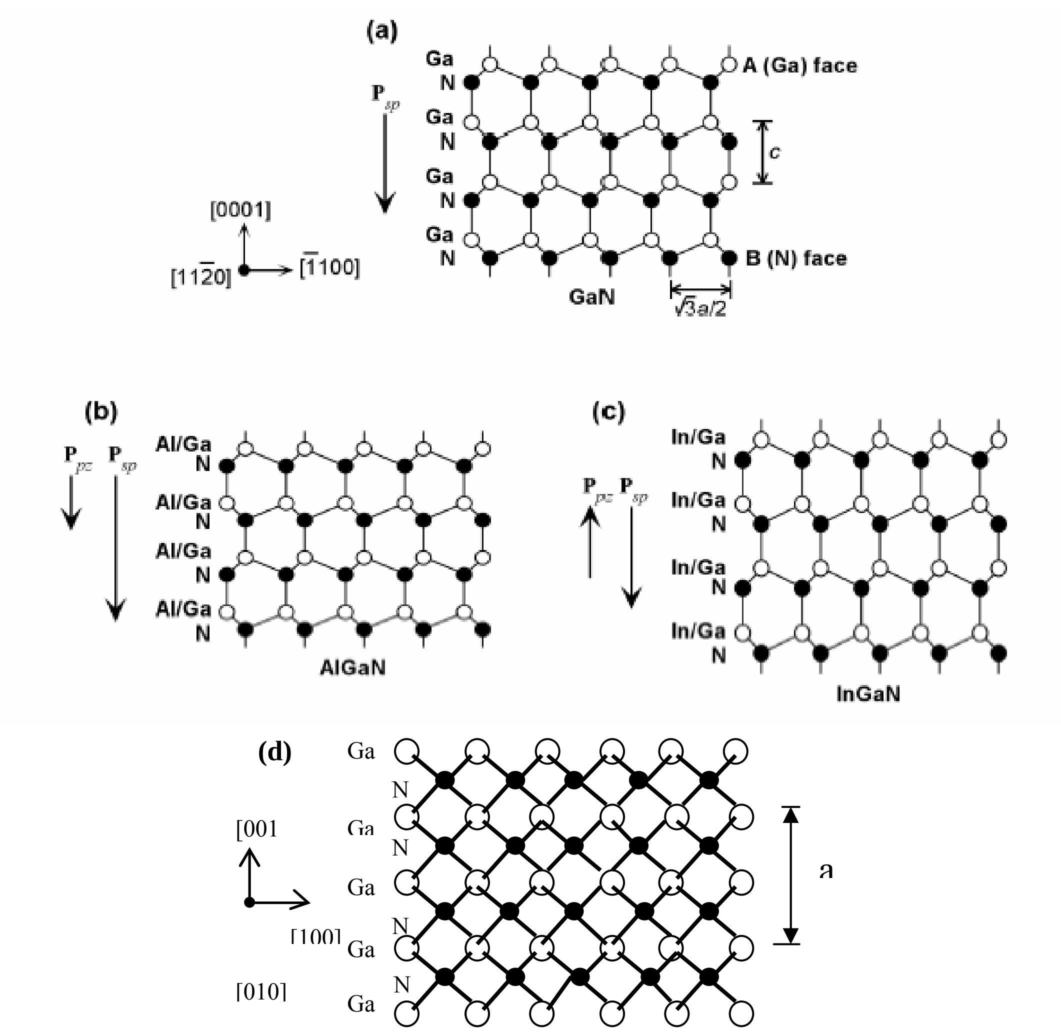
(a)
Ga
N
A (Ga) face
B (N) face
c
GaN
√3a/2
[0001]
[11$\bar{2}$0]
[$\bar{1}$100]
(b)
Al/Ga
N
AlGaN
(c)
In/Ga
N
InGaN
(d)
Ga
N
[001
[100]
[010]
a

Figure 4.3 Spontaneous and piezoelectric polarization field in the III-nitride and the crystal configuration. a) h-GaN, b)h-AlGaN, c) h-InGaN. d) Non polarization field in cubic GaN.

In the case of InGaN/GaN quantum well, the band profile and carrier distribution difference in cubic and hexagonal configuration have been shown in fig. 4.4 a) and b)

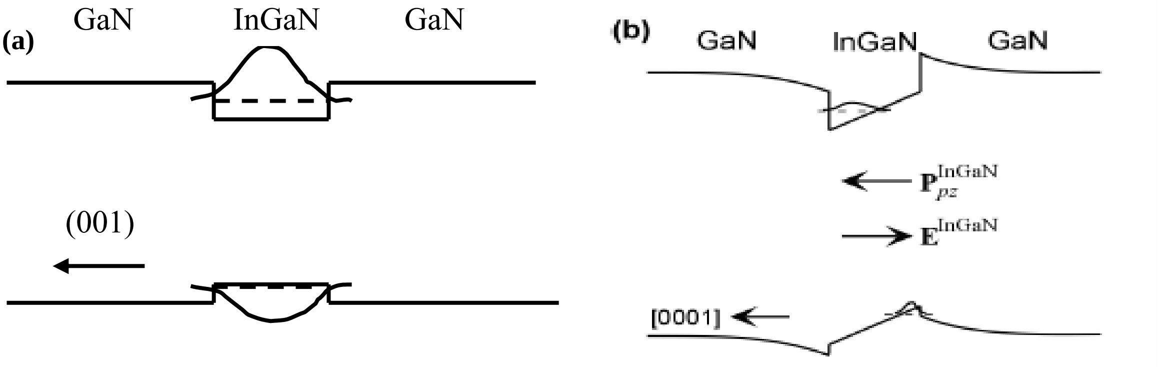
(a)
GaN
InGaN
GaN
(001)
(b)
GaN
InGaN
GaN
P_{pz}^{InGaN}
E^{InGaN}
[0001]

Figure 4.4 The band profile and carrier distributions in cubic and hexagonal InGaN/GaN quantum well, a) the cubic InGaN/GaN DH structure, b), the h-InGaN/GaN DH structure.

In hexagonal InGaN/GaN, the polarization field in GaN and InGaN wells results in a net electric field E^{InGaN}, which makes the tilt of the InGaN energy gap in the band profile and separates the electron and holes to the two opposite sides of the well. This gives rise to the lower transition energy of the electron from conduction band to valence band. Also, the wave-function overlap decreases with increasing the well thickness. This effect degrades the emission intensity with increasing the well thickness. Both effects are called quantum confinement Stark effect (QCSE). Bai et al have studied the variation of PL intensity with the well thickness [115]. They found that the PL intensity decreases monotonically with the well thickness. The intensity will totally quench with the well thickness above 5nm. The optimal InGaN well thickness is 2-3nm used in h-InGaN/GaN multiple quantum well growth[1,116]. Chichibu et al have shown that the polarization field is inactive in cubic polytypes by the time integrated and resolved PL measurement on cubic InGaN/GaN MQWs [26]. Therefore, one can expect that cubic III-nitrides will have a different PL intensity dependence on the well thickness, which is advantageous in the fabrication of cubic III-nitride based devices.

4.2.5 Stokes-like shift

The difference between Stokes line and Rayleigh scattering line in Raman scattering spectra is called “Stokes shift”. In the optical measurement of InGaN alloys, it is frequently found that PL emission peak has a red shift to absorption edge. This shift is also defined as “Stokes shift’’ or “Stokes-like shift“, which has different meaning from Raman scattering measurements. This “Stokes shift’’ is related to the strong localized properties of the luminescence.

There are many opinions to discuss the origin of Stokes shift. Firstly, due to the polarization field in hexagonal InGaN, the PL emission from quantum wells will have a red shift compared to the quantum well without polarization effect (as shown in Fig.4.4). The other more dominant influence on Stokes shift is the In concentration fluctuation. It is widely believed that localized structures with higher In concentration than its surrounding material are responsible for the light emission from InGaN. The excited electron and hole pairs relax to localized centers and recombine; on the other hand, the absorption edge which determines the InGaN band gap energy originates from the average band gap of the “homogenous” InGaN layer. This gives rise to the Stokes shift between the absorption and emission spectrum. In hexagonal InGaN, it is not possible to separate this spontaneous or piezoelectric polarization field from localization effects. It is believed that both of these effects will have influence on Stokes shift.

Due to the higher crystal lattice symmetry, in cubic InGaN, there exist no polarization fields in cubic InGaN. This gives a way to investigate the Stokes shift without the influence of the polarization field in cubic nitride system [117].

4.2.6 InGaN bandgap bowing and InN band gap

In the active region of the optoelectronic devices, the InGaN band gap determines the emission energy and influences the carriers confinement. Therefore, the bandgap of InGaN is an important parameter for the device performance and light emission wavelength of the In-based nitride devices. It has been suggested by some authors that the relation between the InGaN band gap and In mol content x does not follow a linear behavior[90,118], which can be fitted be polynomial function. This is called band gap bowing effect. The coefficient of the second order item in the polynomial function is called bowing parameter.

In the InGaN alloy, the InGaN PL emission is far below the InGaN bandgap. The PL emission is not an effective method to evaluate the InGaN band gap. Absorption spectrum, ellipsometry spectrum and photoluminescence excitation spectrum (PLE) measurements are widely performed to get the band gap of InGaN.

For the band gap bowing parameters, the InN band gap is a critical value, which is still under debate. The theoretical value of InN band gap in the 1990s was 2.0eV[3]. Due to the difficulty in pure InN growth, only a few data of the InN band gap of about 1.9eV [3] exist. However, Yoshimoto et al reported that the oxygen incorporation in InN will widen the band gap of InN and lead to a misinterpretation on the InN band gap data [119,120]. Wu et al have succeeded in the growth of hexagonal InN with reasonable quality. They proved that the band gap of InN is 0.7eV by different methods [121]. Using this value, they found a small band gap bowing of only b = 1.4eV. Up to now, there are still some arguments that InN band gap maybe higher than 0.7eV[122,123].

The accurate InN band gap is an important issue to clarify the InGaN band gap properties. Therefore, high quality InN is required for the measurement. Nevertheless, with any InN band gap between 0.6eV to 2.0eV, the InGaN alloy can cover the whole visible light emission range in the energy of 2.0eV to 3.0eV.

4.3 Competitive processes in InGaN growth

In InGaN growth, simultaneously several competitive processes occur. The salient rate processes involved are:

1. In incorporation into the ternary solid, “F_s” (atoms/cm^2/sec)
2. In atom desorption from the growth surface. “F_d” (atoms/cm^2/sec)
3. In incorporation as In metal droplets, “ F_m” (atoms/cm^2/sec)

These action pathways are illustrated schematically in Fig. 4.5. It should be noted that rate process F_d can be due to the desorption of solitary adsorbed In atoms, or breaking of the existing In-N bond. So for an indium incident flux, F_{in} (atoms/cm^2/sec), the following mass balance equation can be assumed:

$$F_{In} = F_s + F_d + F_m \tag{4.1}$$

The incorporation of In atoms into the InGaN layer is not only been determined by the input In flux. The growth temperature and the III-V stoichiometry on the growth front are also important to influence the In incorporation and crystal quality.

The InGaN growth temperature has the strongest impact on the sticking coefficient of indium atoms. T. Frey[51] estimated the In sticking coefficient varying from 0.1 to 0.0001 when the substrate temperature increases from 600°C to 700°C. It means In atoms has no incorporation when the growth close to 700°C. Adelmann et al[98] found that indium atoms can not be incorporated when the growth temperature is higher than 660°C.

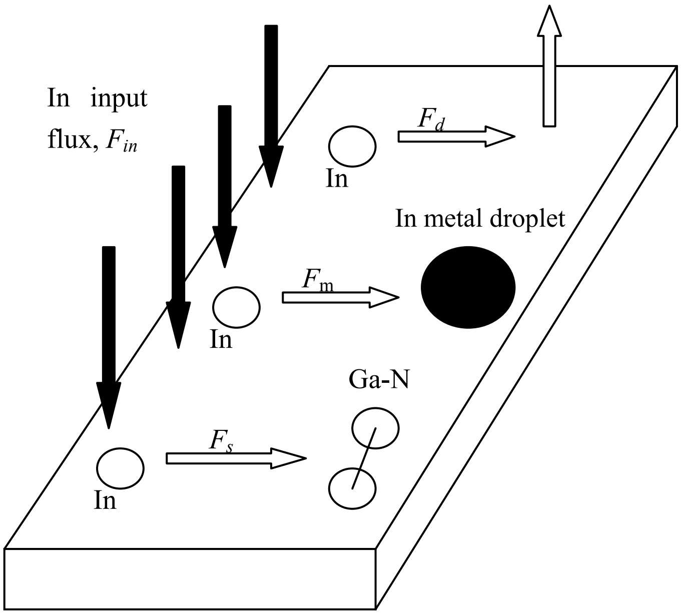

Figure 4.5 Reaction pathways for the deposition of In-based nitride compounds (after Bedair et al.1997[124]).

The high growth temperature yields a high In desorption rate and less opportunity to form In metal droplets. The desorption rate, "F_d" is inversely proportional to the residence lifetime, τ, of In on the growing surface where τ can be written as:

$$\tau = \tau_0 e^{+E_d/kT}; F_d \propto e^{-E_d/kT} \quad (4.2)$$

where τ_0 is fixed for given system and E_d is the activation energy for In desorption. The exponential temperature dependence of F_d can be dominant pathway at high growth temperature. Since the Ga atoms have a much higher sticking coefficient compared to In atoms at InGaN growth temperature, the In/Ga atoms ratio will be much smaller than that in the vapor phase. High In composition growth will require a high In flux and/or low growth temperature.

4.4 Cubic InGaN growth

In this part, the influence of In and Ga fluxes on the InGaN growth are demonstrated. After that, we will summarize the results and discuss the optimization of the InGaN growth.

Considerable efforts have been taken to optimize the growth of InGaN and obtain

in-depth understanding [125,126,127,105]. It has been found that the metal flux has a strong influence on the In-incorporation. Brandt *et al* [128] showed that In surface segregation is strongly influenced by the condition of the growth front. Nitrogen-stabilized growth yields rough interfaces of InGaN/GaN quantum wells, whereas metal-stabilized growth gives smooth interfaces and strong In segregation at the surface which leads to an increase of the well thickness. Chen *et al* [88] demonstrated the existence of stable In ad-layers on InGaN(0001) surfaces and discussed the influence of the In flux on the In incorporation. Several models were supposed to describe the In incorporation in InGaN [129,130].
As mentioned in the rate process equation 4.1, for In incorporation, the optimal In flux is critical for growing of InGaN with good optical and structural quality. There are many papers which concentrate on the In flux influence on the InGaN layer quality and interface due to the In segregation effect and In surfactant effect [88,131]
Impact of In flux on InGaN surface quality, optical and structural properties has been investigated. Both In flux and Ga flux influence on the In molar fraction x of $In_xGa_{1-x}N$ have also been studied, and a phenomenological model has been proposed to explain the x dependence on the Ga and In flux.

The GaN buffer layers were grown on 3C-SiC substrates at 700°C without a low temperature nucleation layers. Two series of InGaN layers with a thickness of about 50nm were deposited at a substrate temperature of 620°C. The first series of samples was grown at constant Ga flux of 0.036 ml/s and the In flux was varied between 0.016 ml/s and 0.1 ml/s. The second series of samples was grown with identical In flux of 0.079 ml/s and the Ga flux varying from 0.035 ml/s to 0.075 ml/s. The supplied metal fluxes and In mole fraction are shown in table 4.2. After the deposition of the InGaN layer a 35nm GaN capping layer was grown at 720°C. During all growth experiments the plasma source parameters were kept constant giving an effective N flux of 0.13 ml/s. During InGaN growth, a 5 min interruption was made after 15 min of layer growth. The growth front was monitored by *in-situ* reflection high energy electron diffraction (RHEED).

Table 4.2 Information of the c-InGaN samples for varying indium and Gallium flux.

	Ga flux (ml/s)	In flux (ml/s)	In mole fraction x
#1157	0.036	0.016	0.045
#1156	0.036	0.044	0.085
#1154	0.036	0.072	0.13
#1153	0.036	0.1	0.13
#1160	0.035	0.079	0.17
#1161	0.048	0.079	0.14
#1170	0.062	0.079	0.045
#1171	0.075	0.079	0.08

The surface of the c-InGaN layers was checked by scanning electron microscopy (SEM) and by atomic force microscopy (AFM). High-resolution X-ray diffraction

(HRXRD) was used to measure the strain and the composition of the c-InGaN layers. Room temperature photoluminescence was measured to carry out the optical properties.

4.4.1 C-InGaN growth with varying In flux

50nm thick c-InGaN layers were deposited on 600nm thick GaN buffer layers at 620°C. The In flux used in the experiments ranged from 0.016 ml/s to 0.1 ml/s, the Ga flux was kept constant at 0.036 ml/s. In this way the total metal flux (In+Ga) varied from a value lower than the flux of active nitrogen (0.13 ml/s) to one exceeding the flux of active nitrogen.

During the GaN buffer growth the RHEED pattern was streaky, indicating a 2D growth regime. After the InGaN growth was initiated, the RHEED pattern became spotty and dim indicating a 3D growth mode. When the InGaN growth was interrupted we observed a significant increase of the RHEED intensity.

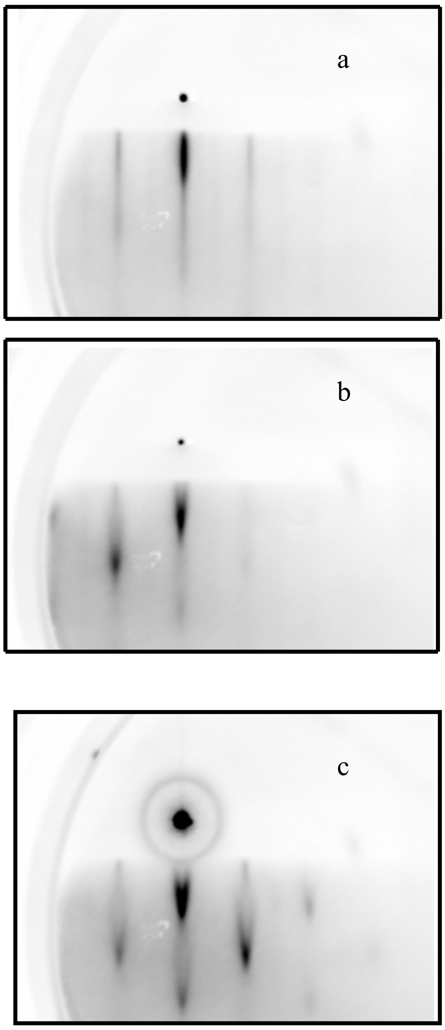

Figure 4. 6. RHEED patterns of c-InGaN layers obtained 5min after growth interruption. The indium flux was a): 0.072 ml/s, b) 0.044 ml/s, c) 0.016 mlL/s.

Figure 4.6 shows RHEED images taken at the end of the interruption. The RHEED patterns which of layers grown with a low indium flux (0.016 ml/s, 0.044 ml/s) clearly show a tendency of faceting. In contrast, the RHEED pattern of layers which were grown under high In flux (0.072 ml/s) was streaky, indicating a smooth 2D surface of the layers. The reconstruction of the surface was (4x1). Since this reconstruction is indicative for a metal deficit at the surface it is supposed that metal atoms are removed from the InGaN surface during the growth interruption [41].

When the metal sources are closed, the surface excess metal atoms will evaporate. After a few minutes of evaporation, a new (4×1) surface reconstruction appears. The transition time of surface reconstruction versus In flux has been plotted in Fig. 4.7. From In flux of 0.016ml/s to 0.16ml/s, the transition time increase with In flux. At higher In flux, the surface reconstruction can not be detected after 5 min growth interruption, which indicates the strongly excessive In metal on the surface. The longer time needed to evaporate the surface In atoms was due to the increasing In flux. This coincided with SEM measurement results, in which more indium droplets with larger size were obviously observed at higher In flux.

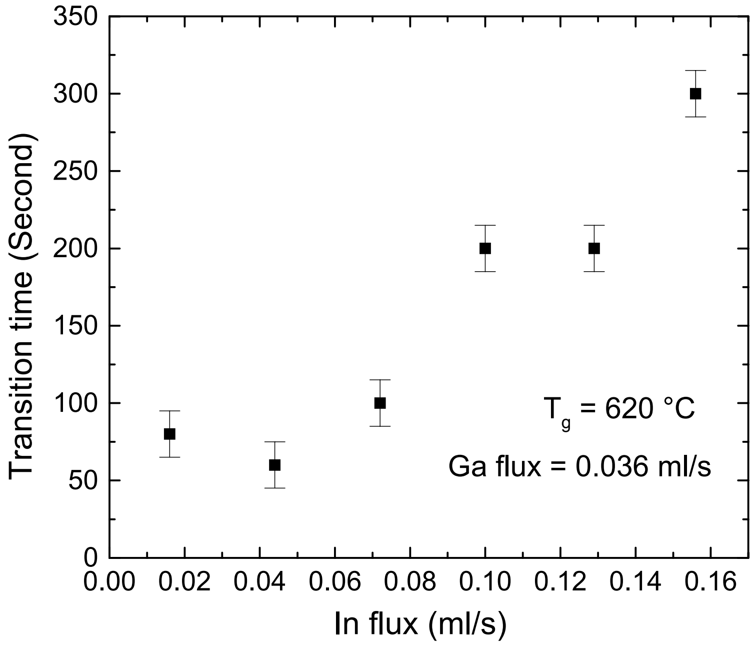

Figure 4.7 Transition time interval of surface reconstruction dependence on In flux after shuttering off the metal flux.

Figure 4.8 shows the X-ray diffraction ω-2θ scans of the c-InGaN samples close to the GaN (002) Bragg reflex. The InGaN Bragg reflex is clearly resolved and separated from the GaN peak in all diffraction patterns. The highest intensity peak originates from diffraction of the SiC substrate. The diffraction patterns of c-InGaN layers which were grown with high In flux show an additional sharp peak at about 2θ = 36.2°. The intensity of this peak increases with increasing In flux, and the peak is absent in the diffraction pattern of samples which were grown with relatively low In flux. Since the diffraction angle is close to that of cubic InN (2θ = 36.115°) or metallic indium (2θ = 36.295°) [132,133] it is difficult to distinguish between this two options. However, the diffraction peak totally disappeared when the samples were etched in chloride acid (HCl) indicating that diffraction is due to In metal on the surface rather than InN and the peak intensity can be used as a measure for the amount of In metal on surface of our c- InGaN layers.

The surface morphology of all samples was checked by SEM. It is found that only a few metal droplets on the surface of c-InGaN layers, which were grown under N-rich condition but the density and the size of the droplets on the InGaN surface increased with increasing indium flux. The droplets were analyzed by energy dispersive x-ray microanalysis (EDX). Only indium has been detected.

As-grown InGaN/GaN samples were dipped into chloride acid (HCl) for 10min to remove In droplets, then the surface roughness were measured by atomic force microscopy (AFM). The scanning area was $20 \times 20 \mu m^2$. Figure 4.9 shows the root-mean square (RMS) surface roughness versus In flux. It is obvious that the roughness of the InGaN surface decreases with increasing In flux, which is in full agreement with the RHEED results.

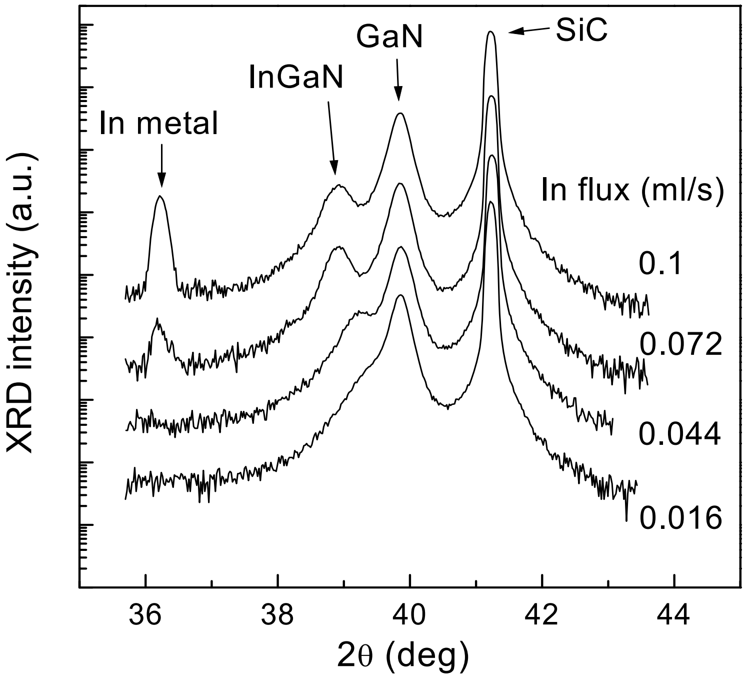

Figure 4.8 XRD ω-2θ scans of the (002)-Bragg reflex of c-InGaN/GaN/SiC samples. The InGaN layers were grown with different indium fluxes which are indicated in the figure. The gallium flux was 0.036 ml/s.

High resolution XRD reciprocal space maps revealed that the c-InGaN layers are pseudomorphically grown on the GaN buffer. The In mole fraction of these strained InGaN layers was calculated using Vegard´s rule. Figure 4.10 shows the relation between the In mole fraction and In-flux. For an In-flux below 0.072 ml/s, the In molar fraction increases monotonically. Under these conditions the growing surface has enough sticking positions for In atoms and their incorporation is then proportional to their flux.

When the In flux exceeds 0.072 ml/s no further increase of In content the is observed. The In mole fraction saturates at In flux of about 0.072 ml/s. I suppose that then the In atoms have such a high density at the surface that they can stick together and form In metal droplets. The flux of active N cannot be measured directly, however one can estimate the flux from GaN growth where *in-situ* RHEED control allows establishing stoichiometric growth conditions. From the Ga flux and the growth rate the flux of active N can be evaluated. In this way we found an effective N flux of about 0.13 ml/s. The Ga flux during InGaN growth was 0.036 ml/s and the maximal In molar faction of the InGaN layers was 13%. Thus the total metal flux incorporated (about 0.04 ml/s) was only about 30% of the active N flux indicating a pronounced reduction of the growth rate. This observation is in contrast to what has been reported for h-InGaN growth, where the rate of maximum metal incorporation at the (0001) growth front is limited by the flux of active nitrogen. [88,134]

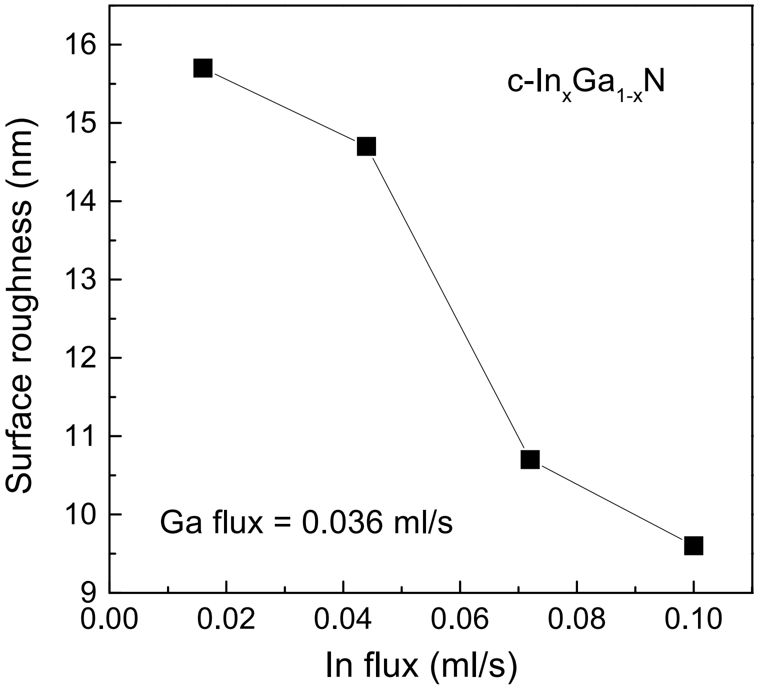

Figure 4.9 The RMS surface roughness of c-InGaN versus indium flux. The gallium flux was constant at 0.036 ml/s

Room temperature PL spectra of the c-InGaN samples are depicted in Fig. 4.11a. All spectra were measured using the same excitation intensity. It is shown that the intensity of the InGaN related emission below 2.9eV is increasing with increasing In-content. The PL spectra of the layers which were grown with an In-flux of 0.072 ml/s and 0.1 ml/s consist of a single Gaussian-like peak with line width of about 250meV. As depicted in Fig. 5b the PL intensity per unit layer thickness shows a strong increase when plotted versus the In-flux and then tends to saturate. The PL peak energy of samples with a low In content exhibits a shift of 400meV when the In molar fraction increases by only 4%. In contrast, the PL peak shift is only 10meV for the two samples grown with an In flux of 0.044 ml/s and 0.072 ml/s, respectively, where the difference of the In molar fraction is also 4.5%.

The existence of strong composition fluctuations in c-InGaN has been observed in a number of experiments [135,136,137]. In-rich clusters are formed which act as highly efficient recombination centers. Indium segregation is supposed to be one of the main processes of cluster formation. It has been demonstrated that N-rich growth can suppress the In surface segregation process [128]. So, I suppose that this may reduce the composition fluctuations and result in a low density of In-rich clusters, which may also have a lower In-content. As a consequence the radiative recombination efficiency is reduced in samples grown under N-rich conditions yielding a lower intensity per unit thickness and a higher PL emission energy.

The PL emission of samples which were grown at an In-flux exceeding 0.044 ml/s is located at about 2.4eV and shows only a weak red-shift of the peak energy with In molar fraction. We suppose that the In-rich clusters have almost identical composition independent of the In molar fraction of the InGaN layer.

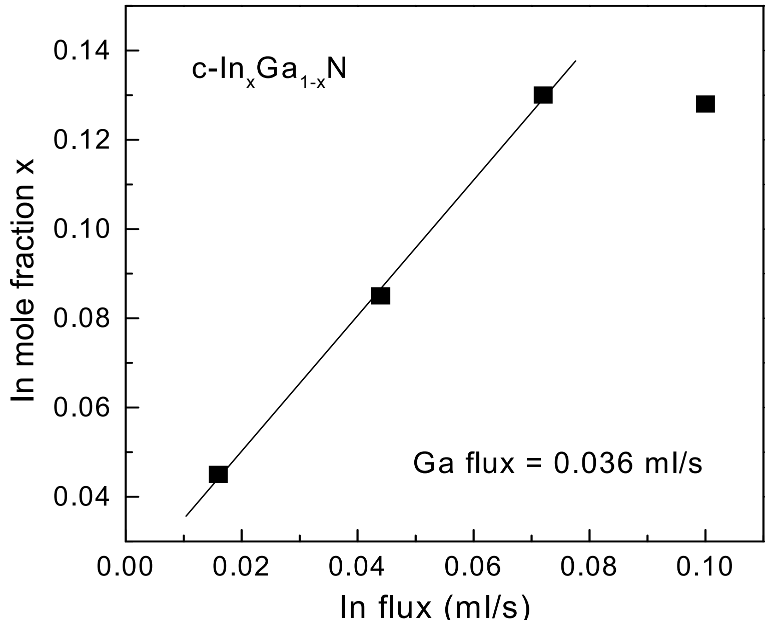

Figure 4.10 Indium mole fraction of InGaN layers grown with a fixed gallium flux (0.036 ml/s) as a function of the In flux

4.4.2 C-InGaN grown with different Ga flux

It is well established that Ga atoms have a much higher sticking coefficient than In atoms at the InGaN growth temperature. Therefore, the Ga flux can be critical for the In incorporation in MBE growth. In order to study the influence of the Ga/In flux ratio a series of c-InGaN layers was grown at 620°C. The Ga flux was varied between 0.035 ml/s and 0.075 ml/s, and the In flux was kept constant at 0.079 ml/s, the flux of active

N was 0.13 atoms/cm^{2}s. According to the results of Fig. 4 this yields metal rich growth conditions for all samples.

The In mole fraction of the layers was measured by HRXRD. Figure 4.12 shows that the In mole fraction increases linearly with decrease of Ga flux. However, if one assumes that the Ga sticking coefficient is close to one at 620°C [87] and all impinging

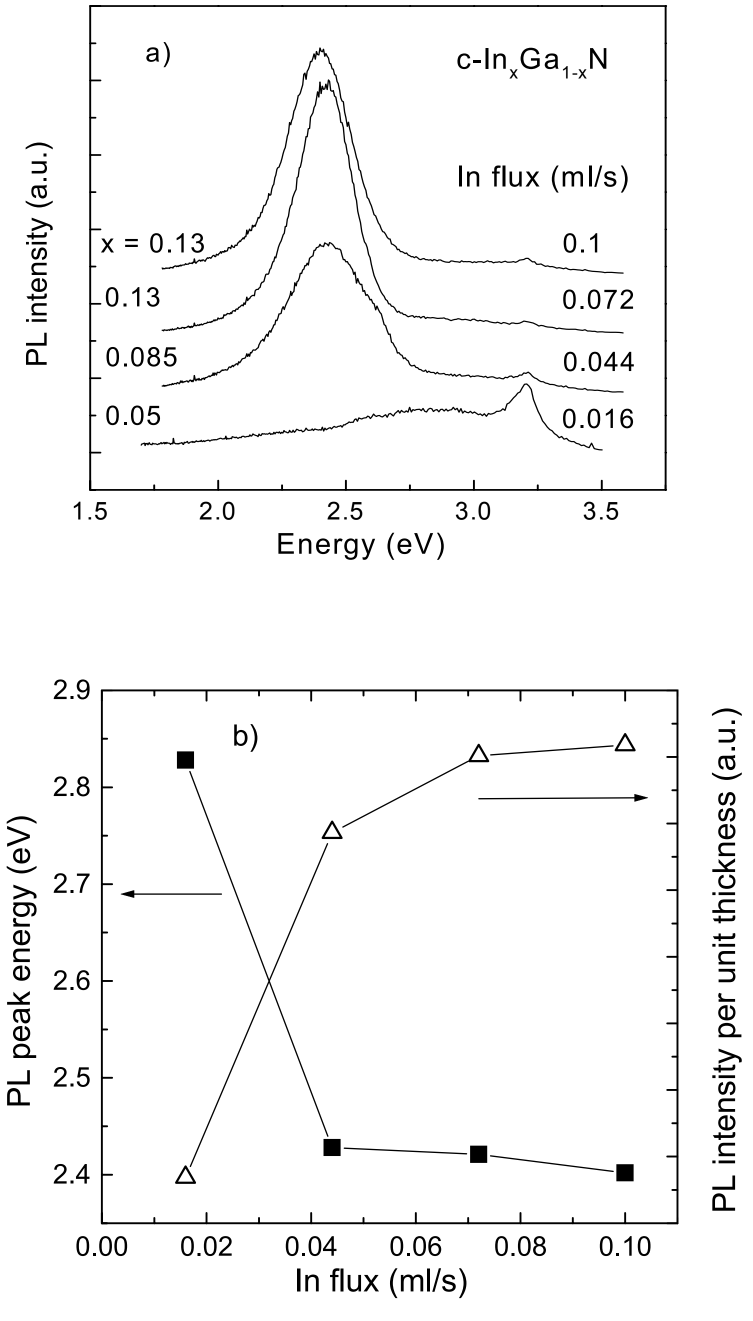

Figure 4.11 a) Room temperature PL spectra of c-InGaN. The Indium mole fraction and the indium flux are indicated. b) PL peak energy (squares) and PL intensity per unit thickness (triangles) of c-InGaN layers grown with a fixed gallium flux (0.036 ml/s) as a function of the indium flux.

gallium atoms are incorporated in the layer one can find that the total rate of metal atoms, which are incorporated is significantly lower than the rate of active N. This leads to a strong decrease of the growth rate. The growth rate, which was calculated from the measured layer thickness and the growth time was in perfect agreement with that obtained from the Ga flux and the composition of the layers. If one compares the flux of incorporated Ga and In with the flux of active N it is found that only about 1/10 of possible In-N bonds are actually formed. This result is identical to what was found when the In-flux was varied at constant Ga-flux. In the "saturation" limit (see Fig. 4) also only 1/10 of the possible In-N bonds are formed. These data suggest that during c-InGaN growth on (100) surfaces the formation of In-N is inhibited, most likely due to an In-adlayer.

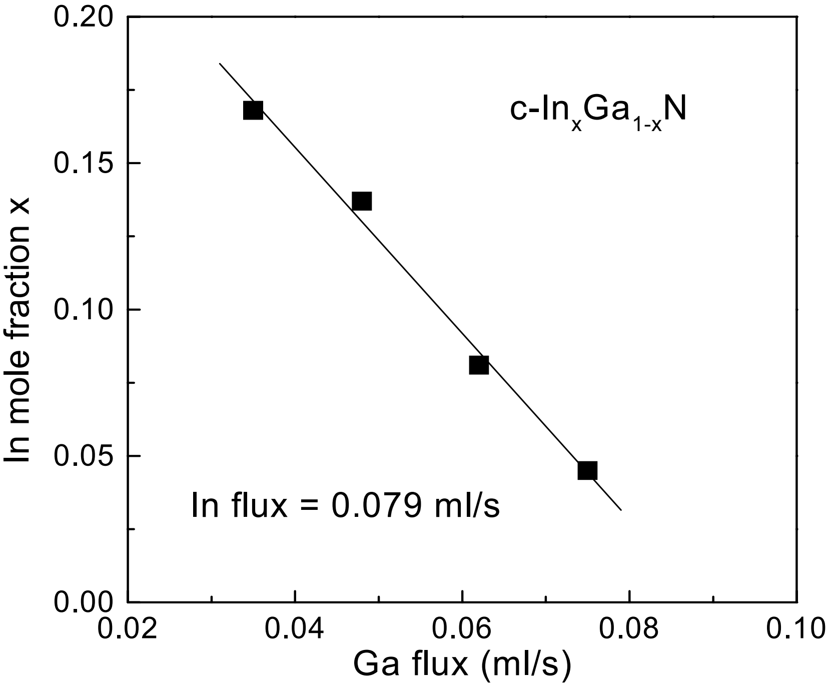

Figure 4.12 Indium molar fraction of c-InGaN layers grown at 620°C with a fixed indium flux of 0.079ml/s as a function of the gallium flux.

Based on first principles total energy calculations Neugebauer et al. [138] have proposed the existence of In adlayers on the (0001) surface of h-InGaN. I suppose that such adlayers are also formed on the (001) surface of c-InGaN. According to Chen et al[88], the incorporation rate of indium is given by f_{In} - R_{In} , where f_{In} is the incident flux of In and R_{In} is the rate of In loss either by evaporation or droplet formation. The total metal incorporation rate is given by $f_{In} - R_{In} + f_{Ga} - R_{Ga}$ where f_{Ga} is the incident flux of Ga atoms and R_{Ga} the loss rate of Ga, which is assumed to be negligible at 620°C growth temperature. The In mole fraction x is given then by

$$x = (f_{In} - R_{In}) / (f_{In} - R_{In} + f_{Ga}) \qquad (4.3)$$

Eq. 4.3 can be used to calculate R_{In} . If one inserts the flux of In and Ga which was used for the growth of c-InGaN layers with only a small amount of In-droplets at the surface one gets R_{In} = 0.072 ml/s. This value is in the same order of magnitude to that which was obtained for h-InGaN growth at the same temperature, the small difference reflects the fact that the c-InGaN is grown on the cubic GaN (001) crystal plane, which has a different density of atoms and polarity than the (0001) crystal plane of hexagonal InGaN.

If extrapolating the data in Fig. 6 to x = 0, i.e. the growth of GaN under an additional flux of In, one finds that the growth rate of GaN is reduced by about 30% due to the presence of In.

Similar experiments of InGaN growth with varying Ga flux were also performed using GaAs substrates. The substrate temperature for InGaN growth was 630°C. The In flux was kept constant at 0.15 ml/s, which resulted in a In rich growth. The Ga flux varied from 0.031 ml/s to 0.054 ml/s. The N source with constant parameters gave the active N flux of 0.076 ml/s. The growth parameter and In mole fraction are listed in table 4.3.

Table 4.3 C-InGaN samples with different Ga flux using GaAs substrates

	Ga flux (ml/s)	In flux	In mole fraction
InGaN#867	0.053	0.15	0
InGaN#868	0.041	0.15	0.05
InGaN#886	0.035	0.15	0.09
InGaN#892	0.035	0.15	0.10
InGaN#922	0.031	0.15	0.16

The relation between In mole fraction and Ga flux is plotted in Fig. 4.13.

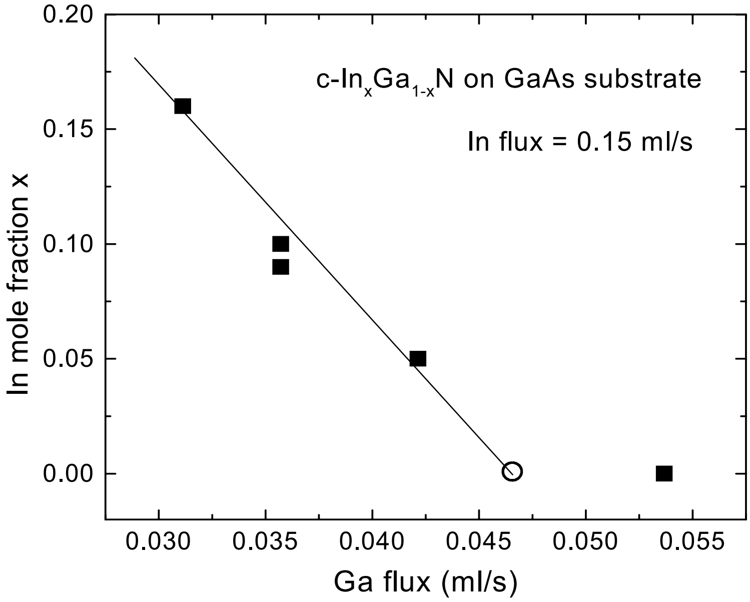

Figure 4.13 Indium molar fraction of c-InGaN layers grown on GaAs substrates at 630°C as a function of the gallium flux with a fixed indium flux of 0.15ml/s.

The same trend has also been found in the InGaN samples with different Ga flux on GaAs substrates. The extrapolated Ga flux for x = 0 is about 0.046 ml/s (circle in Fig.

1.13), which is about 60% of the supplied N flux. One additional point is shown in the graph with Ga flux of 0.052 ml/s, which is smaller than the supplied N flux, but higher than the extrapolated Ga flux with x = 0. The In mole fraction is below the detection limit, i.e. x = 0. This coincides with the extrapolation point. The decreasing of the growth rate is an unusual behavior in InGaN growth. In most of the published papers concerning h-InGaN MBE growth, no growth change was found. However, a reduction of the growth rate has been found in Adelmann's work [98] when a small In flux is used during the MBE of h-GaN at temperatures which are close to those used in our experiments.

4.4.3 Discussion and Modeling of c-InGaN growth

For clarifying the growth rate reduction effect, I plotted the growth rate ratio of InGaN to GaN at 720°C (the optimal growth temperature for GaN buffer layers) for different samples in figure 4.14. The InGaN growth rate is estimated from the whole thickness of the InGaN samples (InGaN plus GaN buffer), which is measured by reflectance, subtracted by the GaN thickness, then divided by the growth time.

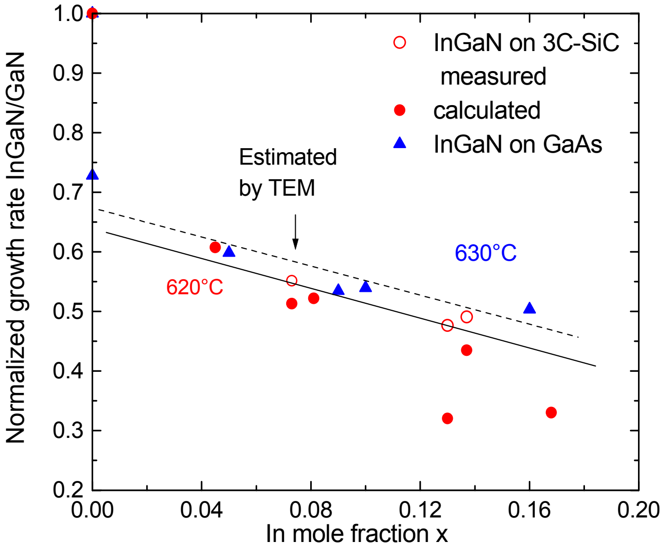

Figure 4.14 Normalized growth rate of InGaN to GaN versus In mole fraction x. .The dotted and solid lines are the guides for the eyes of the data of InGaN on GaAs (triangles) and InGaN on 3C-SiC (circles), respectively.

One sample in which the thickness is measured by transmission electron microscopy (TEM) is indicated in the graph. The growth temperature is also shown here. All the samples were grown at In rich condition to ensure that the In concentration has reached the "saturation limit". The c-InGaN growth rate was calculated from the total incorporated metal flux assuming that all the supplied Ga flux has been incorporated into the InGaN. The incorporated In flux was calculated from the In mole fraction x and pure GaN growth rate in InGaN growth. It is clearly shown that all the data from normalized InGaN growth rate are well below the unit (the GaN growth rate). The calculated data points coincide with the measured growth rate within the error. In this graph, it is shown that the relative growth rate decreases with the In molar fraction x. The extrapolation to x = 0 shows a dramatic decrease of the growth rate of about 35%. This behaviour can be interpreted by the blocking effect from the floating In metal layer existing on the InGaN surface due to the In segregation effects, as shown in Fig. 4.15. The formation of In adlayer prevents the N incorporation and makes N atoms loss from the surface. Once the In metal adlayer appears on the InGaN surface, N atoms can stick to In atoms on the surface. Due to the low In-N binding energy, the InN molecules are mobile on the surface and have chances to meet and combine into much more stable N_2 or directly evaporate from the surface (1 in Fig. 4.15). This effect results in a decrease of the effective N flux. The N atoms can incorporate into the layer via the thermal exchange with surface In atoms (2 in Fig. 4.15). On the other hand, due to the strong Ga-N bond, the Ga atoms on the surface can replace In atoms in In-N bonds (3 in Fig. 4.15). Thus at the InGaN growth temperature, nearly all the Ga atoms incorporate into the InGaN layers. The GaN growth with In coverage on the GaN surface also proves this assumption. At the GaN growth at 720°C with well-defined indium atoms coverage on the GaN surface, the growth rate of GaN has a remarkable decrease of about 25% if compared to the normal GaN growth under the same conditions.

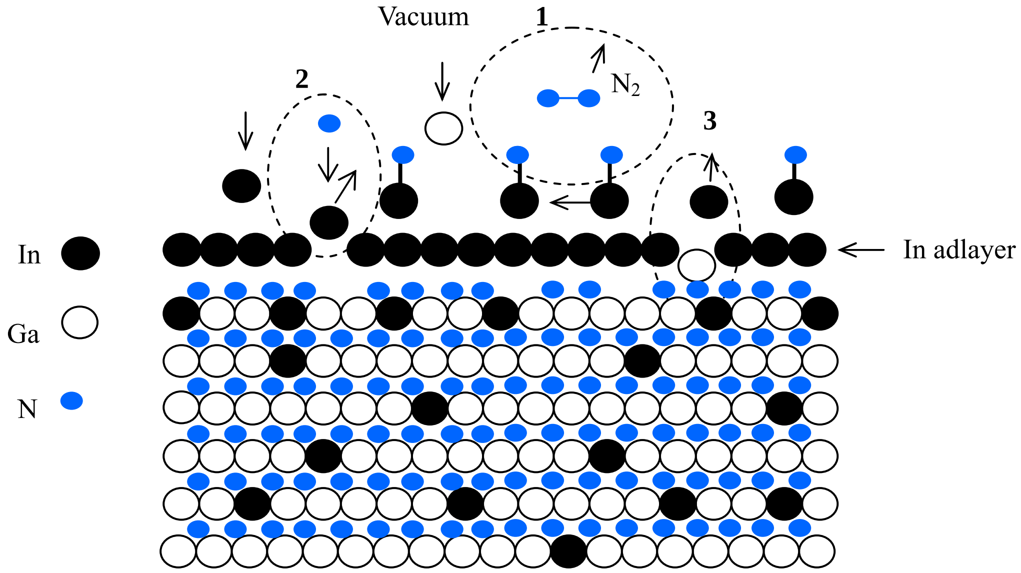

Figure 4.15 Schematic drawing of InGaN surface reaction processes and surface morphology on InGaN (001) surface. 1. N_2 formation, 2. N incorporation, 3. Ga incorporation.

4.4.4 Determination of c-InGaN growth parameters

The growth temperature also plays a critical role in InGaN growth. Adelmann et al[98] found that the InGaN growth temperature limits the indium concentration with different maximal In mole fraction at different growth temperature. At higher growth temperature than 630°C, no indium incorporation can be obtained, whereas, below 565°C, InGaN with arbitrary In mole fractions should be thermodynamically stable. I also found that it is difficult to get indium incorporation in InGaN layer with growth temperature higher than 650°C.

Once the growth temperature is determined, the metal fluxes have a dominant influence on the indium composition and the optical properties. The incorporated N flux was reduced due to the In blocking effect. For InGaN growth, the growth parameters can be determined by Fig. 4.14, which is described as follows:

1) Set the working parameters of nitrogen source for InGaN growth. The active nitrogen flux can be derived out by the growth rate of GaN at 720°C. Considering the N flux constant at different growth temperature, the nitrogen flux for the InGaN growth is identical to the flux for GaN growth.

2). In Fig. 4.14, the growth rate ratio of InGaN to GaN also denotes the incorporated total metal flux ratio of InGaN growth (In+Ga) to GaN growth (Ga). For a certain In mole fraction x, the corresponding incorporated metal flux ratio can be read out from Fig. 4.14 at a certain growth temperature. From the calculated nitrogen flux (or incorporated Ga flux) at the GaN growth temperature, the total incorporated metal (In+Ga) for InGaN growth can be carried out by the growth rate ratio. With the In mole fraction x and assuming the sticking coefficient of 1 for Ga atoms, the Ga flux and the incorporated In flux can be calculated.

3) The impinging In flux is determined by the incorporated In flux divided by the sticking coefficient of In atoms at InGaN growth temperature. InGaN layers grown under In rich growth condition have superior optical properties at saturation limitation point. Higher indium flux than the In flux at the saturation point leads to a strong In droplets formation. Therefore, the In flux should be close to the In flux where the In mole fraction saturates, e.g. 0.072ml/s in Fig. 4.10.

We have grown one InGaN sample #1329 using the above-mentioned method. The growth temperature was selected at 620°C. The In mole fraction x was designed as 0.18. Then, we got the growth rate ratio of 0.4 from Fig. 4.14. The Ga and In flux is determined by the In mole fraction and the sticking coefficient. A high quality c-InGaN sample with x = 0.17 was obtained, just coinciding with the calculation from this graph.

The surface, structural and optical properties of c-InGaN have been investigated. The information about the investigated samples in this chapter are listed in table 4.4.

Table 4.4 Samples information of c-InGaN for characterization.

Sample No.	Substrate	In mole fraction	Thickness in nm of InGaN/GaN	T_{Growth}	Strain status
InGaN#902	GaAs	0.025	100/625	650°C	Unknown
InGaN#932	GaAs	0.065	90/860	630	Unknown
InGaN#1149	3C-SiC	0.171	55/540	600°C	Partially relaxed
InGaN#1140	3C-SiC	0.098	40/390	620°C	Fully strained
InGaN#1098	3C-SiC	0.065	40/439	620°c	Fully strained
InGaN#1091	3C-SiC	0.028	40/525	630°C	Fully strained
InGaN#1147	3C-SiC	0.17	40/560	600°C	Partially relaxed
InGaN#1184	3C-SiC	0.06	65/540	620°C	Fully strained
InGaN#1329	3C-SiC	0.17	85/600	620°C	Fully strained

4.5 Surface properties

The surface and interface roughness of InGaN is an important factor in high performance device applications. In optoelectronic devices, interface roughness will degrade the confinements of MQWs and broaden the light emission. In the aforementioned experiments (Fig. 4.9), the surface roughness of InGaN decreases with In flux, indicating the In atoms are not only incorporated, but also act as surfactant.

Surfactant atoms can modify the diffusion of adatoms on the growing surface without being incorporated. For III nitride growth, the most frequently used surfactants are In, As, and H_2[139,140,141,142]. Ga atoms work as a self surfactant in GaN growth[143]. There are a great number of papers dealing with the surfactant effect. Applying the density-functional theory in combination with scanning tunneling microscopy, Neugebauer et al[138] have demonstrated that the thin metallic layer on a semiconductor surface may open an efficient diffusion channel for lateral adatom transport, i.e. adatoms prefer diffusion within this metallic layer rather than on top of the surface. They calculated the phase diagram of possible equilibrium surface reconstructions of bare and In covered GaN(0001) as a function of the In and Ga chemical potentials. At Ga rich conditions or with In surfactant, the In adlayer and Ga bilayer are stable surface structures. Further calculations of the diffusion barrier energy show that the In adlayer can strongly decrease the diffusion barrier for Ga atoms on top of the In adlayer surface from 0.7eV on the bare GaN (0001) to 0.12eV on In adlayer surface. Whereas, N adatoms prefer to sit below the top surface layer and adlayer, enhanced lateral diffusion is the dominant diffusion channel for N adatoms on the In terminated GaN (0001) surface. The diffusion barrier is 0.5eV for N atoms, which is much lower than either the barrier for N atoms diffusion on bare surface (1.3eV) or on the In adlayer surface(? 1.5eV) This is believed to be the mechanism for In surfactant and the Ga autosurfactant on the GaN(0001) surface.

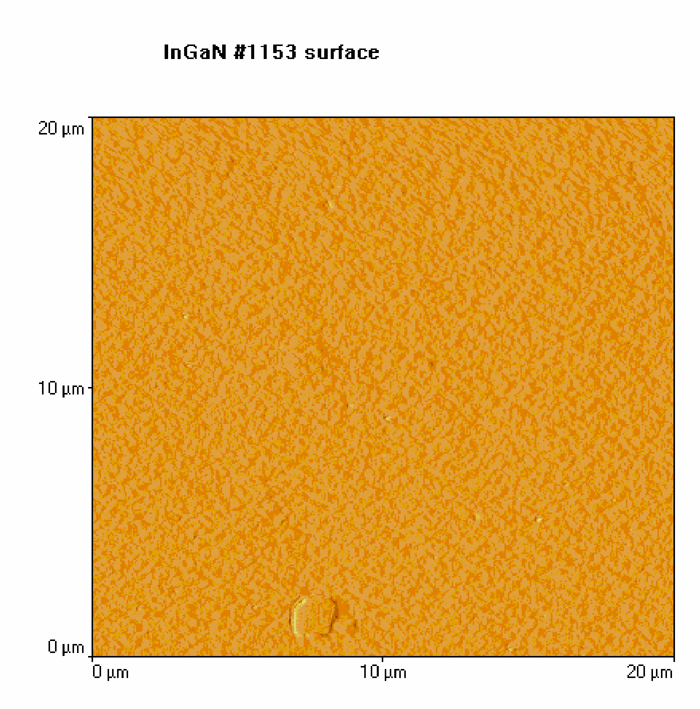

Figure 4.16 A 20 × 20 µm^2 typical AFM picture on surface of sample InGaN #1153.

One typical AFM picture of c-InGaN surface is shown in figure 4.16. The scan range in this picture is 20 × 20 µm^2. One microcrystal is seen in the lower part of this AFM picture. Beside that, a few pits which may originate from dislocation can also be detected. The dominant region of the sample surface is featureless and quite smooth, which gives a 9.6nm RMS surface roughness.

The GaN AFM surface profile is also shown in figure 4.17. The mosaic crystals appear in the AFM picture, which are absent on the InGaN sample surface. The length of the mosaic crystal is about 1 µm and the width is about 250nm. The surface RMS roughness is about 13nm.

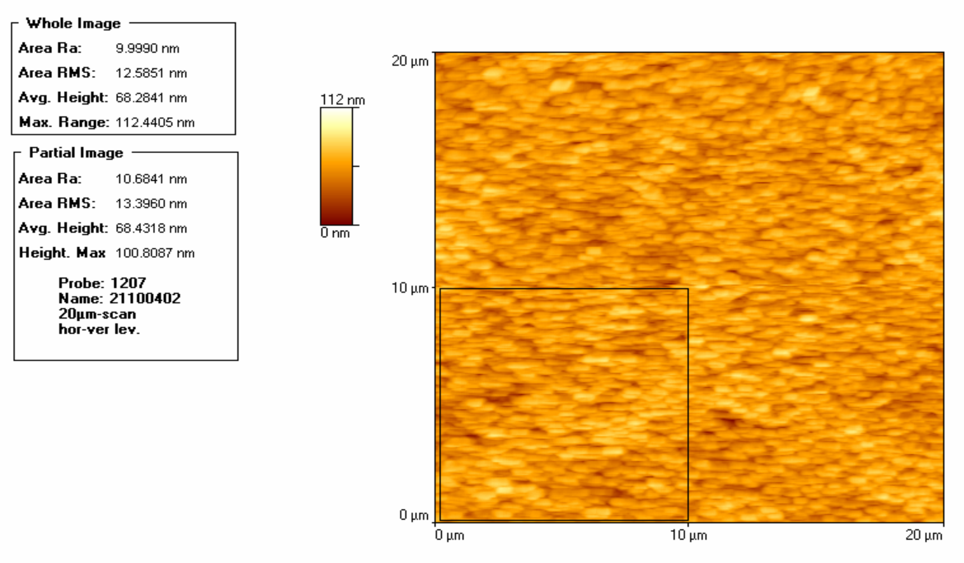

Whole Image

Area Ra:	9.9990 nm
Area RMS:	12.5851 nm
Avg. Height:	68.2841 nm
Max. Range:	112.4405 nm

Partial Image

Area Ra:	10.6841 nm
Area RMS:	13.3960 nm
Avg. Height:	68.4318 nm
Height. Max	100.8087 nm

Probe: 1207
Name: 21100402
20µm-scan
hor-ver lev.

Figure 4.17 A 20 × 20 µm^2 typical AFM picture of surface of GaN.

4.6 Structural properties of c-InGaN

4.6.1 Determination of strain and In mole fraction of c-InGaN

Structural parameters, such as crystal perfection, strain status and the In mole fraction are basic and important information for the InGaN alloy. The commonly used methods to carry out the In molar fraction are high resolution X-ray Diffraction (HRXRD), Rutherford back scattering (RBS)[144,145] , energy-dispersive X-ray (EDX)[146] and X-ray photoelectron spectroscopy (XPS) [147]. However, the RBS, EDX and XPS are destructive or more complicated methods compared to HRXRD. HRXRD is a routine method to measure the In mole fraction. It is non-destructive, easy to be used and less time consuming. Here, HRXRD has been employed for measurement of the In mole fraction and strain status.

InGaN layers are normally grown on GaN buffer layers. The lattice mismatch between InGaN and GaN leads to strain in the GaN/InGaN system. From XRD reciprocal space maps, one can evaluate the strain status of the InGaN layers. The strain status influences the estimation of the In molar content from HRXRD. Mistakes might occur if one neglects the strain conditions in the InGaN layers.

Figure 4.18 a) and b) show XRD reciprocal space maps of the (-1-13) and (002) reflexes of the InGaN/GaN sample #1147. The GaN and InGaN peaks are clearly separated and marked in these figures. The tilt of the InGaN crystal orientation to the GaN buffer layers' could lead to mistakes in the calculation of the strain status and In mole fraction if it is not properly considered. It can be estimated in the symmetric RSM, e.g. (002) RSM. In the (002) RSM, Fig. 4.18 b), the InGaN peak is on the line which connects GaN peak to the reciprocal space zero point, indicating that there is no tilt of the InGaN layer to the GaN layer, so that the (-1-13) RSM can be safely used to evaluate the strain status and In mole fraction. Two lines drawn in the Fig.4.18 a) indicate the direction of GaN reflex to the fully relaxed and pseudomorphical InN reflexes, respectively.

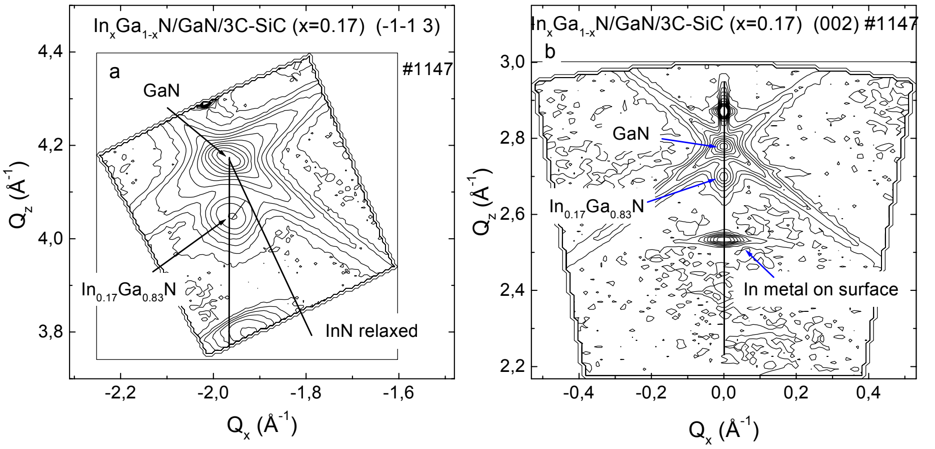

Figure 4.18 XRD reciprocal space map around GaN and InGaN reflexes, a) (-1-13) b) (002)

The InGaN reflex is close to but not exactly on the line which indicates fully strained

InGaN layers, which means the InGaN layer is partially relaxed on the GaN buffer layer. The line, which crosses the InGaN reflex maximum and is parallel to the line between the relaxed and fully strained InN is also plotted in this graph. This line shows the reflex of InGaN layer with a certain In mole fraction, but different strain status from the fully strained to fully relaxed. The In mole fraction of this sample is carried out of 17% from the distance ratio of this line to GaN and InN to GaN.

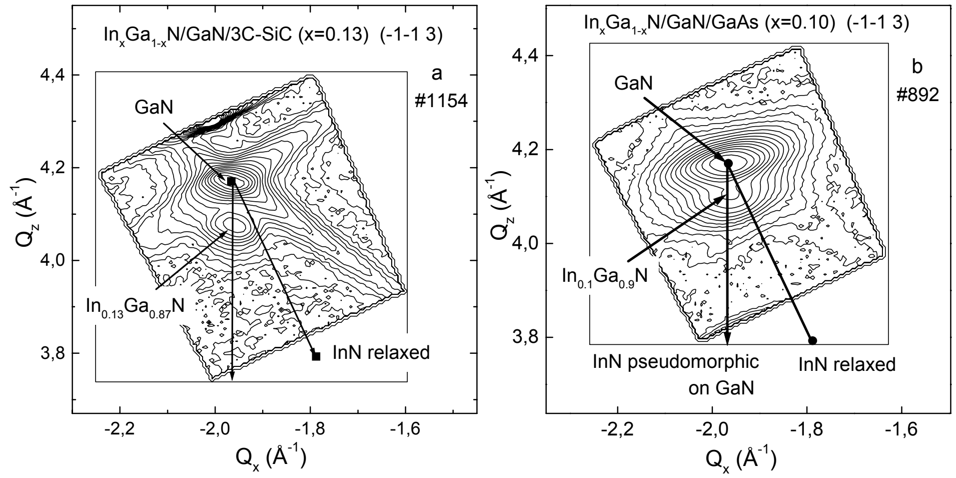

Figure 4.19 XRD (-1-13) RSM of InGaN grown on 3C-SiC substrates and GaAs substrates.

The calculation also gives the relaxation of 15% for this sample. Figure 4.19 a) plots the (-1-13) RSM from InGaN sample #1154 grown on 3C-SiC substrate. The sample information is given in table 4-2. The InGaN reflex is well separated from the GaN reflex and the fully strained line transverse the InGaN reflex in this graph, showing that the $\mathrm{In_xGa_{1-x}N}$ layer is pseudomorphically grown on the GaN buffer layer. The In mole fraction is 0.13. The (-1-13) map from InGaN sample #892 by using a GaAs substrate is plotted in Fig 4.19 b). For the InGaN sample using a GaAs substrate, although with the lower In mole fraction x = 0.10 than the $\mathrm{In_{0.13}Ga_{0.87}N}$ using 3C-SiC substrate, the InGaN is partially relaxed with relaxation of 25% to GaN buffer layer.

4.6.2 Critical thickness

In the heterostructure with lattice mismatch, the strain relaxation will happen via generation of misfit dislocation when the epilayer thickness exceeds the critical thickness. Dislocations degrade the material quality, e.g. dislocations generated by the strain relaxation in some cases are supposed to be one of the origins for non-radiative recombination of excess carriers. Thus, the generation of dislocations has to be avoided in highly efficient optoelectronic devices. In the following, I discuss the critical thickness for our cubic InGaN/GaN system.

Basically, two different kinds of models are frequently adopted in the literature, one was developed by Van der Merwe[148] on the basis of energy considerations, in short: the interface energy between the film and substrate was assumed to be the minimum energy available for generation of dislocation. In practice, this model gives a smaller estimation on the critical thickness than the measurement results [100]. Matthews and Blakeslee[99] suggested another model to calculate the critical thickness. This method balances the line tension present on a dislocation against the glide force present in a strained film. According to this model, the critical thickness h_c is expressed as

$$h_c = \frac{b}{4\pi f(1+\upsilon)}\left[In(\frac{h_c}{b})+1\right] \qquad (4.4)$$

in which, b is Burgers vectors,υ is the Poisson ratio, f is the lattice mismatch.
People and Bean[100] developed another model assuming that misfit dislocation generation is determined solely by the energy balance. It is assumed that the growing film is initially free of threading dislocation, and that interfacial misfit dislocation will be generated when the areal strain energy density exceeds the self-energy of an isolated dislocation of a given type (e.g. edge, screw, etc..). It is described as the function of the In mole fraction of x:

$$h_c(x) \cong \left(\frac{1-\upsilon(x)}{1+\upsilon(x)}\right)\left(\frac{1}{16\pi\sqrt{2}}\right)\left[\frac{b^2}{a(x)}\right]\left[\left(\frac{1}{f^2(x)}\right)In\left(\frac{h_c(x)}{b}\right)\right] \qquad (4.5)$$

in which υ (x) is the x dependent Poisson ratio. The f(x) and a(x) are the lattice mismatch of InGaN to GaN and lattice constant of InGaN.

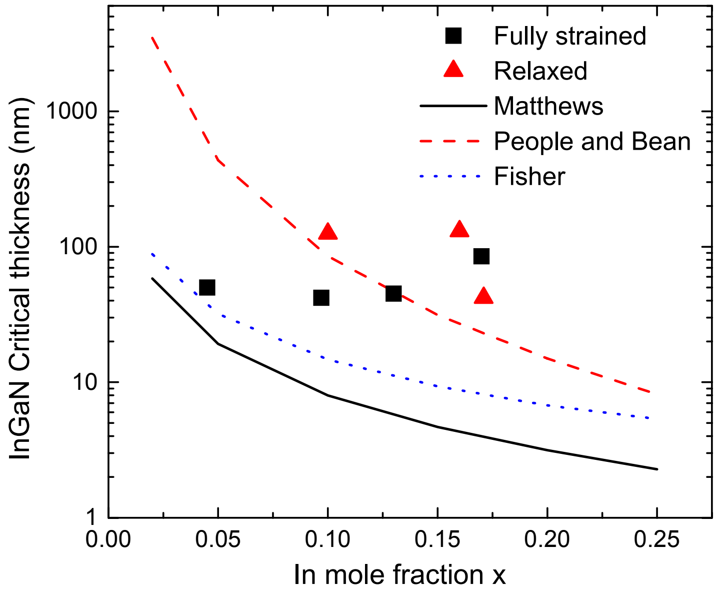

Figure 4.20 Calculated critical thickness of c-$In_xGa_{1-x}N$ on GaN versus the In mole fraction x. InGaN samples with strain status are also shown in this figure.

Fisher et al[149] presented another new approach which includes the elastic interaction between straight misfit dislocations based on the mechanical equilibrium. This model is given by:

$$\left(\frac{a_0-a_s}{a_s}\right)=\left(\frac{b\cos\theta}{2h_c}\right)\left[1+\left(\frac{1-\upsilon/4}{4\pi(1+\upsilon)\cos^2\theta}\right)\ln\left(\frac{h_c}{b}\right)\right] \qquad (4.6)$$

where a_0 and a_s are the lattice constant of the epilayer and substrate. The θ is the angle between the Burgers vector and the direction in the interface, normal to the dislocation line, in this case, θ = 60°.

The data calculated from these three models are depicted in Fig. 4.20. Also indicated in Fig. 4.20 are data from our epitaxial InGaN layer, in which the strain status is shown. The thickness of the strained InGaN layers is larger than the predicted critical thickness by Fisher's and Matthews' models. The thickness of relaxed InGaN layers shows that the calculated values by People and Bean's model fits our data better. This coincides with the results from hexagonal InGaN [150].

4.6.3 High resolution X-ray diffraction linescan of c-InGaN

The HRXRD linescan is a routinely performed measurement method on InGaN layers. The ω-2θ scan is the scan along the direction from the studied reflex to the origin of reciprocal space, which gives the lattice constant of the InGaN in one direction from the InGaN peak position. The full width of half maximum (FWHM) of a ω-2θ scan is determined by the mosaic crystal size and lattice constant fluctuation induced by the inhomogeneous strain and the indium atoms distribution. The FWHM from the ω-scan (rocking curve) includes the information of the dislocation density besides the mosaic crystal size and the inhomogeneous strain. Figure 4.21 shows ω-2θ linescans of InGaN layers with different In mole fraction grown on c-GaN/GaAs substrates. The peaks with maximal intensity are the GaN buffer reflexes, whereas the arrows in the graph indicate the InGaN peaks. The sharp peak around 18.1° is confirmed to be the Bragg reflex from indium metal droplets on the surface. The In mole fraction x of every sample is marked in the graph. The measurement curves are fitted by *pseudo-Voigt* functions, the InGaN and GaN peak positions are derived from the fitting. The distance between the GaN and InGaN peaks is proportional to the In mole fraction in the case that all InGaN layers have an identical strain status. For determination of the In mole fraction, the fully-relaxed lattice parameter should be clarified assuming the tetragonal distortion [51].

The In mole fraction can be derived from the InGaN lattice parameters of relaxed InGaN assuming Vegard's law.

$$x = \frac{a_{InGaN} - a_{GaN}}{a_{InN} - a_{GaN}} \tag{4.7}$$

where a_{InGaN} is the lattice constant of an InGaN crystal cell unit free of strain.

The same ω-2θscans around the GaN and the InGaN (002) reflexes on $In_xGa_{1-x}N$ samples with different x on 3c-SiC substrates have been show in Fig. 4.22. The InGaN peaks indicated in this figure have an increasing distance to GaN peaks due to the increasing out-of-plane lattice constant.

All the InGaN layers are shown pseudomorphically on GaN buffer layers. It is worthwhile to point out the fact that no peaks from separated In rich InGaN phases were detected from the InGaN/GaN line scan. There is no tilt of InGaN layer to GaN buffer layer found in the investigated samples.

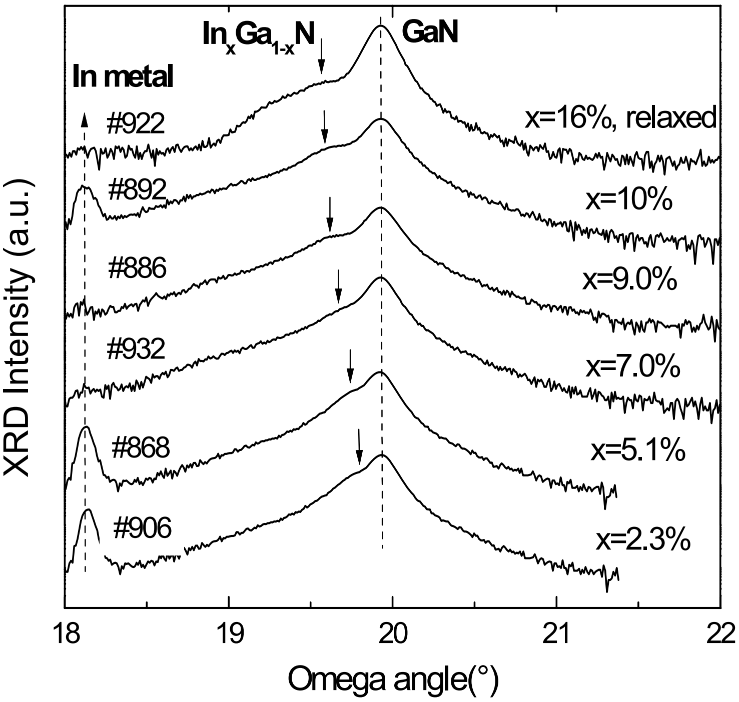

Figure 4.21 HRXRD ω-2θ scans on InGaN/GaN samples with different In mole fraction using GaAs substrates.

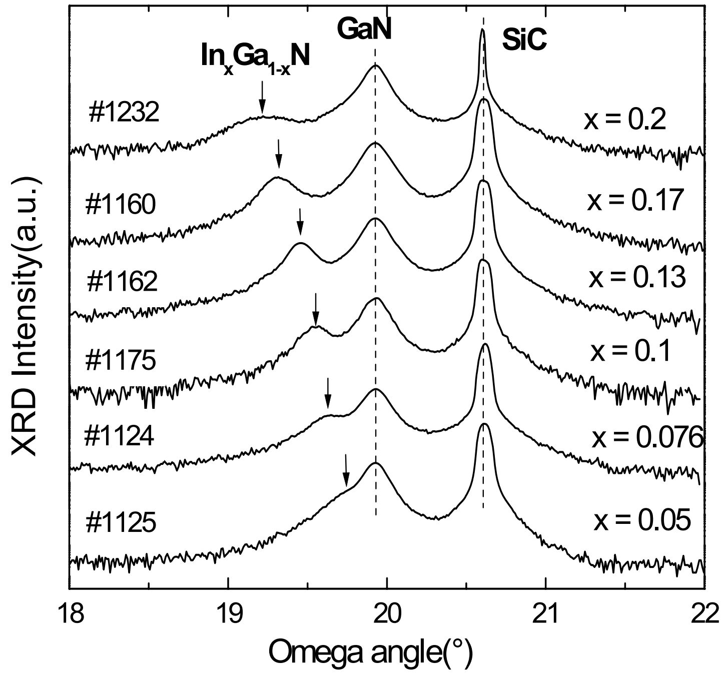

Figure 4.22 HRXRD ω-2θ scans on InGaN/GaN samples with different In mole fraction using 3C-SiC substrates.

This means that if the separated InGaN phase exits, it must have very small volume so that it cannot be traced by HRXRD. Comparing ω-2θlinescan from InGaN on 3C-SiC substrates to InGaN on GaAs, we clearly found that by using 3C-SiC substrates the InGaN layers have better crystal quality than InGaN grown on GaAs substrates, which is shown by the sharper peak and clearer separation of InGaN and GaN peaks of InGaN samples on 3C-SiC substrates with similar In mole fraction.

The line widths of the InGaN peaks were broader than those of GaN in all the curves. The InGaN line width includes the inhomogeneous strain broadening induced by the indium incorporation and the crystal size effect in the normal direction, i.e. the thickness in this case. The broadening from the InGaN layer thickness D, is expressed as[151]:

$$D = \frac{\lambda}{2 * FWHM * \cos\theta} \tag{4.8}$$

where λ = 0.154056nm, θ is the Bragg angle. FWHM in this case is the line width of the InGaN peak from the ω-2θ linescan. Figure 4.23 plots the ratio of the difference of InGaN and GaN linewidth to GaN linewidth versus the In mole fraction. The FWHM of InGaN calculated here has subtracted the linewidth broadening from the layer thickness.

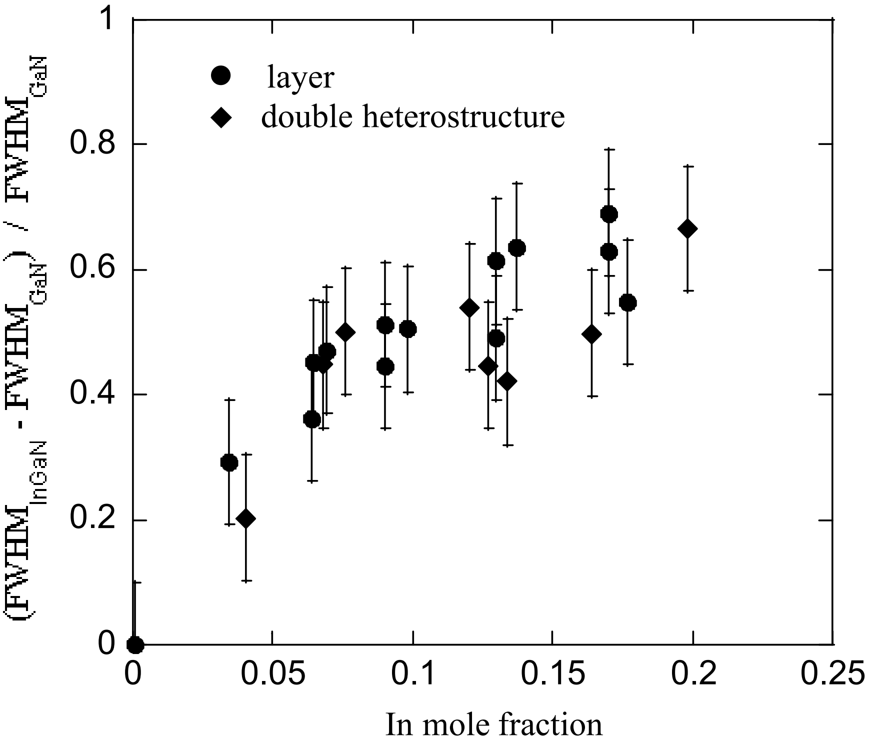

Figure 4.23 Relation between the ratio of the FWHM difference of InGaN and GaN to the FWHM of GaN and the indium mole fraction. The InGaN FWHM has excluded the influence from the InGaN layer thickness

The ratio of the FWHM difference between InGaN and GaN to GaN FWHM increases with the indium mole fraction. It reaches about 60% at x = 0.2, which shows that the extra broadening from InGaN peaks mostly stems from the random In atoms distribution, i.e. alloy disorder. If the linewidth broadening in InGaN diffraction peaks corresponds to the In composition fluctuation in the InGaN layers, it delivers the broadening of the InGaN bandgap.

4.6.4 Transmission electron microscopy results

The research group of Linz University performed TEM measurements on our InGaNDH sample#1112. This sample consists of a 45nm GaN capping layer and 35nm $In_xGa_{1-x}N$ layer with x = 0.07 and 500nm GaN buffer layer.

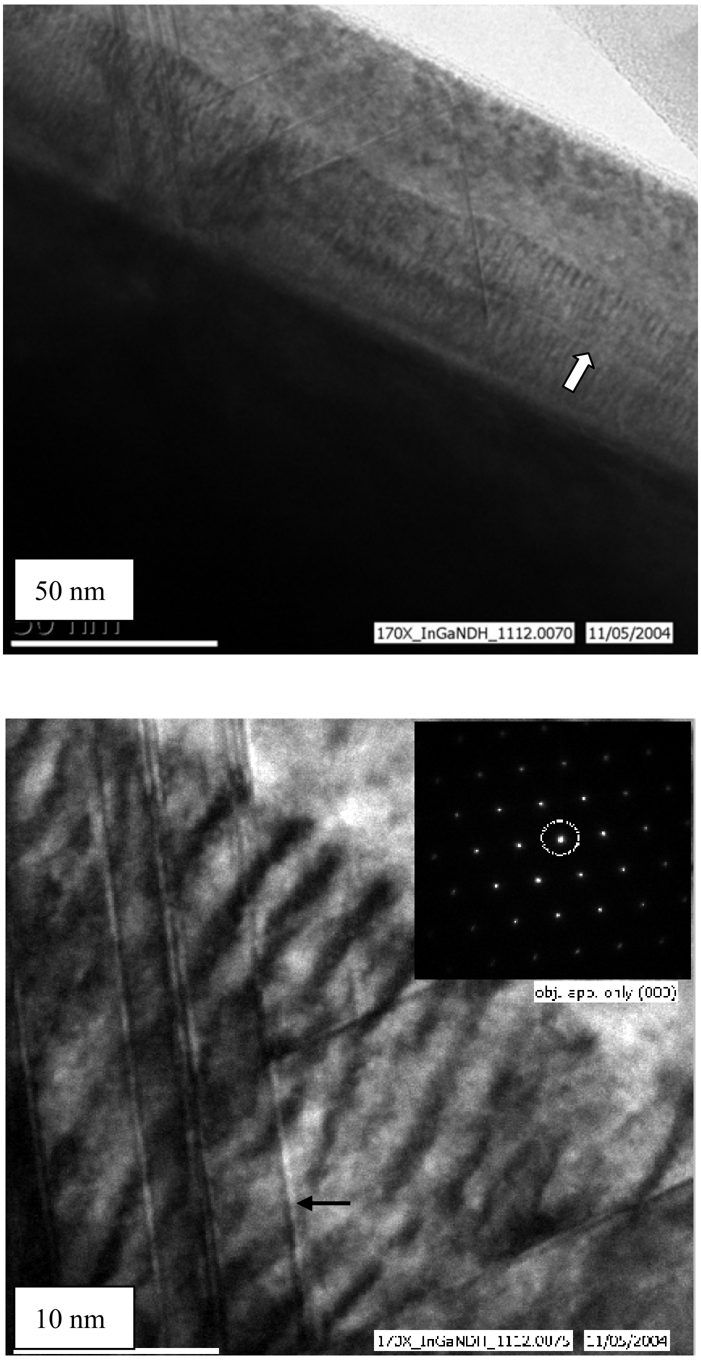
50 nm
170X_InGaNDH_1112.0070
11/05/2004
obj. apo. only (000)
10 nm
170X_InGaNDH_1112.0075
11/05/2004

Figure 4.24 Transmission electron microscopy on InGaNDH1112 with low (a) and large (b) magnification. The legends are shown in the pictures.

TEM pictures are showm in figure 4.24. The thickness is estimated from the growth rate of GaN and the reflectance measurements of the sample. From the legend of the picture, A InGaN thickness of about 40nm is measured. The GaN capping layer thickness is 40-50nm. The InGaN/GaN interface is clearly distinguished in Fig.4.23a, but with a wavy fluctuation, which reveals the inferior interface quality. There is a line in the middle of the InGaN layer parallel to the interface (indicated by the arrow in Fig.4.23a), which is due to the InGaN growth interruption. Figure 4.23b is the enlarged picture on the InGaN layer. The stacking faults stem from the GaN buffer layer and cross the InGaN and GaN capping layer (indicated by arrows), which can also be found in Fig.4.23a. A significant feature is that in the InGaN layer the parallel column structures are found. The column starts from the interface of the InGaN/GaN buffer to the InGaN/GaN capping layer interface along the growth direction, with the same dimension as the InGaN thickness, which reveals that it relates to the InGaN alloy. The lateral dimension of the column structure is about 2-3nm. It is still not clear if it is in the shape of pillar or slab. I suppose that these columns structures are probably the In rich or In poor phases, which give different contrast in the TEM picture. The In rich phase is the origin for localized structures in InGaN layer. Up to now, there is no proven explanation why this kind of structure formed in InGaN.

4.6.5 Raman scattering measurements

The crystallinity and state of tension of the film can also be inferred from the Raman spectrum. It has already been established that the c-InGaN alloy exhibits one-mode behavior [152,153, 152], i.e. the Raman spectrum consists of a single TO and a single LO line which vary in frequency linearly between those of the two binary compounds (InN and GaN). Raman measurements for characterization on the structural information of our InGaN samples are shown here. The Raman measurements were performed at San Paulo University. Unpolarized micro-Raman measurements were made at room temperature in the backscattering configuration using Argon-ion laser excitation (488-nm line). Raman spectra from our samples are displayed in Fig. 4.25(a) and 4.25(b).

The spectra show structures originating in both TO (around 550 cm^{-1}) and LO phonons (around 740 cm^{-1}) of the GaN buffer layer and of the alloy. The corresponding lines of the alloy appear as weak shoulders at slightly lower frequencies than the former. This disparity between the intensities of Raman features originating in the alloy and buffer layers is due to the fact that the thickness ratio between these two layers in our samples is ~ 0.1 (see table 4-4). Thus, in order to extract information about the frequencies of the alloy phonons, a line fitting has to be made of these spectra. Representative examples of these fittings, for samples deposited on both types of substrate, are displayed in Figs. 426(a) and 4.26(b). These fittings provide values for both frequencies and relative intensities of all lines, which can be used for extracting information about the state of strain of the InGaN layers. The spectra of Figs. 4.25 and 4.26 were taken in the backscattering configuration, with incoming and scattered radiation propagating perpendicularly to the film surface i.e., along the laboratory z-axis.

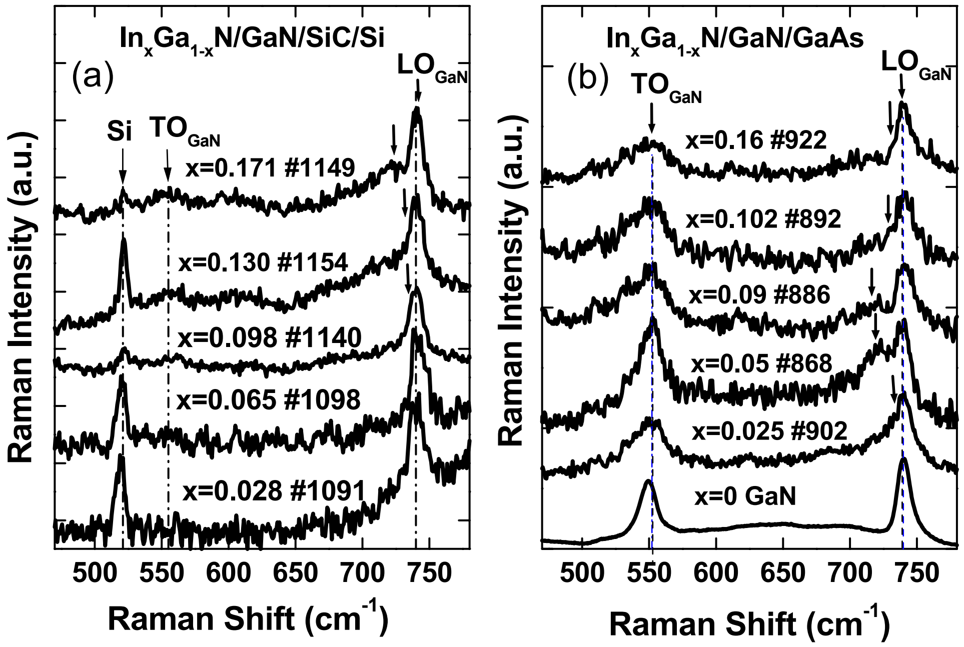

Figure 4.25 Raman spectra using 488nm Ar laser excitation, a) $In_xGa_{1-x}N/GaN/SiC$ and (b) $In_xGa_{1-x}N/GaN/GaAs$.

For films of perfect crystalline order, this direction should coincide with the cubic z-axis, the (001) direction. In such a configuration, scattering by LO phonons is allowed for (x,y) polarization, but scattering by TO phonons is strictly forbidden, because it could only occur for (x,z) or (y,z) polarizations; both impossible, because it would require that light be polarized along its propagation direction. However, figure 4.25(b) shows that the line attributed to TO scattering is sometimes as intense as that attributed to LO scattering. This is due to poor crystalline quality. It tells us that, although neither incoming nor scattered radiation can be polarized along the laboratory z-axis, misalignment of crystallites in the film (both in the alloy and the GaN layers) produce grains with the z-axis of the crystallites tilted towards the laboratory z-axis. Hence, there can be a projection of the incoming and outgoing beam polarizations along the crystal (001) direction. If the films were perfect, this would be impossible. Hence, the ratio of the intensity between TO and LO lines (I_{TO}/I_{LO}), which should be zero for a perfect crystal, can be used as an indicator of crystalline quality. A visual inspection of Figs. 4.25(a) and 4.25(b) shows that the (I_{TO}/I_{LO}) ratio is much larger in samples grown on GaAs substrates than in those grown on SiC substrates. In fact, comparing two samples grown on the two types of substrates of approximately the same In mole fraction (x?0.09), samples #886 and #1140, respectively, we find (I_{TO}/I_{LO}) = 0.89 for the sample grown on GaAs and (I_{TO}/I_{LO}) = 0.19 for that grown on SiC. These numbers refer to the intensity ratio of the GaN peaks, since those of the alloy TO phonons from the InGaN films grown on SiC are so weak that they do not show up in our spectra. Thus, the crystalline quality of the GaN buffers grown on SiC substrates appears to be much better than that grown on GaAs substrates.

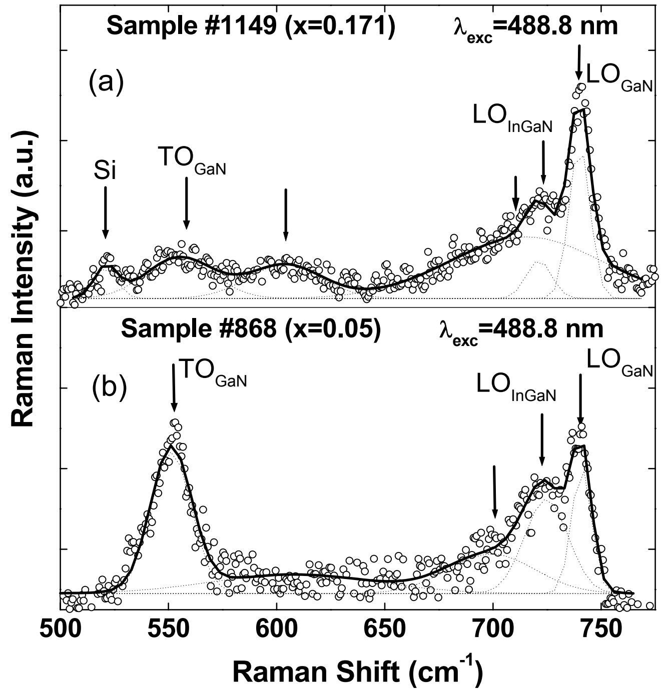

Figure 4.26 Typical Raman spectra from $In_{0.17}Ga_{0.83}N$ #1149using 3C-SiC substrate and $In_{0.05}Ga_{0.95}N$ #868 grown on GaAs substrate.

The alloy layers should follow this trend, which is shown by the fact that the TO line from the alloy layer is only visible in the spectra of films grown on GaAs.

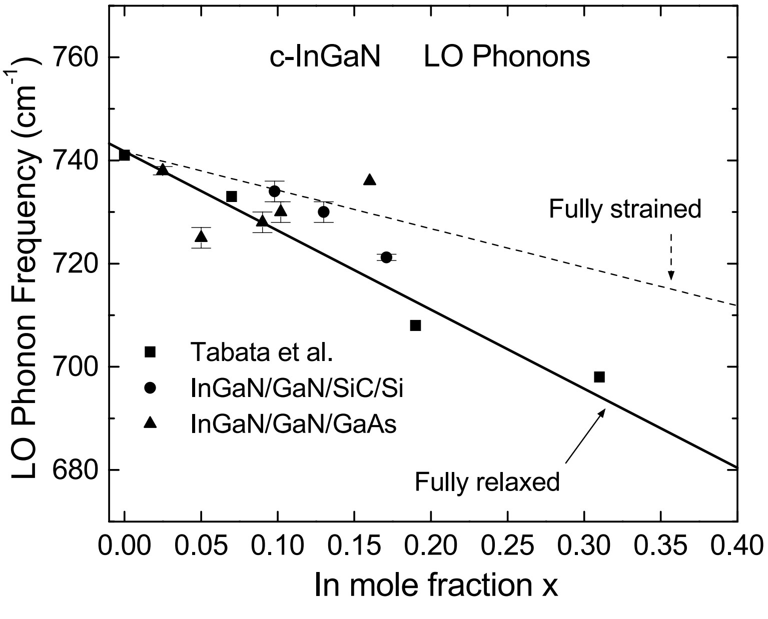

Figure 4.27 InGaN LO phonon frequency versus In mole fraction, the dashed line denotes the fully strained InGaN LO line and the solid line for fully relaxed InGaN LO line.

Phonon frequencies are affected by the In content of the alloy and by the state of strain of the film. In totally relaxed films the former gives a linear decrease of the phonon frequency as the In molar fraction (x) of the c-$In_xGa_{1-x}N$ increases. The attention will be focused on the LO phonon, which is the one more clearly observed in the spectra of all the samples (see Fig. 4.25). In Fig. 4.27, we represent this linear tendency for the data of Tabata *et al*[154], which corresponds to thick, totally relaxed (unstrained) c-$In_xGa_{1-x}N$ films deposited on a GaN substrate (full squares). The straight line corresponds to a linear least-squares fit to their data and represents the dependence of the LO frequency on the In mole fraction for unstrained films. This line is given by:

$$\omega_{LO}^{0}(x) = \omega_{GaN}^{0} - \Gamma x \qquad (4.9)$$

where $\omega_{LO}^{0}(x) = 741{,}73cm^{-1}$, Γ = 153,29 cm^{-1} and the superscript "0" signifies the absence of strain.

The LO frequency for a fully strained layer versus the In mole fraction is expressed by David [155] as:

$$\omega(x) \cong 741{,}73 - (153{,}29 - 70{,}179|b|)x \qquad (4.10)$$

where frequencies are given in cm^{-1} and x is the In mole fraction. Both *x* and *b* are dimensionless numbers. Here the values of 0.4520 nm (0.4970 nm) were used for the equilibrium lattice parameter of GaN (InN). The parameter *b* does not seem to vary from one material to the other in II-VI or IV materials [156, 157]. Hence, we can tentatively use the value for this parameter measured with great precision for the LO phonons of GaAs (*b =-1,119*) by Hünermann et al. [158]. Inserting this value in eq.(4.10), we obtain the dashed line of Fig. 4.27. Hence, we have two relevant straight lines in this figure: the full line, representing the dependence of the LO phonon frequency of the unstrained layer on the In molar fraction (eq. 4.9) and the dotted line which is our best estimate for this dependence of the fully strained InGaN layer. If films are fully relaxed, their LO phonon frequencies should be around the lower (full) line, while those of the fully strained film should be around the upper (dashed) line. Our data is represented in this figure by full triangles for samples grown on GaAs substrates and full circles for those grown on SiC substrates. These data show that the former are around the totally relaxed line (with the exception of sample #922 (x=0.16), which is anomalous in many ways), while the latter are around the fully strained line. This is in agreement with the XRD measurement results. The fact that the samples grown on SiC are close to the fully strained situation while those grown on GaAs are not is maybe a reflection of the better crystallinity of the GaN buffer on SiC substrates, as shown by the (I_{TO}/I_{LO}) ratios on their Raman spectra. On the other hand, strain relaxation in the samples grown on GaAs substrates is almost certainly aided by the fact that the alloy layers grown on these substrates are thicker than those grown on SiC substrates.

4.7 Optical properties of c-InGaN

As the active layers in III nitride based optoelectronic devices, the optical properties of InGaN are critical for realizing high efficiency light emitting devices. Here I report the optical measurement results from our InGaN layer by photoluminescence excitation spectra (PLE) measurements on the cubic InGaN samples grown on 3C-SiC substrates and temperature dependent photoluminescence spectra. The band gap of InGaN layers determined by PLE and ellipsometry measurements versus In mole fraction is also demonstrated.

The fact that hexagonal and cubic InGaN emission is observed at energies far below the energy gap of the alloy which is measured by absorption or ellipsometry and that the high efficiency carrier recombination is insensitive to defects led to the assumption that the photoluminenscence (PL) results from excitons localized in In-rich regions [159,160]. However, in hexagonal group III nitrides piezo-electric and spontaneaous polarization fields give rise to a quantum confined Stark effect (QCSE) if the samples are grown in (0001) direction (c-axis) [161]. This QCSE introduces an additional strong PL red-shift in the h-InGaN/GaN quantum wells [162]. It has been proven that the polarization field is absent in cubic InGaN/GaN system, which helps to investigate the intrinsic optical properties of InGaN layer.

Alternatively, In segregation may result in the formation of very small $In_xGa_{1-x}N$ localized structures, such as quantum dots where the In composition is much larger than the overall average composition [163]. This segregated compositional localized structure would have a smaller energy gap than the bulk alloy and would provide efficient recombination centers, because electron-hole pairs created by incoming radiation close to the localized structures would migrate into them and recombine from them. Hence, strong absorption would occur at the energy gap of the bulk alloy (because this occupies the overwhelmingly larger fraction of the volume of the sample), whereas recombination would occur preferentially in the In-rich regions having a smaller energy gap.

If the ratio between the total volume occupied by localized structures and that of the bulk alloy is sufficiently small, the absorption by the In rich regions should be undetectable in ordinary optical experiments, such as absorption or ellipsometry and even in X-ray diffraction spectra. If one wants to reveal the direct absorption of the localized structures one has to use different techniques such as photoluminescence (PL) or photoluminescence excitation spectroscopy (PLE) [164].

4.7.1 Photoluminescence excitation measurements on c-InGaN

$In_xGa_{1-x}N$ samples investigated in this part were grown on 3C-SiC substrates using our MBE system. Prior to InGaN growth, a 500nm GaN layer was grown directly on 3C-SiC substrates, followed by 50nm $In_xGa_{1-x}N$, with x changing from 0-0.17. The In-content and the strain status were measured by high resolution x-ray diffraction. The characteristics of the samples used in our experiments can be found in Table 4-2 and 4-4.

The PL and PLE measurements were performed in Prof. Leite's group at Sao Paulo University. PL spectra were measured both with He-Cd laser (λ= 325 nm) and arc-lamp excitation. The samples were placed in a cold finger cryostat, where the temperature could be varied continuously from approximately 3K to 300K. The measurements with arc lamp excitation, both PL and PLE, were performed with an air-cooled 1000 W Xe lamp filtered with a 1.0m SPEX monochromator with a 1200 groove/mm grating. The monochromatic light was focused onto the sample, contained in an Air Products cold finger cryostat at T = 7K. The emitted light was focused into a double monochromator with a Ga-In-As photo-multiplier tube. Quartz lenses were used both for excitation and collection of emitted radiation.

Figure 4.28a shows the PL spectra of the InGaN samples. These spectra were taken at 2.5 K using the λ= 325 nm line of a He-Cd laser as the source of excitation. Arrows indicate the maximum of the PL emission for samples with indium molar fraction x ? 0.098. For these samples a strong emission peak around 2.5 eV occurs, which has been attributed to recombination at In-rich sites of the sample [165]. The same information is displayed in Fig. 4.28b in a logarithmic intensity scale. In this figure a secondary maximum at lower photon energies can be observed in some samples, also indicated by arrows in the figure. This signifies that the emission peak is composed of a superposition of peaks centered at different photon energies. In addition, the low temperature PL spectra of these samples was taken using the filtered radiation from Xe arc as excitation. The spectra obtained in this way are entirely similar to those of Fig 4.28, albeit with a smaller signal-to-noise ratio. All these spectra show a very broad emission at photon energies between 2.5 and 2.7 eV (which may appear as the superposition of more than one peak for some samples) and a number of sharper structures at higher photon energies. Of the latter, some are clearly associated with the emission of the GaN buffer layer (see for instance refs. [165, 166]), while others (in particular sharp lines around 2.9 eV) could be, in principle, also attributed to the InGaN alloy layer.

In order to try to assign correctly the observed PL lines, we proceeded to take low temperature PL spectra with lamp using progressively higher wavelengths (lower photon energies) as exciting radiation. As the photon energy of the exciting radiation decreases below the absorption edge of the GaN buffer, some lines drop away from the PL spectrum, as illustrated in Fig. 29a for sample #1154 (x = 0.13). This figure shows that when the excitation photon energy falls below the GaN energy gap $(h\nu_{exc} \leq 3.2eV)$, the PL features at 2.75 and 2.85 eV disappear from the spectrum. This identifies these lines as originating in the GaN buffer layer rather than in the InGaN alloy layer. Also some new sharp features appear below 2.3 eV, which lies just below the indirect gap of the SiC [167]. Since at this low excitation frequencies the light penetrates all the way into the SiC substrate, we attribute these new lines to emissions from SiC (bound impurities associated with the indirect gap and their phonon replicas)[168]. Thus, the only feature in the PL spectra of our samples which can be unequivocally attributed to the InGaN layer is the rather broad emission appearing around 2.5 eV for most of our samples. This line survives even for excitations very close to this maximum. This is illustrated in Fig 4.29b, which shows this PL peak taken with the λ=488nm $(\hbar\omega = 2.54eV)$ line of an Argon-ion laser and the PLE absorption profile of the InGaN layer obtained by PLE (see PLE discussion that follows).

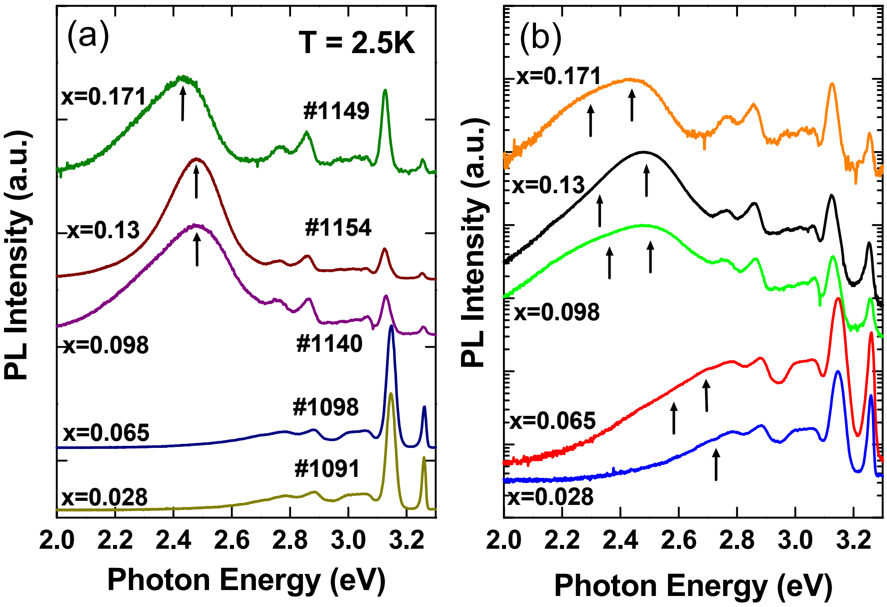

Figure 4.28 Low temperature PL spectra on c-InGaN samples

Notice that, although the excitation is very close to the emission peak and well below the absorption edge of the alloy layer (indicated by a vertical arrow in Fig.29b), the recombination peak is still clearly observed.

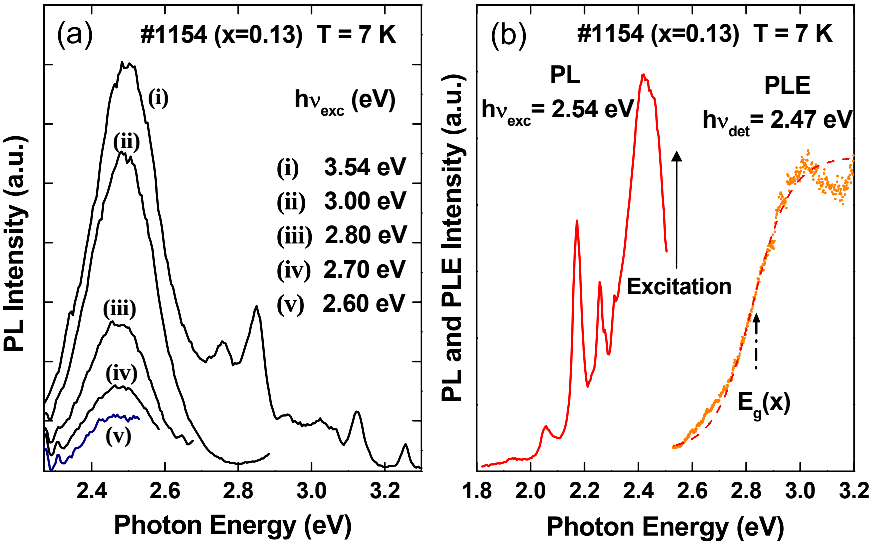

Figure 4.29 a) 7K PL measurement on $In_{0.13}Ga_{0.87}N$#1154 by various light wavelength excitation from the lamp. B) 7K PL at excitation light of 2.54eV and PLE measurement at detection energy of 2.47eV.

This indicates that this recombination occurs because of absorption occurring within the alloy layer, but not by the part of the layer having average composition (henceforward referred to as bulk layer), which has an absorption edge above that of the exciting radiation. Rather, the light appears to be absorbed by the same part of the layer responsible for the emission i.e., the In-rich phase with a lower gap.

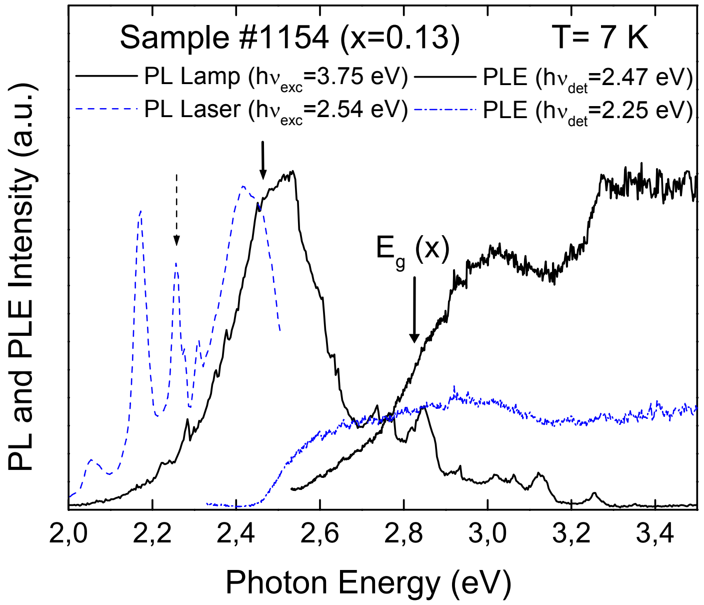

Figure 4.30 Low temperature (7K) PL spectra with excitation energy of 3.75 eV, 2.54eV and PLE spectra detected at 2.47eV, 2.25eV.

Finally, although the whole discussion was based on results from sample #1154, the same could be argued from the spectra of all the other samples (not shown), which all display the same type of behavior. The type of absorption depicted in a PLE spectrum depends on the photon energy at which the analyzing spectrometer is centered. This is illustrated in Fig.4.30, where the PL and PLE spectra of sample #1154 (x=0.13) are displayed. In this figure, the different PLE spectra are centered at different photon energies. This is indicated by solid or dashed curves. Arrows indicate the centering of the photon energy PL detection for each PLE curve of the same type (dashed or solid). If centering is made around the energy of the PL maximum ($\hbar\omega \cong 2.47eV$, solid arrow), previously identified emission as originating from the alloy layer, two clear absorption edges are observed (solid curve): one corresponding to the GaN buffer layer (E_g= 3.26 eV) and another at lower photon energy (E_g= 2.8 eV, solid arrow), which we attribute to the main absorption edge of the alloy layer. The dashed PLE curve in Fig. 4.30 was taken with centering well below the PL maximum ($\hbar\omega \cong 2.25eV$, dashed arrow) and has a different shape. This curve shows an absorption profile which starts to rise steeply at E ? 2.4eV (much lower than the absorption edge of the bulk alloy), then saturates, showing a more or less constant absorption, and finally drops again around the photon energy region where the GaN buffer layer starts to absorb light (see Fig. 30). This kind of absorption is only observed when centering is made at the low energy tail of the PL main peak and on top of PLE lines attributed to SiC emission (see dashed PL curve in Fig.4.30). Hence, it is reasonable to attribute this absorption-like feature of the PLE to the SiC substrate.

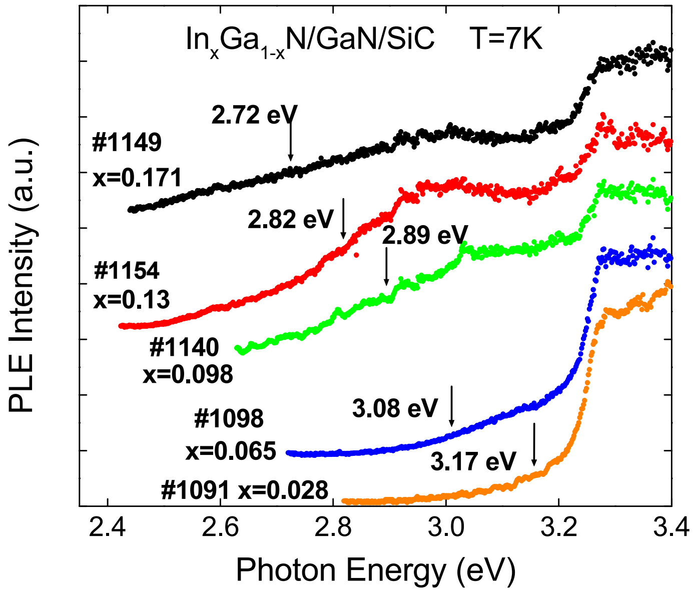

Figure 4.31 PLE measurements on $In_xGa_{1-x}N$ with different x at 7K.

As said before, when the detection frequency is centered on the main InGaN emission line, the absorption-like features in the spectra have two edges: one corresponding to the gap of the InGaN layer of average composition and another, around 3.25 eV, corresponding to the gap of the GaN buffer layer. These PLE spectra for all our samples are displayed in Fig.4.31. The arrows indicate the alloy absorption edges obtained by assuming that this edge can be fitted by a broadened step function, as is the case in c-GaN thin films [14]. This fitting is illustrated in Fig. 4.29 b) for sample #1154 (x =0.13).

The optical data discussed in the previous section has definite information as to the structure and composition of the InGaN layers. First, the PL spectrum reveals a broad structure (Fig.4.28), which is the only feature of the observed spectrum that can unequivocally be attributed to recombination processes taking place within the alloy layer of our samples (Fig. 4.29). This feature is not only broad, but in some cases shows secondary maxima (Fig. 4.28b). Also, this feature lies well below that of the absorption edge of the layer (Fig. 4.29b), and can be excited by radiation of photon energies lying well below this absorption edge. In fact, a look at Fig. 4.29b shows that even when this photon energy is located at points where the absorption of the InGaN layer is zero (dashed line in this figure), this feature still appears in the spectrum. This behavior clearly indicates that light is being absorbed within the InGaN layer, but it is not the bulk layer of average composition that is responsible for this absorption. Rather, the light appears to be absorbed by the same part of the layer responsible for the emission. This could, in principle, be identified as an indium rich phase (with a lower gap) occupying a negligible fraction of the layer's volume. The smallness of this fraction would be the reason why the existence of this phase goes undetected by ordinary absorption (or absorption-related techniques such as ellipsometry) and x-ray diffraction. Also, the fact that the PL peak is broad and appears to have more than one maximum can be attributed to the existence of quantum structures with different In concentration or sizes (consequently with different confining energies).

The positions of the energy gap in all the InGaN samples are consistently higher than that of the emission peaks in the PL spectra. Recent calculations [169] show that strain can suppress the formation of In rich phases by spinodal decomposition in the bulk of InGaN. Since all c-InGaN layers in the present work were strained, the experimental results indicate that the formation process of the In-rich phase seems to differ from bulk spinodal decomposition.

4.7.2 Band gap determination of c-InGaN

The band gap is an essential parameter for semiconductor material. For designing an InGaN based optoelectronic device in order to get the highly efficient light emission with targeted light wavelength from the InGaN active layers, one has to know the bandgap of InGaN varying with In concentration. The InGaN band gap varying with In concentration is also an important issue in the theoretical study. Unfortunately, it has been evidently proven that the optical emission of InGaN does not come from the homogeneous InGaN layer, but rather from the localized structures due to In segregation, phase separation and other reasons. These phenomena make the PL emission far below the bandgap of the "bulk" InGaN layer and it is not an available way to get the InGaN bandgap. The most commonly employed method in the literature for carrying out the InGaN bandgap is absorption spectrum [122,121], ellipsometry measurement[170] and photoluminescence excitation spectrum[171,172].

There are ongoing discussions on the band gap bowing parameter on the $In_xGa_{1-x}N$ changing with x [173,174,90]. Due to the difficulties in high In concentration growth of InGaN and pure InN, the band gap for $In_xGa_{1-x}N$ with high x or x=1 is rarely investigated [175,90,176]. This is responsible for the uncertainty in the determination of the band gap with high In concentration. As already mentioned, the InN bandgap is a disputed topic in recent years. Now, due to the improvement of h-InN growth, the influence from oxygen and the interface metal clusters could be avoided [119]. The InN band gap has been measured and discussed in several papers. The new h-InN band gap is 0.7-1.4eV. [121,122,120] The cubic InN bandgap has been calculated by Bechstedt et al[92], which is 0.58eV.

The band gap of cubic InGaN layers with different In concentration were measured by PLE and spectroscopic ellipsometry measurement. The samples investigated here are InGaN layers grown on GaN buffer layer using SiC substrates. Improved InGaN structural and optical quality due to employing the low mismatch substrate 3C-SiC, made it possible for more accurate band gap measurements. The PLE spectra shown in Fig.4.31, were measured in Prof. Leite's group at San Paulo Univ. The InGaN band gap versus In concentration was depicted in Fig. 4.32 (squares). The spectroscopic ellipsometry measurements for the InGaN bandgap were performed at Linz University. The InGaN bandgap results are also shown in Fig 4.32 (circles). The PLE and spectroscopic ellipsometry band gap measurement result show good agreement with each other.

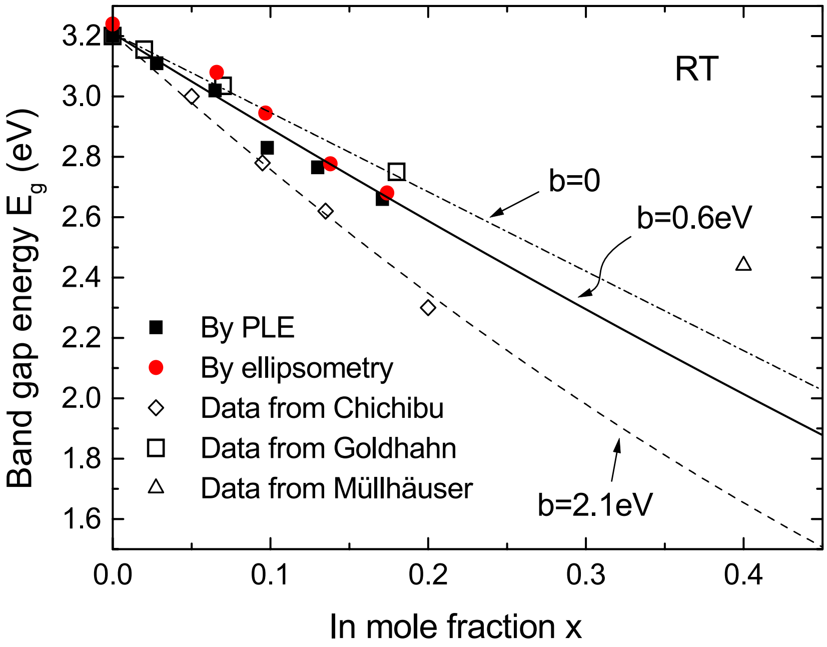

Figure 4.32 Cubic InGaN band gap versus In mole fraction x.

The band gap of cubic InGaN versus In concentration is fitted by polynomial functions with bowing parameter b, which is given as:

$$E_{In_xGa_{1-x}N} = E_{GaN} * (1-x) + E_{InN} * x - bx(1-x) \qquad (4.11\ )$$

The solid line is the InGaN band gap energy with bowing parameter of 0.6eV, showing the best fitting to the PLE and ellipsometry data, which is smaller than the new bowing parameter for new, small hexagonal InGaN, 1.4eV[90].

Result from Chichibu fits the line with a bowing parameter of 2.1[177]. Also shown in this figure is the line with the bowing parameter of 0 and 2.1eV. Data from Goldhahn[178] and Müllhäuser[179] are more close to the line without bowing.

4.7.3 Photoluminescence measurements on c-InGaN

The InGaN photoluminescence properties have been explored on the samples with different In mole fraction at room temperature and at temperature varying from 2K to 300K.

Figure 4.33 shows the room temperature PL spectra from InGaN layers with different In mole fraction grown on a 3C-SiC substrate. The InGaN thickness is about 60nm in all the samples. The $In_xGa_{1-x}N$ emission dominates the spectra and only a weak 3.2eV c-GaN emission is observed, indicating a high recombination efficiency of the

$In_xGa_{1-x}N$ layers. The PL-spectra from those structures which according to X-ray diffraction results contain $In_xGa_{1-x}N$ epilayers with “low” In-concentration (x=0.045) or “high” In-concentration ($x > 0.13$) consist of one single Gaussian-like peak at 2.6 eV and 2.4 eV, respectively.

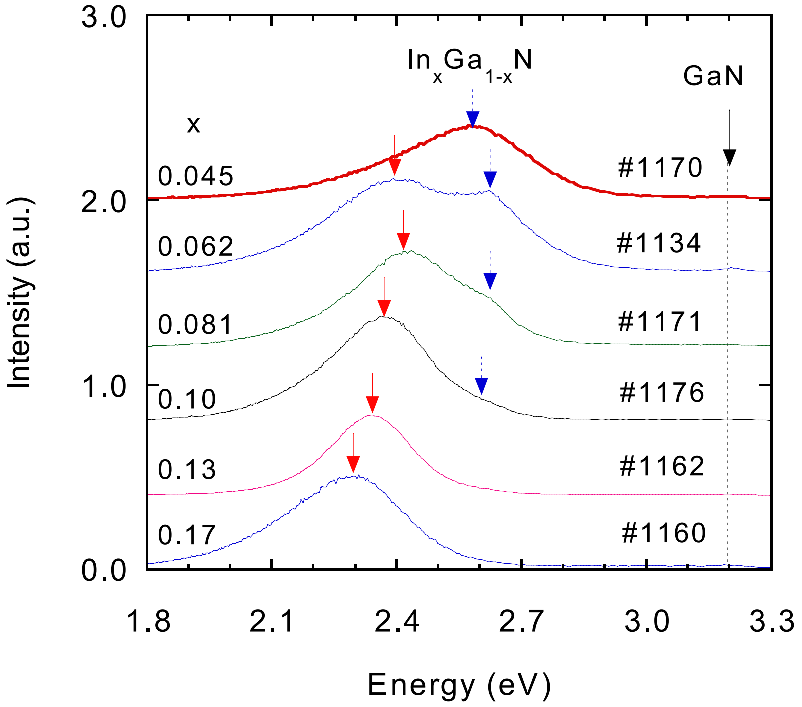

Figure 4.33 Room temperature PL spectra from $In_xGa_{1-x}N$ with different x. Arrows in the graph mark the PL peak positions

However, for intermediate In-concentrations ($0.062 < x < 0.13$), these two spectrally well-separated peaks exist simultaneously and the intensity ratio of the 2.4 eV peak to the 2.6 eV peak increases with increasing In composition. Both peaks are indicated in Fig. 4.33 by arrows and show a weak red-shift with increasing x-value.

Figure 4.34 shows the $In_xGa_{1-x}N$ related peak energy of our DH structures plotted versus In composition (full circles). Also included in this diagram are the PL peak energies of cubic $In_xGa_{1-x}N$ layers grown on 3C-SiC substrates and results from other groups (black triangles) [44,180]. These data reveal clearly that the PL emission of c-InGaN does not shift monotonically with increasing In content, but seems to be dominated by two well defined emission bands. The full squares are the $In_xGa_{1-x}N$ band gap energies measured by photoluminescence excitation (PLE) spectroscopy[181]. The black line shows the $In_xGa_{1-x}N$ band gap versus In composition. The PL peak energy is about 300 meV lower than the band gap and does not exactly follow the band gap energy dependence of $In_xGa_{1-x}N$. This large Stokes shift suggests again that localized structures in $In_xGa_{1-x}N$ may be responsible for the PL emission [180] and the existence of two peaks in the PL spectra indicate that at least two different $In_xGa_{1-x}N$ phases are formed which coexist simultaneously in the intermediate In-mole fraction range.

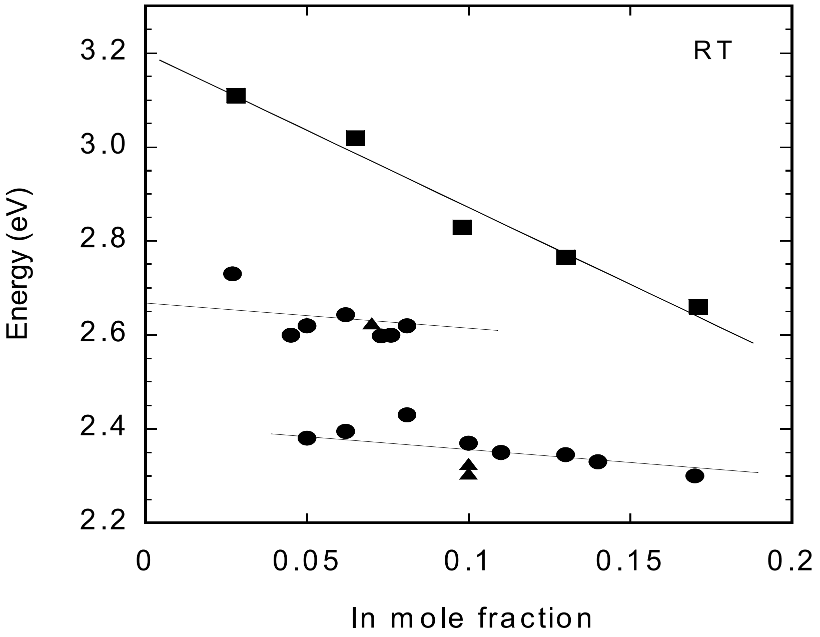

Figure 4.34 PL peak energy (full circles) and band gap energy (squares) versus In composition.

For further investigations on the PL properties of $In_xGa_{1-x}N$, temperature dependent PL spectra were measured on $In_{0.06}Ga_{0.94}N$ #1184 and $In_{0.13}Ga_{0.87}N$ DH #1162, which are the typical samples with two or only one emission peaks, respectively, in room temperature PL spectra.

Figure 4.35 shows the PL spectra from $In_xGa_{1-x}N(x=0.06)$ sample #1184, in which the temperature varied from 5K to 300K. The sharp peaks above 2.8eV have been ascribed to GaN related emission, which disappeared when the sample was excited by the laser with energy lower than the GaN bandgap. In the PL spectra at 5K, the InGaN emission can be fitted by two well-separated Gaussion-like peaks, which located in energy at 2.5eV and 2.7eV.

When including the temperature induced blue-shift of about 70meV, this two peak energies would be around 2.4eV and 2.6eV at 300K. In the low temperature range (5K-80K), the high energy peak with 2.7eV is dominant, whereas with increasing temperature, the intensity from this peak drastically decreases. Consequently, only a weak shoulder around 2.6 eV can be found at 300K spectrum originating from this 2.7 eV peak at 5K. The 2.5eV peak at 5K survived and became dominant at 300K with energy of 2.4eV. The bandgap of $In_xGa_{1-x}N$ with x=0.06 is 3.02eV, which is much higher than these two PL emission peak energies. The energy of these two peaks versus temperature is shown in Fig.4.36. The 2.4eV peaks shows a clear “S” shape behavior, a feature which was also found in hexagonal InGaN[182,183]. The 2.6eV peak energy keeps constant up to 120K, and then it follows the line of the temperature dependent band gap. Both peak energy variations with temperature indicate the strong localized properties of these emission peaks.

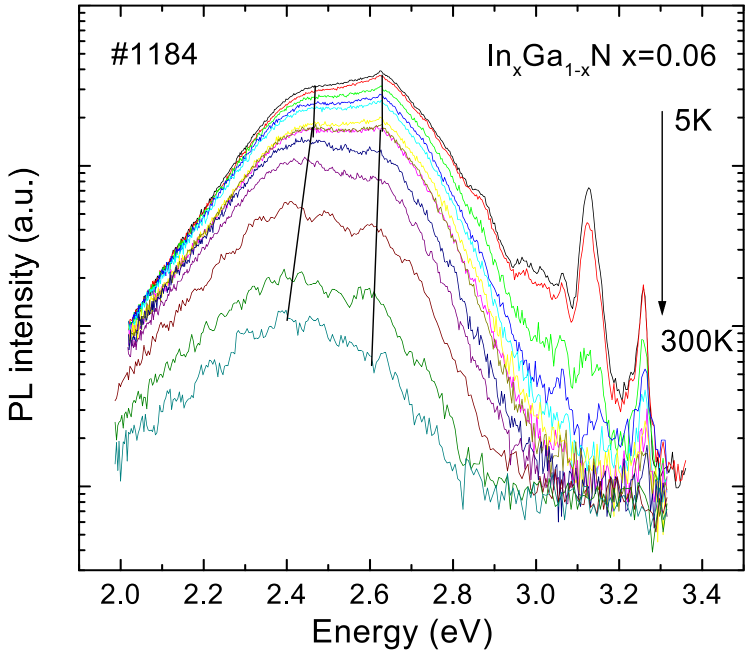

Figure 4.35 PL spectra from $In_{0.06}Ga_{0.94}N$ #1184 measured at temperature of 5K-300K. Two lines mark the energy variation with temperature.

These emission energy variations with temperature are fitted by the Varshni equation which includes two fitting parameters, shown as following [184]:

$$E(T) = E_0 - \frac{\alpha T^2}{\beta + T} \tag{4.12}$$

Where E_0 is the value of the energy gap at 0 K. α and β are constants. For the 2.4eV emission, the fit gives the energy gap E_0 of 2.463eV. The α and β got here are 7.5×10^{-4}eV/K and 600K. The same values of αandβwere put into the equation with E_0 of 2.657 eV and got a good fitting curve at high temperature, shown in Fig.4.36.

The deviation of both peak energies to the fitting curves at a low temperature range of 5-120K probably originates from the redistribution of the carriers between these two preferential InGaN localized structures due to the increasing of the temperature. For the 2.4eV emission peak, the carriers gain enough energy from the increasing temperature and jump out from the weak localized structures to the potential minimum, thus the peak energy decreases although the effective gap has a red-shift induced by the temperature. When the temperature increases further, the carriers have higher energy to occupy even higher energy states, which leads to a blueshift of the PL emission peak. The temperature-induced redshift of the band gap finally determined the PL emission peak variation at high temperature. This process gives a “S” shape behavior of the PL peak versus temperature. For the 2.6eV emission peak in the same manner, the compromise of the impact from the redistribution and temperature induced gap redshift consequently lead to constant PL emission peak from 5K to 130K. Then it follows temperature induced energy gap red-shift curve.

Integrated intensity versus the 1000/T is depicted in Fig.4.37. It follows the well-known thermal activation process:

$$I(T) = \frac{I_0}{1 + C * e^{-E_{act}/k_b * T}} \qquad (4.13)$$

where I(T) is the integrated intensity at temperature T, I_0 and C are constants, k_B is

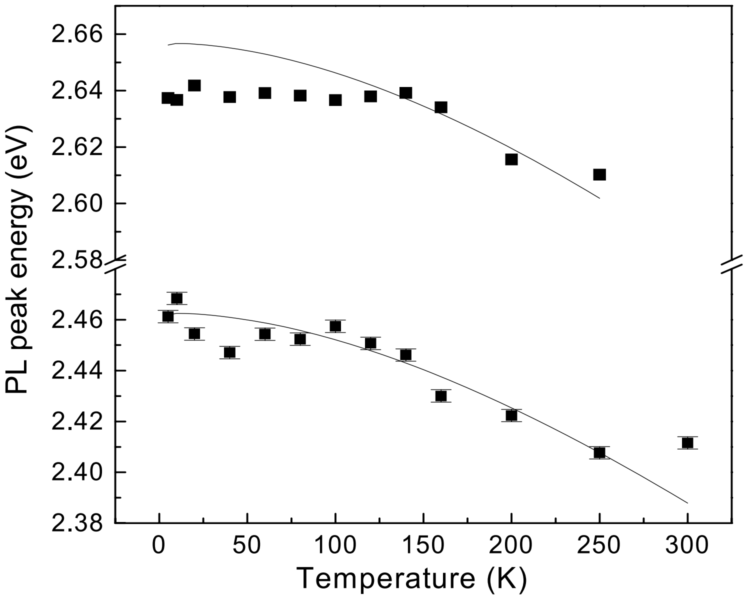

Figure 4.36 PL peak energy versus temperature from the $In_{0.06}Ga_{0.94}N$#1184.

Boltzmann's constant, E_{act} is the activation energy of this process. By the least-square fitting using this equation (the solid curve), the activation energy is obtained of 21meV for the 2.6eV peak and 67meV for the 2.4eV peak. The PL intensity ratio of the 2.6eV emission peak to the 2.4eV peak decreases with increasing temperature (as shown in the inset of Fig.4.37). The diffusion of the carriers from the localized structures with 2.6eV emission to those with 2.4 eV emission may happen to enhance the 2.4 eV emission intensity, and results in the dominant 2.4 eV emission at 300K. A similar phenomenon was also found in hexagonal InGaN/GaN. [185].

One "high" In mole content sample has also been investigated with the temperature dependent PL measurements from 4K to 300K. This sample #1162 has InGaN/GaN double heterostructures with an InGaN thickness of 50nm, and an In mole fraction of 13%. The GaN capping layer thickness is about 50nm. The PL spectra at different temperature were plotted in Fig 4.38a. As mentioned previously, the emission with energy above 2.8eV is due to the GaN layer. The 2.4eV emission dominates all the spectra measured at different temperature. In the PL spectra from 4K-125K, similar to #1184, but a very weak emission shoulder could be distinguished at 2.6eV. It disappeared when the temperature rose above 150K. The pure Gaussian like 2.4eV peak occurred in the spectra above 150K. Fitting of the relation of the peak intensity versus 1000/T (Arrenhius plot in Fig.4.38b) gives the activation energy of the 2.4eV peak of 67meV, which is identical with the value got from the 2.4eV PL peak in the $In_xGa_{1-x}N$ sample #1184 with x=0.06. Moreover, the “bulk” InGaN or average band gap is 2.80eV for In mole fraction of 13%. This hints to the fact that the 2.4eV emission peaks in these two samples come from the InGaN localized structures with the same band profile.

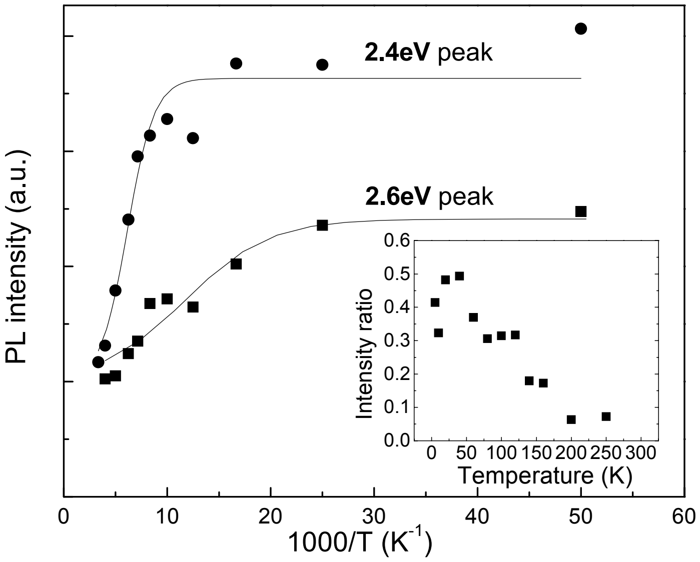

Figure 4.37 PL intensity of the 2.4 eV and 2.6 eV peaks got by fitting versus 1000/T (Arrenhius plot). Inset is the intensity ratio of 2.6 eV peak to 2.4 eV peak versus temperature.

The 2.4eV peak energy fitting by Gaussian functions was plotted versus the temperature in Fig.4.38c. The emission peak at round 2.4eV showed a slightly “S” shape behavior with increasing temperature, but within a smaller temperature range. This is an evidence for localized states in InGaN. Above 50K, the emission energy fits very well the temperature induced energy gap variation (from eq. 4.12). All the temperature dependent PL results shown above indicate that there are probably two kinds of localized structures with two preferred In composition in the InGaN. At “low” In content samples, the localized structures with 2.4eV and 2.6eV emission are both present, whereas, in “high” In content InGaN, the structure with the 2.4eV emission is preferred. Both emissions are well below the measured “bulk” InGaN band gap. There are theoretical speculations on the ordered phase in cubic InGaN. In the paper published by Teles et al[110], the formation of the ordered phases has been calculated by employing the first-principle total energy calculation, a concentration-dependent cluster-based model, and Monte Carlo simulations. They predicted that the biaxial strain suppresses phase separation and acts as a driving force for chemical ordering in c-$In_xGa_{1-x}N$ layer. This conclusion can be a good interpretation for the “pinned” 2.4eV PL emission energy in our InGaN samples.

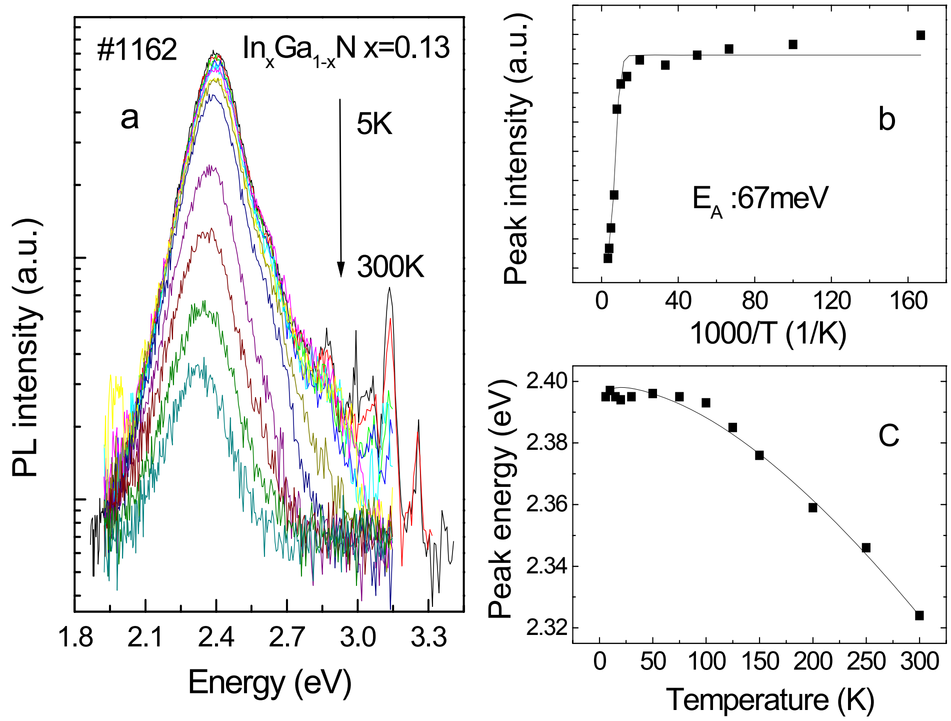

Figure 4.38 a) PL spectra of $In_{0.13}Ga_{0.87}N$ DH#1162 from 5K to 300K, b) PL peak energy versus 1000/T, the Arrenhius plot, c) PL peak energy versus temperature.

4.7.4 Depth resolved cathodoluminescence measurements

Cathodoluminescence is a powerful method to investigate the optical properties of InGaN based structures. Due to the small dimension of the focused electron beam, the spatial resolution of the CL can be very high up to several tens of nanometer. By changing the acceleration voltage, the detection depth can be varied to get the information within the sample along the growth direction. In semiconductor structures and devices, we need to have multiple layers along the growth direction, such as heterojunction and multiple quantum wells. CL is a very helpful tool to evaluate the depth and spatial resolved optical properties of these complicated structures. We have performed the depth resolved CL measurements on our InGaN samples. The detail of our CL equipment has been described in chapter 2.

The InGaN samples investigated here are grown on GaAs and 3C-SiC, respectively. InGaN #868 is a 130nm $In_{0.05}Ga_{0.95}N$ layer grown on a 600nm GaN buffer layer by using a GaAs substrate. The focus mode CL measurement was performed with a constant emission current of 350mA and different acceleration voltage.

Figure 4.39 shows a room temperature CL spectra measured on InGaN sample #868. In this figure, two dominant emission peaks were clearly found in all the spectra with the energy about 2.55eV and 2.8eV at different acceleration voltage. These two peaks are ascribed to the InGaN emissions. The GaN emission peak (3.2eV) is only visible when the acceleration voltage is higher than 6kV. The relative PL intensity of the 2.8 eV peak increases with the acceleration voltage, i.e. the penetration depth.

The range of the electron penetration depth was estimated by the model introduce in chapter 2. The electron distribution with different voltage is schematically drawn in Fig.4.40.

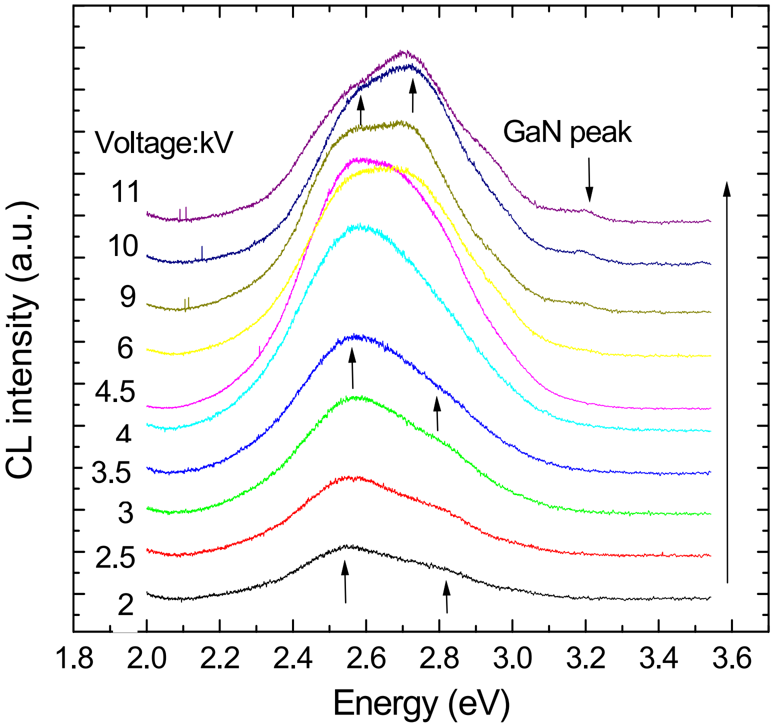

Figure 4.39 Depth resolved CL spectra on $In_{0.05}Ga_{0.95}N$ #868

The pesudo-Voigt functions have been used to fit the depth resolved cathodoluminescence spectra. The derived dominant two peak energies versus the penetration depth are shown in Fig 4.41. The squares denote the high energy 2.8eV peak, and the circles stand for the low energy peak 2.5eV peak. The InGaN #868 sample structure also is shown in this figure by the bar graph. The horizontal length of the bar denotes the thickness of the InGaN and GaN layer.

From this graph, one can clearly see that both the two peak energies increase with the depth at beginning, and reach a maximum at 130nm, which is the position of the InGaN/GaN interface.

When the depth increases further, the two peak energies start to decrease until the penetration depth reaches 380nm, then both peak energies stay constant at about 2.7eV. For the whole detection depth, the energy shift is about 110meV for the high energy peak and 60meV for the low energy peak.

From all what we have found, we come to a similar conclusion, which is also shown in the PLE and temperature dependent PL measurement, namely that there exist In rich clusters in the InGaN layers with a distribution along the growth direction.

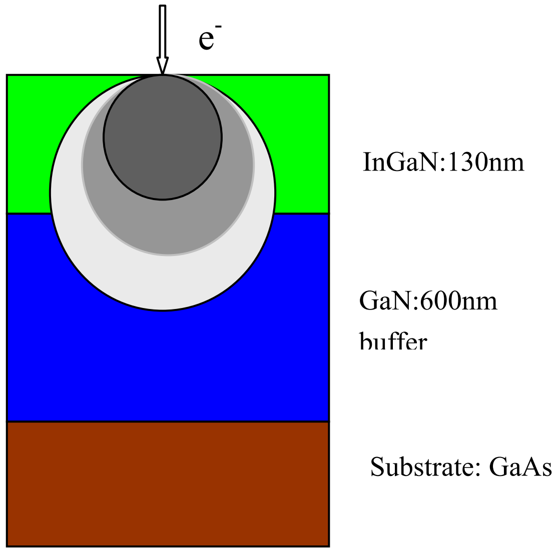

Figure 4.40 Schematical drawing of electron distribution in the InGaN samples.

As the acceleration voltage increasing, i.e. the detection depth, the CL intensity of the high energy peak starts to dominate the spectra. This leads to a conclusion that the In rich InGaN clusters are close to the InGaN surface. When the detection depth is shallow at low voltage, the excited carriers are distributed mostly in the InGaN layer and they can diffuse into the In rich clusters close to the surface. By increasing the voltage, most of the carriers are generated in the GaN buffer layer, and then diffuse into the InGaN side, but close to InGaN/GaN interface. In the meantime, the excited carrier quantity near the InGaN/GaN interface also increases due to the increase in diameter of the electron distribution sphere.

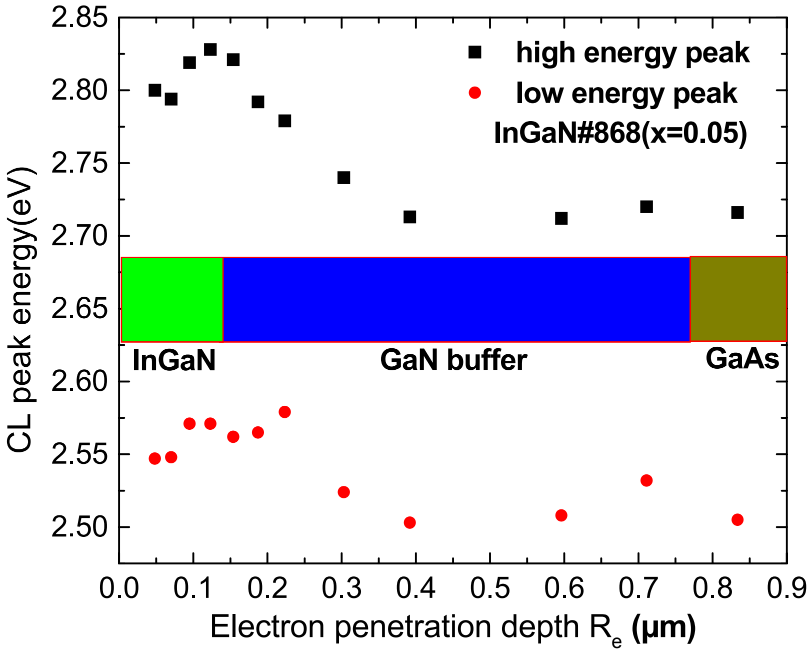

Figure 4.41 CL emission peak energy versus electron penetration depth.

This indicates that compared to the In rich InGaN phase close to the surface there are InGaN layers with relatively low In content phase close the InGaN/GaN interface.
The integrated intensity ratio of the 2.8eV peak to 2.5eV peak is plotted in Fig.4.42 versus the penetration depth. This ratio increases with the penetration depth, showing that the high energy peak starts to dominate the CL spectra when the depth exceeds 0.3-0.4 μm, corresponding to the acceleration voltage of 6kV.

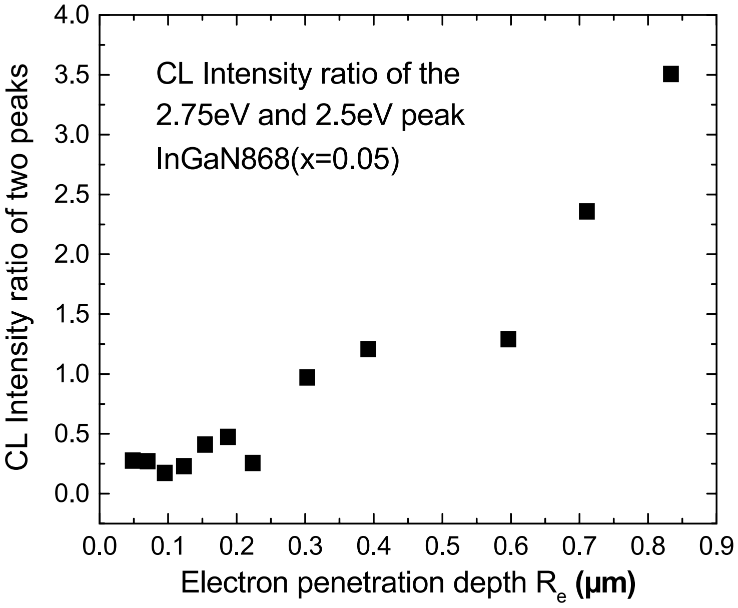

Figure 4.42 CL intensity ratio of 2.8 eV peaks to 2.5 eV peak versus the electron penetration depth.

The same experiments were also performed on the InGaN samples grown on SiC substrates with a lower emission current of 180mA. The $In_xGa_{1-x}N$ DH#1231 sample with x=0.184 and thickness of 14nm was grown at a substrate temperature of 610°C by using 3C-SiC substrate.

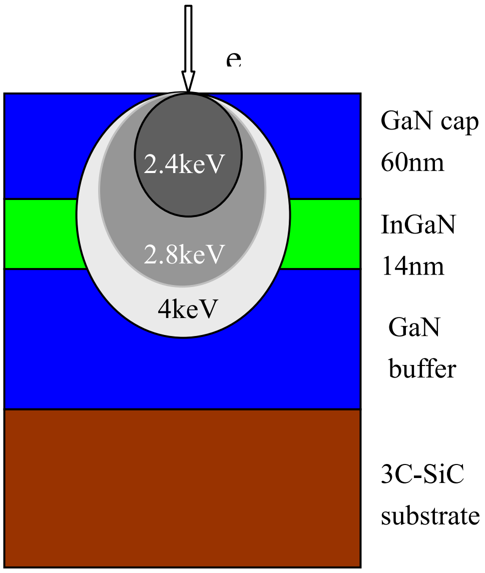

Figure 4.43 Distribution of the electrons in InGaNDH#1231 at various voltages.

The GaN capping layer thickness is 55nm and the buffer layer 600nm. The sample structure and the penetrated electron distribution are depicted in Fig.4.43. Figure 4.44 shows the room temperature CL spectra at different acceleration voltages. The single emission peak feature remains in every spectrum. In the spectra detected with a higher voltage than 6kV, the GaN emission peak appears at 3.2 eV. Unlike the clear two peaks in the sample #868, the InGaN emission peak is more likely to be one peak but with a strong asymmetry. Two pseudo-Voigt functions were used to fit the spectra. The peak positions are plotted with the detection depth in Fig. 4.45. The squares denote the main emission peak. The circles show the emission tail (as show in the inset of the figure). Similar to the peak variation in the CL spectra of InGaN#868, the main emission peak also shows a blue-red- shift when the detection depth is close to the InGaN /GaN interface.

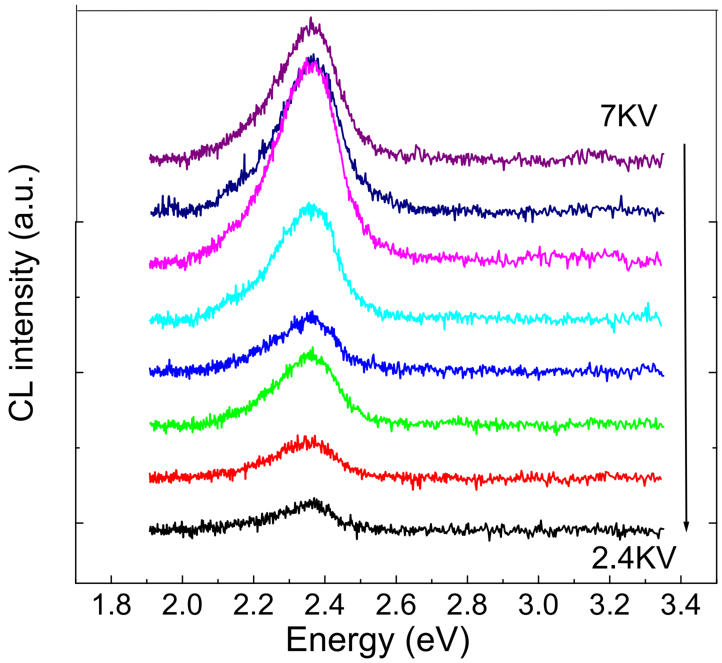

Figure 4.44 Room temperature depth resolved CL spectra from InGaNDH#1231.

The total energy shift is only 20meV, much smaller compared to the 110meV in the measurement on the InGaN#868 sample.

For the peak energy shift with the penetration depth, one may assign the shift in these two samples to the variation of the In concentration along the growth direction. However, exactly the same behavior of the emission peaks from these two samples encourages us to seek an alternative explanation. Here, we tentatively ascribe the energy shift with the detection depth to the band filling, i.e. the Burstein–Moss effect and the band gap shrinkage by heating from the increasing of the acceleration voltage. This conclusion is upheld by the fact that the smaller peak shift of 20meV in sample #1231 is found to be due to the small current of 180mA exerted on this sample, which is about half of that on sample InGaN #868 with 350mA.

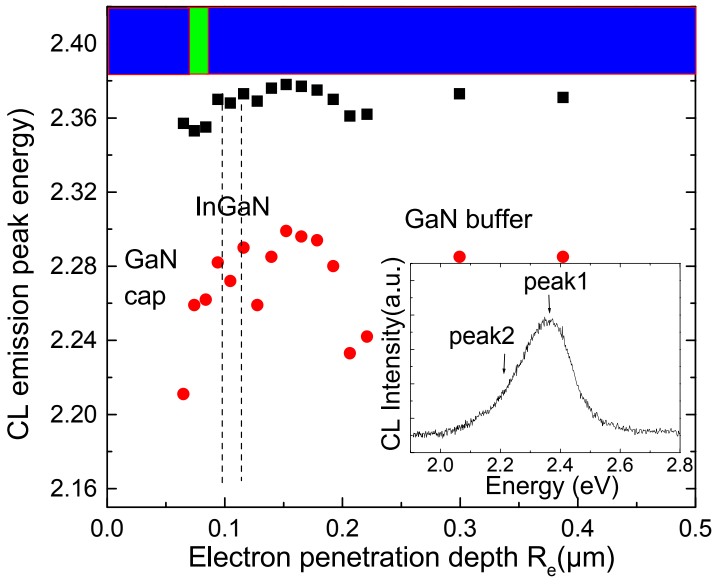

Figure 4.45 CL emission peak energy versus penetration depth from depth resolved measurement on InGaN#1231 (x=0.184).

4.8 Thermal annealing results of c-InGaN.

A cubic III nitride is a meta-stable compound, which means that it is not favorable in the high temperature epitaxial growth. On the other hand, in both hexagonal and cubic InGaN, some researchers have found the separated phases due to the immiscibility of InN and GaN[186,187]. In our MBE grown cubic InGaN samples, phase separation has not been found from the XRD measurement results.

Theoretically, phase separation is a thermodynamic equilibrium, whereas MBE is a non-thermodynamic equilibrium growth process. It is argued that if enough driven force is supplied, i.e. thermal annealing, the phase separation could occur within the MBE grown InGaN layers [112, 188]. To study the thermal stability of cubic InGaN and check the phase separation effect, we have performed thermal annealing experiments on the as-grown cubic InGaNDH sample #1224. The annealed InGaNDH #1124 sample contains an InGaN active layer with a thickness of 40nm and an In mole content of 0.07. The GaN capping layer thickness is 35nm and the buffer layer thickness is 500nm. This sample was placed in a DHS 900 “Domed Hot Stage” closed-type chamber with N_2 gas ambient atmosphere, keeping the pressure at 0.5bar. The temperature exerted on the InGaN sample increased from 800°C to 900°C at steps of 50°C. The annealing temperature and the time was plotted in Fig. 4.46. The XRD reciprocal maps were shown in Fig 4.47 to demonstrate the structural properties at different annealing stages. At the beginning, the InGaN reflex is well separated from GaN reflex. During every stage, either the shape of the GaN and InGaN reflex or the distance of these two diffraction reflexes has no change.

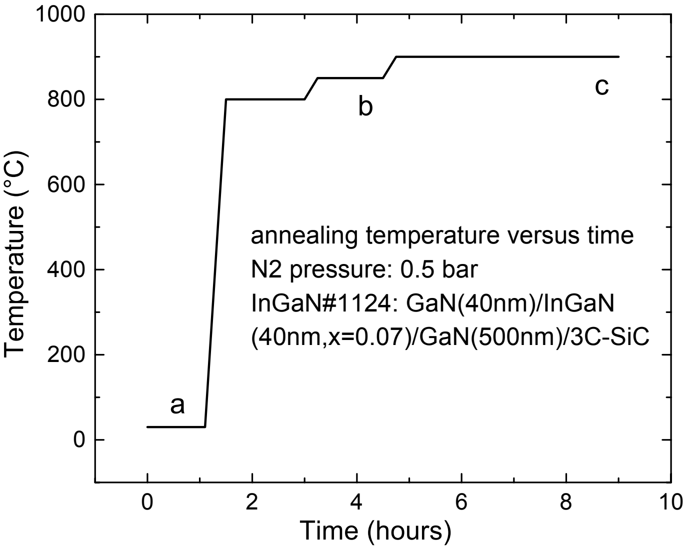

Figure 4.46 Annealing temperature on InGaN sample versus keeping time.

No additional peak appeared after each annealing stage, indicating no detectable InGaN separated phases existed after the annealing and showing the stability of the c-InGaN layer up to 900°C.

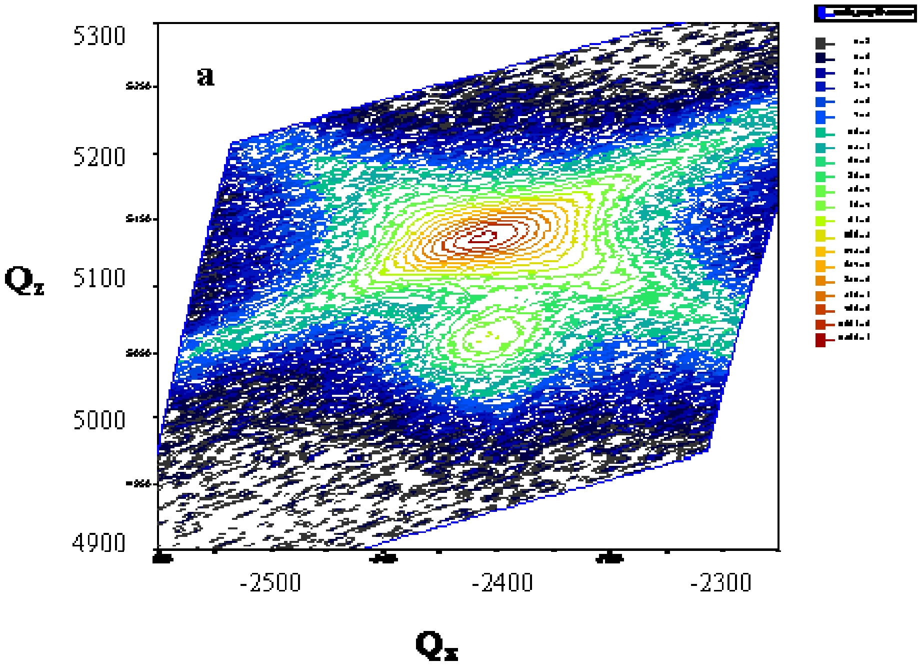

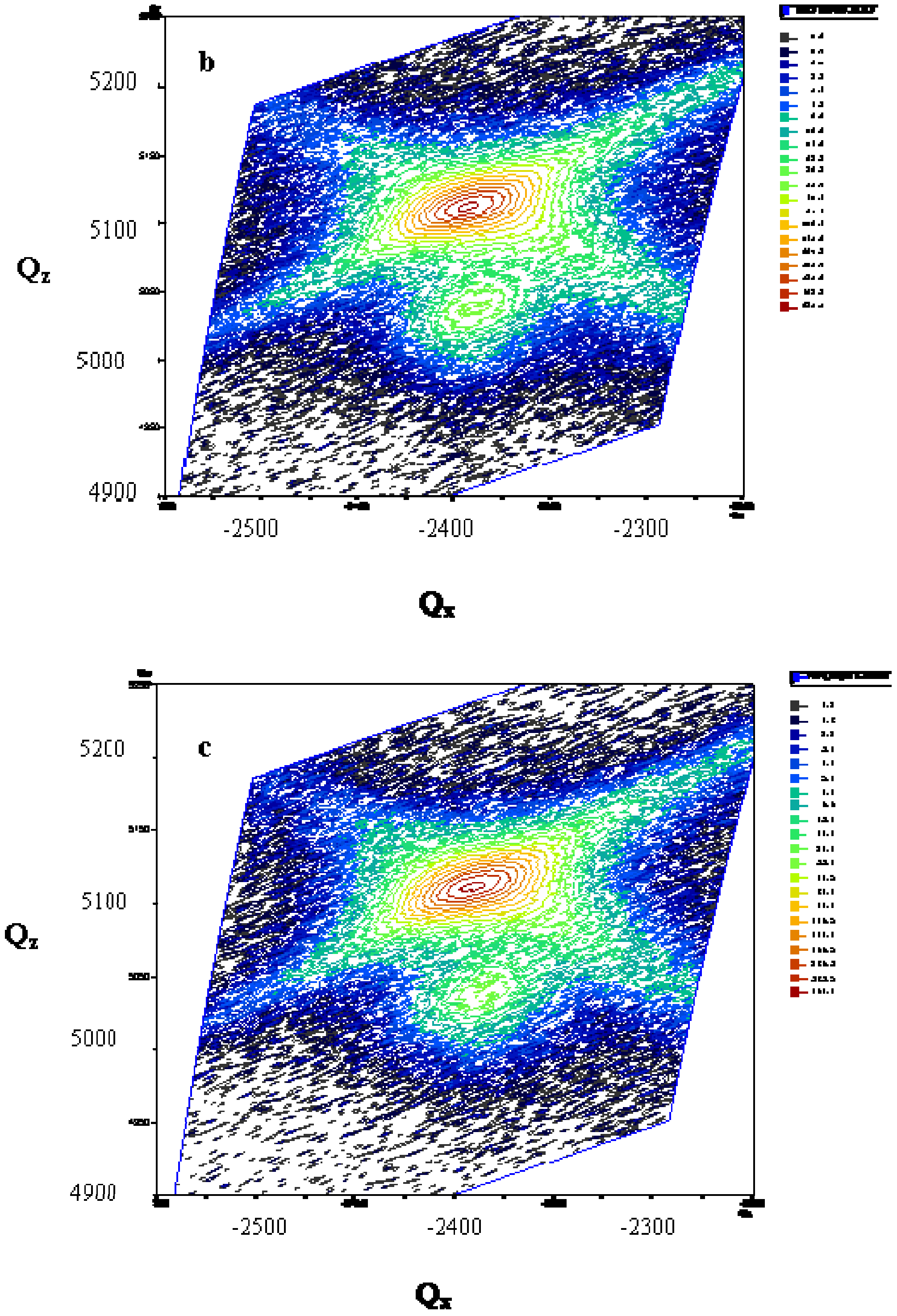

Figure 4.47 (-1-13) Reciprocal space maps on annealed sample InGaNDH#1124 at different stages. a) before annealing, b) at end of 850°C, c) at end of 950°C, indicated in Fig. 4.46.

Room temperature PL spectra were also measured on this sample before and after annealing, shown in Fig.4.48. Both PL spectra are dominated by the Gaussian like InGaN emission peak. No additional peaks are found except the InGaN and GaN emission peaks, which also revealed that there is no trace of separated phases by PL measurement. The InGaN emission energy has a slight blueshift of about 15meV, which may come from the local In content redistribution induced by the thermal annealing. The FWHM of the InGaN emission is 375meV in the InGaN PL emission after annealing. This is nearly identical with measurement before annealing (370meV).

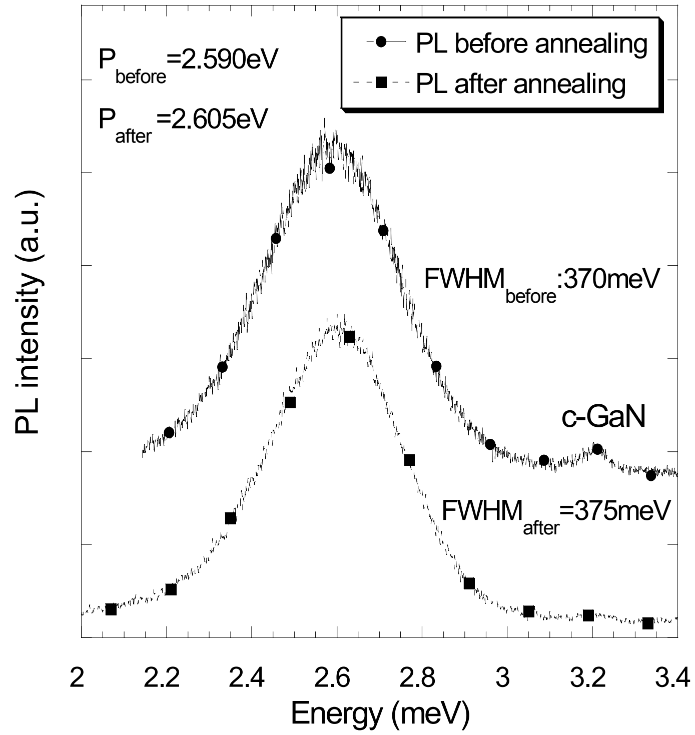

Figure 4.48 Room temperature PL spectra from the InGaNDH#1124 before and after thermal annealing.

Both HRXRD and PL results show no change after the thermal annealing experiments. Therefore, I suppose that the spinodal phase separation may not occur in our InGaN samples. The thermal annealing does not induce phase separation, indicating the stability of our c-InGaN layer.

5. Growth and properties of c-InGaN/GaN QWs and application

High quality InGaN/GaN quantum wells are widely employed active structure in high brightness LED and high efficiency laser diodes due to its superior properties compared to the homojuction and heterojunctions [1]. Firstly, quantum wells have great capabilities to capture carriers and exhibit strong confinement of electrons and holes. Room temperature GaN band gaps are 3.4eV (hexagonal) or 3.2eV (cubic). InGaN band gap may be varied from 0.7eV (0.6eV) to band gap energy of GaN. For blue (470nm) and green (520nm) emissions, large InGaN/GaN bandgap offset (0.76eV for blue and 1eV for green) gives rise to highly efficient confinement of the carrier by increasing the In concentration in the InGaN quantum wells. Secondly, a quantum well of small dimensions results in high amplitude overlapping of the carriers' wave function, which leads to high recombination efficiency. The multi-quantum wells further enhance these two effects due to an increase in the number of wells. Consequently, the high internal quantum efficiency is realized by these superior properties from the multi-quantum wells.

Cubic InGaN/GaN MQWs growth and characterization will be reported in this chapter. A brief introduction on the application in resonant cavity LEDs is also demonstrated.

5.1 Quantum size effect in finite depth quantum well

Due to the quantum size effect, the k vector along the confinement direction is quantized and split to several discrete energy levels.

The quantum well energy varied with well thickness may be calculated as follows:

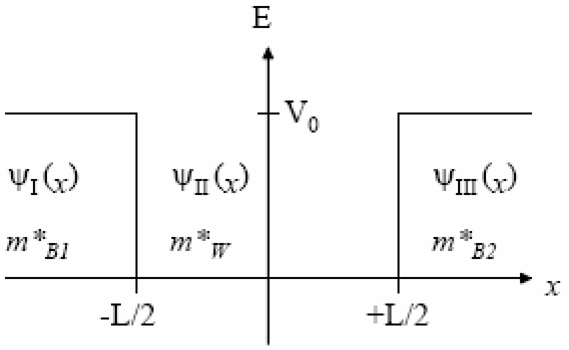

Figure 5.1 Finite depth quantum well conduction band profile.

Consider an electron in the conduction band of the quantum well of width L and a finite well height of V_0. This finite well height is equal to the band offset of InGaN well and GaN barrier distribution in the conduction band (Fig.5.1). The electron effective mass in the well is m_W^*, and is m_B^* in the barrier (in this case barrier 1 and 2 are both c-GaN).

The wavefunction $\psi(z)$, must be satisfied with the Schrödinger's equation in the quantum well given by:

$$\left[-\frac{\hbar^2}{2m^*}\frac{\partial^2}{\partial z^2}+V_0(z)\right]\Psi(z)=E_n\Psi(z) \tag{5.1}$$

Schrödinger's equation requires that the wavefunction, $\psi(z)$, be continuous at the edges of the QW, that is, at $x = \pm L/2$. It can be shown that the corresponding derivatives $(1/m^*)\,\psi'(z)$ must also be continuous at these boundaries.

Assuming the from of the $\psi(z)$ as following:

$$\begin{aligned}\Psi_1 &= A*e^{\beta*z}\\ \Psi_2 &= B\cos(\alpha z)+C\sin(\alpha z)\\ \Psi_3 &= D*e^{-\beta*z}\end{aligned} \tag{5.2}$$

Where $\alpha=\frac{1}{\hbar}\sqrt{2m_w^*E}$ and $\beta=\frac{1}{\hbar}\sqrt{2m_B^*(V_0-E)}$, put the wavefuction into the boundary condition. Through algebraic manipulation, one may arrive the following wavefunction in the quantum well:

Case 1:

$\Psi_2(z)=B\cos(a*z)$ (C=0 symmetric solution)

from the boundary condition the following relation can be obtained:

$$\cot\left(\alpha*L/2\right)=\left(\frac{m_B^*}{m_w^*}\right)\frac{\alpha}{\beta} \tag{5.3}$$

The symmetric solution with E_n (n = 0,2, 4, 6…) can be calculated from this equation.

Case 2:

$\Psi_2=C\sin(\alpha*z)$ (B=0 asymmetric solution)

the relation between α and β can be expressed in 4.:

$$-\tan\left(\frac{\alpha*L}{2}\right)=\left(\frac{m_B^*}{m_W^*}\right)\frac{\alpha}{\beta} \tag{5.4}$$

Numerical calculation may give the asymmetric solution with corresponding energy level E_n (n = 1, 3, 5, …) from this equation.

Ground state calculation:

Through this calculation assuming the same effective mass in well and barrier, the ground state solution for a finite potential well is the lowest even parity state and can be expressed in the form

$$\beta=\alpha*\tan\left(\alpha*L/2\right) \tag{5.5}$$

Since both sides of the equation are dependent on the energy E for which you are solving, the equation is transcendental and must be solved numerically.
One way to estimate the ground state energy of a finite potential well is to use the infinite well energy to produce a trial attenuation factor β. Then the value of β can be refined by iteration to get an effective well width and a numerical solution for the energy.

5.2 Sample description

We have grown cubic InGaN/GaN single and multiple quantum wells and studied the growth and properties of these cubic InGaN/GaN SQWs and MQWs.
The InGaN/GaN SQW and MQW were both grown on GaAs and 3C-SiC substrates. Figure 5.2 is the schematic drawing of the structure for c-InGaN/GaN SQW and MQWs samples. For the single quantum well, the capping layer thickness is about 40nm and the InGaN thickness can be varied. All the MQWs samples have 6 InGaN quantum wells without a thick GaN capping layer on top of the MQW structures.
Two series of c-InGaN/GaN SQW samples were grown for investigating the optical properties of the quantum well. One series of InGaN SQW was grown on GaAs substrate, while the other series was grown on 3C-SiC substrate. The well thickness was varied from 4nm to 24 nm, which was estimated from the InGaN growth rate. The GaN capping layer thickness in both cases is approximately 50nm. The In mole content for InGaN SQW grown on both substrates is approximately 7%.

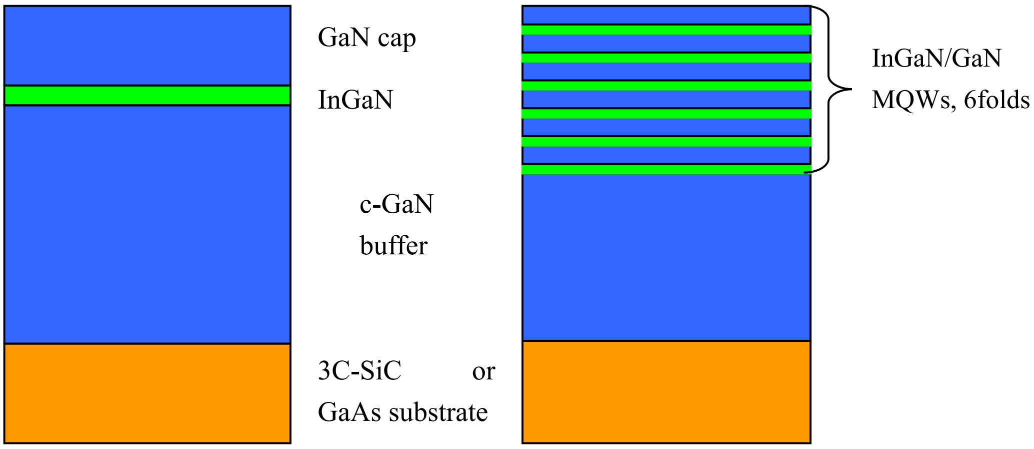

Figure 5.2 Schematical drawing of InGaN/GaN SQW and MQW samples

5.3 Optical properties of c-InGaN/GaN single quantum well

The PL spectra from InGaN/GaN SQW samples grown on GaAs substrate with different well thickness are shown in Fig. 5.3. In all the spectra, the InGaN emission contains two or three peaks, which appear below 3.0eV in emission energy. The dominant peaks lie between 2.5-2.7eV in spectrum of sample #901 with 40nm well thickness. In Fig 5.3, a strong blue shift of these two peaks occurs as the well width is decreased except the spectra from sample #931 and #933. However, the intensity ratio of high energy peak (2.8eV) to low energy peak (2.6eV) in the spectrum of sample #933 with a 6nm InGaN well, is larger than in the spectrum of sample #931 with a 9nm InGaN layer.

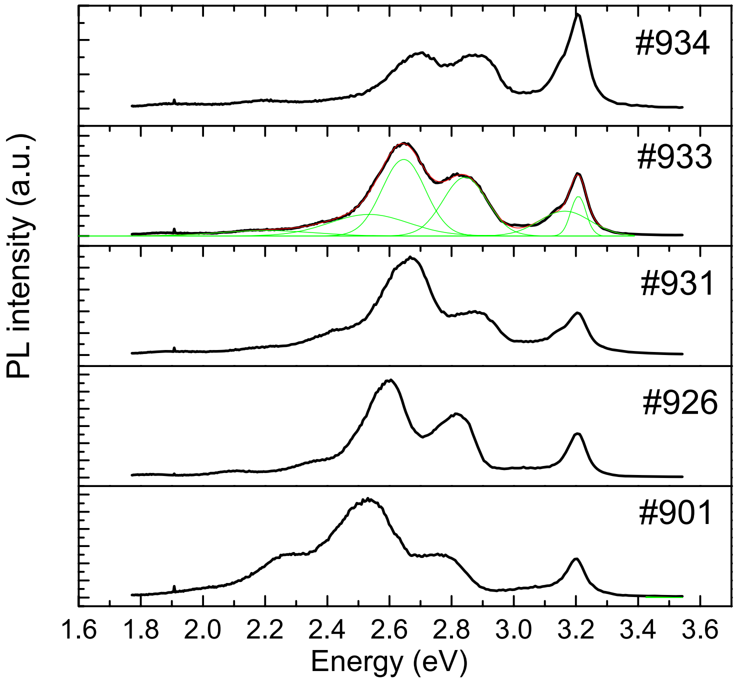

Figure 5.3 Room temperature PL spectra of InGaN/GaN single quantum well with different well thickness grown on GaAs substrate.

The weighted emission peak energy from sample#933 is therefore higher than that from sample#931.

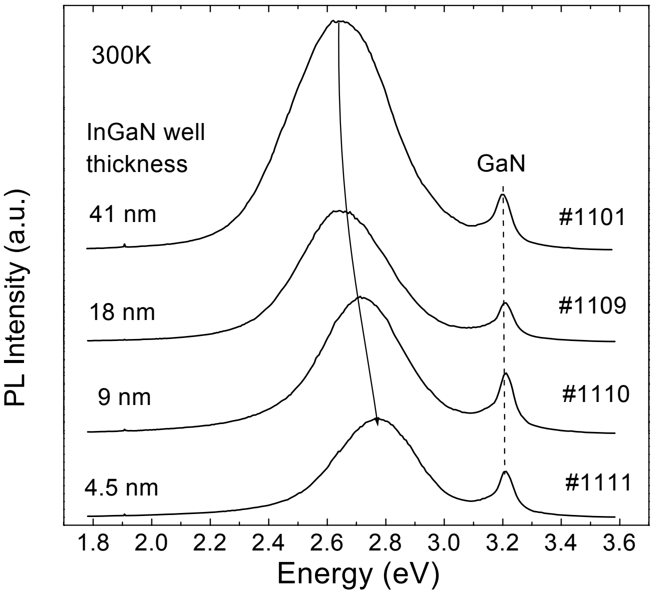

Figure 5.4 Room temperature PL spectra of InGaN/GaN single quantum well grown on 3C-SiC substrate. The In mol content is 7.3% in the well

The InGaN emission peaks were resolved by fitting two or three pseudo-Voigt functions (e.g. #933 in Fig. 5.3) and plotted in Fig. 5.5 versus the well thickness.

Both two peaks (open circle and triangle in Fig.5.5) show strong red shift with increasing of the well thickness, which hints these two peaks come from the InGaN wells. For estimation of the blue shift due to the quantum size effects, numerical calculations have been performed (assuming the InGaN effective gap energies are the PL emission peak energy) to get the peak energy with well thickness. This is reasonable due to the localized structures existing in InGaN. The band offset ratio of conduction band to valence band is adopted as 2:1, according to the frequently employed data [189]. The effective electron and hole mass in InGaN is extrapolated from the value in GaN and InN applying Vegard's law, which shown in table 4.1. Both the 2.8 eV and 2.5 eV peaks fit well with the theoretical calculations except the sample with 9 nm InGaN (#931). Multi-peaks features in the PL spectra of the quantum well emission also appear in the spectra of the thick InGaN layer or double heterostructures. According to the PLE and CL measurement results in chapter 4, this makes one believe that there are also different In content InGaN phases in the InGaN well layer.

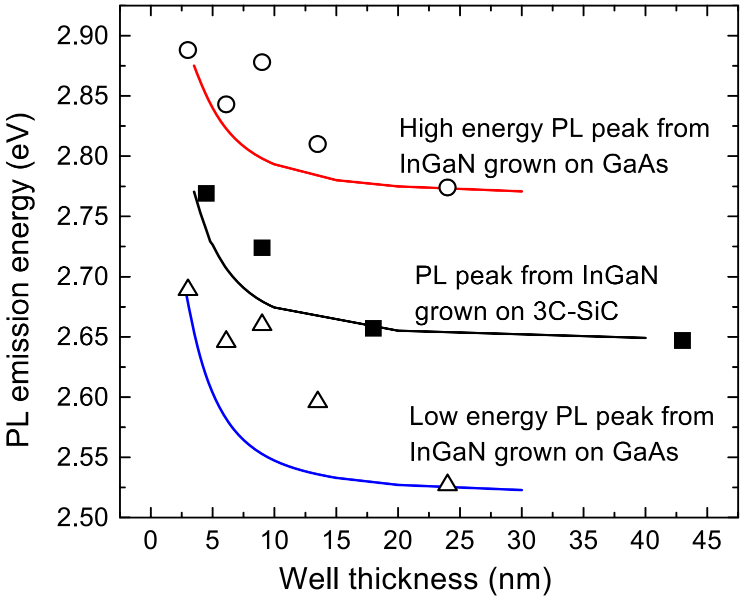

Figure 5.5 Calculated transition energy in the quantum well with well thickness and measured PL emission energy of the InGaN/GaN quantum wells.

The second series of $In_{0.07}Ga_{0.93}N$ SQW was grown on the 3C-SiC substrate with a well thickness of 4.5 to 41nm. The room temperature PL spectra from this series of InGaN SQW samples with different well thickness were measured under the same PL setup and similar He-Cd laser power with a fluctuation of less than 10% (shown in Fig.5.4). The PL spectra show relatively sharp, single emission peak feature, revealing better optical quality of the InGaN quantum well grown on low lattice mismatch 3C-SiC substrate. The InGaN emission peak has obviously blueshifted with decreasing well thickness. The peak PL energy versus well thickness from InGaN/GaN SQW samples was plotted in Fig.5.5 (black squares). Similar calculation about the blue shift has been also performed which is indicated by the black line in Fig. 5.5. As seen in the figure, these calculated results are slightly below the experimental data.

5.4 Photoluminescence intensity with well thickness

Due to the spontaneous and piezoelectric polarization field in hexagonal InGaN active layers, electrons and holes which trapped by the quantum well will be effectively separated by the electric field on two opposite sides of the quantum well. The overlap of the electron and hole wave function decreases as the well's size is increased, which results in lower PL intensities and a red shift of emission energy. This phenomenon called quantum confined stark effect (QCSE) has been proven by Chichibu [190]. For this reason, the optimal h-InGaN quantum wells thickness in devices application was typically set as 2-3nm [116,191,4]. Contrary to the hexagonal system, cubic InGaN's higher crystal symmetry results in no polarization field. Thus, no deterioration of PL intensity is expected with thick InGaN wells.

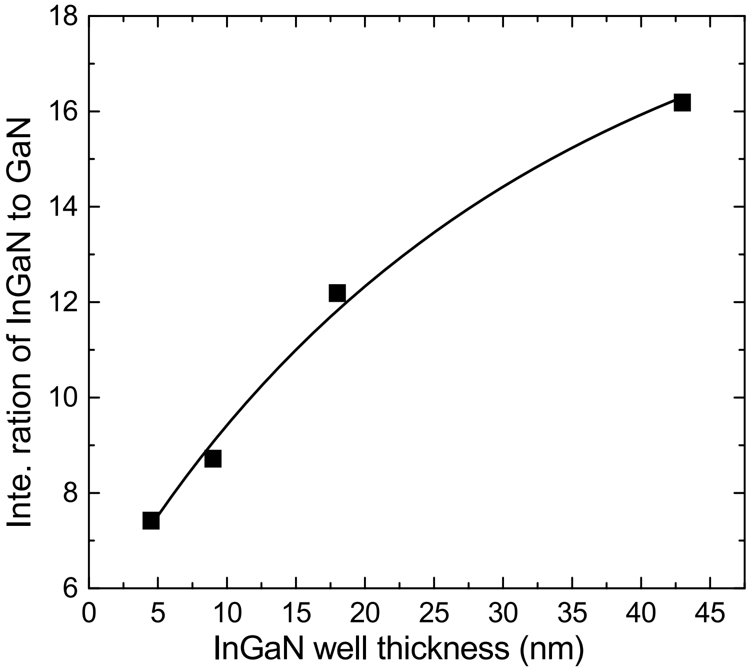

Figure 5.6 Integrated PL intensity ratio of the InGaN SQW samples versus the InGaN well thickness.

For the room temperature PL spectra shown in Fig.5.4, after calibrating the InGaN PL emission intensity with excitation power, the PL integrated intensity ratio of peak InGaN to peak GaN was plotted in Fig.5.6 versus the well thickness. Due to the same GaN capping layer thickness, this ratio denotes the normalized InGaN PL intensity. It is clear in this figure that this ratio increases with the well thickness, which is evidently opposite to hexagonal InGaN results [115], where the PL intensity decreases with well thickness due to the QCSE. Our results reveal that the thickness of c-InGaN/GaN quantum well can be varied in a wide range in order to yield optimum recombination efficiency.

5.5 Cubic InGaN/GaN multiple quantum wells

5.5.1 Growth interruption in c-InGaN/GaN quantum wells

Six periods of InGaN/GaN MQWs were deposited on a 700nm thick c-GaN buffer layer by using 3C-SiC substrates. The barrier thickness was 10nm and the well thickness was 4nm. InGaN layers were deposited under In-rich conditions at a growth temperature of 610°C. Two different growth procedures were employed. For type A samples, after the well growth, the InGaN well layers were covered by a few nanometer thick GaN layer at 610°C, then the temperature was ramped up to a GaN growth temperature of 720°C to grow the rest of the barrier. For type B samples, growth was interrupted between the well and the low temperature GaN barrier growth. All other growth conditions remained constant.

Figure 5.7 shows the RHEED patterns of the InGaN surface obtained before and after growth interruption. The RHEED patterns of A and B samples were spotty during the InGaN growth.

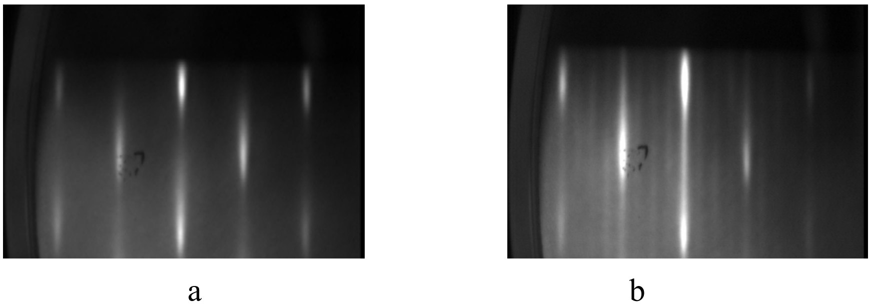
a b

Figure 5.7. RHEED pattern of the InGaN growth, a) before growth interruption, b) after growth interruption

Following the growth interruption in type B samples, we observed a (1 × 4) reconstruction and a streaky pattern, which indicates a smooth surface. The intensity of the RHEED pattern also increased after interruption. It is supposed that this is due to the evaporation of In atoms from the surface during growth interruption. HRXRD (-1-13) reciprocal space maps revealed that the InGaN wells in all samples were pseudomorphically grown on GaN barrier layers. A typical (-1-13) map is shown in Fig. 5.8. HRXRD (002) ω-2θ line scans of one type A (#1213) and one type B (#1212) samples are shown in Fig. 5.9. The superlattice peaks are clearly resolved, indicating good interface quality for both types of samples. The measured data have been fitted by a full-dynamical simulation, shown as full curves in Fig.5.9. The effective well thickness and the average In molar fraction were obtained from the simulation. Type A sample #1213 had a well thickness of about 4.4nm and an average In molar fraction of 13.7%. Type B sample #1212 had a lower In molar fraction of 12.1%, and a well thickness of 3.7nm.

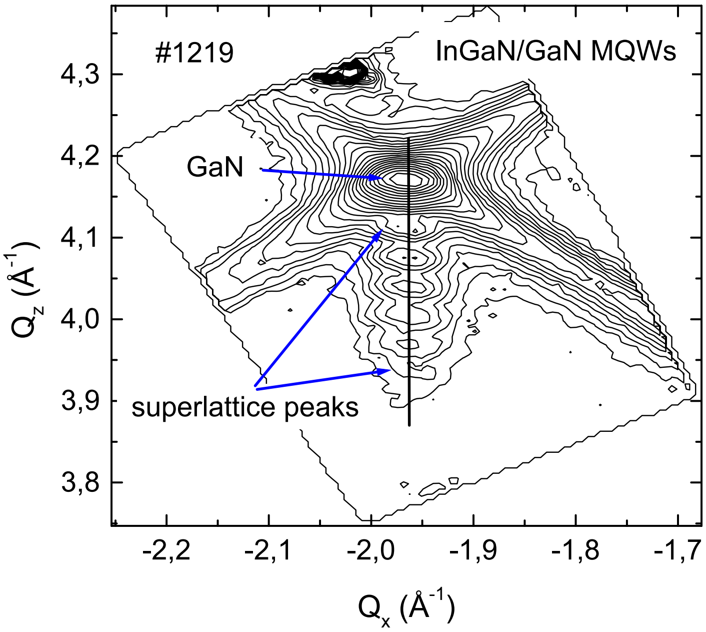

Figure 5.8 HRXRD (-1-13) reciprocal space map on InGaN/GaN MQWs.

I suggest that the observed differences are due to In segregation. After the InGaN well growth, an In metal layer remains on the InGaN surface. Without growth interruption (type A samples) the In atoms stay on the surface.

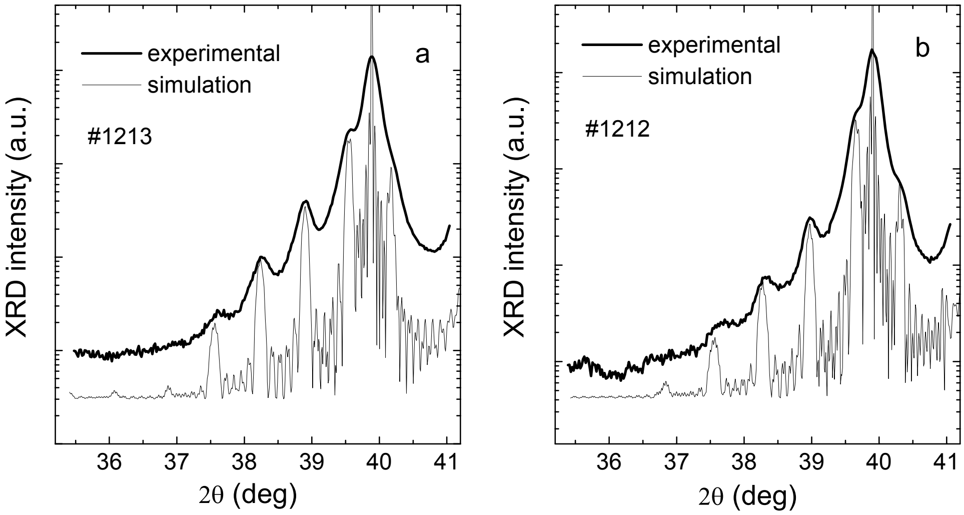

Figure 5.9 HRXRD (002) ω-2θscans of a) type A sample, b) type B sample.

During the low temperature GaN layer growth, the In atoms will be absorbed into the GaN barriers yielding a larger InGaN well thickness and a higher In molar fraction. In contrast, during the growth interruption of type B samples, the In metal layer can evaporate from the surface. Figure 5.10 a) and b) show the room temperature PL spectra of type A sample #1213 and type B sample #1212, respectively. The InGaN emission is dominant in all spectra.

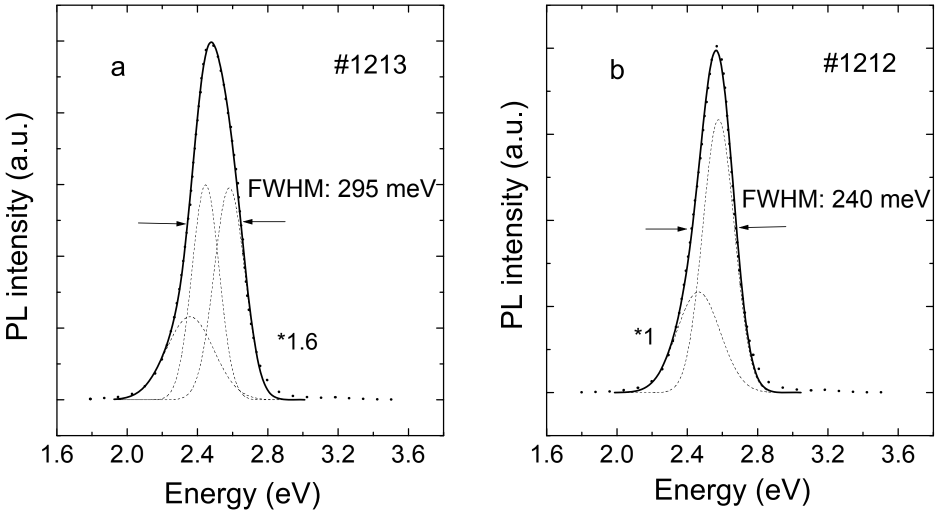

Figure 5.10 Room temperature PL spectra of the two different type of samples. a) type A, b) type B

No emission from the GaN barriers is observed demonstrating high recombination efficiency of our c-InGaN MQWs. Gaussian functions were used to fit the PL spectra. The emission of the type A sample #1213 is asymmetric and can be fitted by two Gaussian peaks and a weak peak for the band tail-like contribution. The PL emission peak from type B sample #1212 has a reduced line width (FWHM) and can be fitted with only one dominant Gaussian peak and also a weak additional peak. It is believe d that the second dominant emission of type A samples is due to recombination of e-h pairs in a region of high In content InGaN layer formed by segregated In at the InGaN/GaN interface.

These samples suggested that the growth interruption after InGaN wells growth will help create more homogenous InGaN wells by avoiding the In surface segregation layer.

5.5.2 Simulation of X ray diffraction patterns

In the MQWs structure, if the structure of each period of the MQWs is identical, the MQWs structure can be treated as a repeated structure with period of the well thickness plus barrier thickness. This repeated structure is called a superlattice. The “lattice constant” of this superlattice is the period of the quantum well, which is normally tens of times larger than the material’s lattice constant. In reciprocal space, the reciprocal lattice thus has tens of times smaller distance between the different lattice points.

Figure 5.11 shows the XRD diffraction line scan on InGaN/GaN MQW#1219 around GaN (002) and (004) reflexes. The GaN peak is marked in this figure. Adjacent to that are multi-peak structures, which are clearly distinguished. These are the so-called superlattice peaks. From this superlattice peaks, one may deduce the period of the MQW, that is, the well and barrier thickness and the In mole content in these InGaN wells.

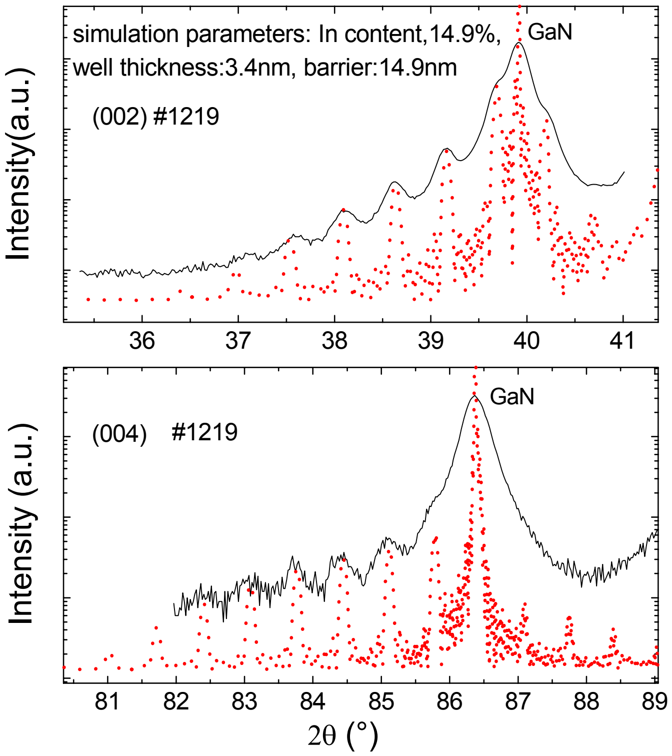

Figure 5.11 The ω-2θ of (002) and (004) reflex of the InGaNMQW1219 sample. Also shown in the graph are the results of full dynamic simulations

The thickness of the period may be found as follows:

$$d = \frac{n * \lambda}{\sin\theta_n - \sin\theta_0} \tag{5.6}$$

where n is the order of the superlattice peak and λ is the wavelength of the X-ray beam. In this case, the wavelength of the x-ray beam is Cu K_a line which is 1.54056Å. θ_n is the diffraction angle of n^{th} order superlattice peak. This 0^{th} superlattice peak is the one with maximal intensity in all the superlattice peaks. After getting the period of the superlattice, the lattice constant of the well material, InGaN normal to the surface can be calculated as follows:

$$a_{InGaN} = \left(a_{s0} - \frac{a_{GaN} * d_{GaN}}{d_{period}} \right) * \left(\frac{d_{period}}{d_{InGaN}} \right) \tag{5.7}$$

Where a_{InGaN} is the lattice constant of InGaN well along the growth direction, A_{s0} is the average lattice parameter calculated from the 0^{th} superlattice. d_{GaN} is the barrier thickness, which is estimated by the GaN growth rate and the growth time, and d_{InGaN} is the InGaN well thickness, which includes the strain status. Applying Vegard's law one can carry out the In molar content in the InGaN quantum well.

For more accurate determination of the structural parameters, a full dynamic simulation program was employed to simulate the XRD measurement curve by varying the input parameters. The full dynamic simulation includes the X-ray multiple scattering and the refractive index difference between air and the material, which are neglected in the kinetic model [151]. The dotted curve in the Fig. 5.11 is calculated by using the full dynamic simulation program. In the experimental curve, the GaN diffraction peak is broad due to the defect in the GaN buffer layer. Consequently, the broad GaN diffraction peak modifies the maximum position and intensity of the superlattice peaks due to the GaN background. This could influence the judgment of whether the fitting curve agrees to the measured curve and deliver errors in the simulation result.

To overcome this problem, one can use high index reflexes to abate the influence from the GaN background, e.g. the (004) reflex. Then the parameters which give the best fitting both in (004) and (002) reflexes are the proper structural parameters for the InGaN/GaN MQWs. In the Fig. 5.11 a) and b), both simulations of InGaN/GaN (004) and (002) linescans are well fitted with the measured curve in the peak position and intensity ratio between the peaks. Simulation results give a well thickness of 3.4nm with In content of 15% and a barrier of 14.9nm.

An alternative method to get rid of the influence from GaN background is to subtract the GaN peak from the measured curve.

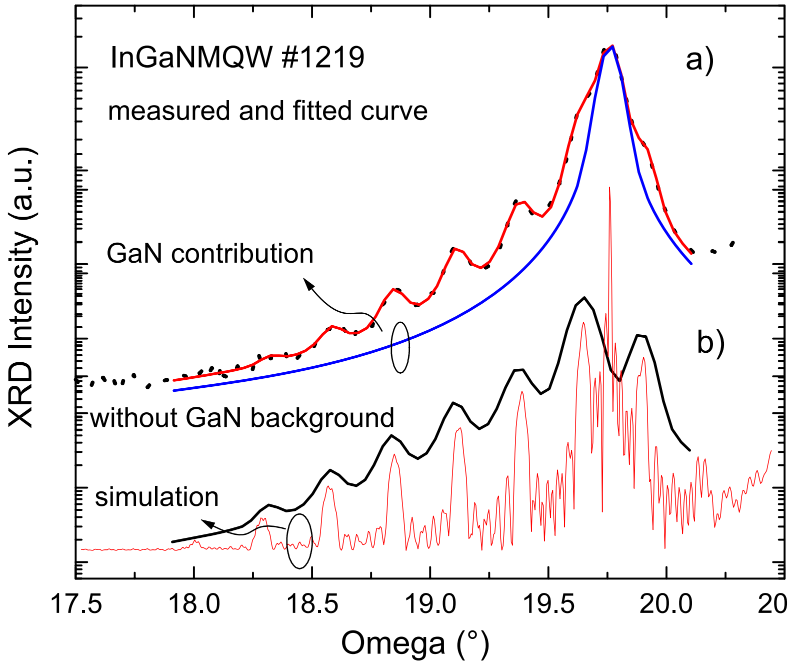

Figure 5.12 a) XRD patterns of InGaN/GaN MQWs#1219. The fitting curve by multiple pseudo-voigt function and the GaN contribution are shown b) the subtracted curve of mutiple pseudo-voigt fitting curve by the GaN contribution and the simulation.

Figure 5.12 a) plots the measured XRD pattern on one InGaN/GaN MQW sample with a perfect fitting curve by the multiple pseudo-voigt functions (red line).

Also shown in Fig.5.12 a) is the GaN contribution from this multiple pseud-Voigt functions fitting. Figure 5.12 b) shows the subtracted fitting curve by the GaN contribution. It means the “pure” superlattice peaks without the GaN background contribution. The simulation curve shown in Fig. 5.12 b) agrees well with the “pure” superlattice peaks both in intensity and the peak position. The slight contribution from the SiC substrate is another reason for the intensity difference between the simulation and subtracted curve if comparing the low order and high order superlattice peaks.

5.5.3 Photoluminescence of c-InGaN/GaN multiple quantum wells

The PL spectra from InGaN/GaN MQWs were performed at both room temperature and low temperature. Figure 5.13 and 5.14 shows 2K and room temperature PL spectra measured from samples MQW#1212 and MQW#1213 with different In mole fraction, the two samples grown with and without growth interruption. The PL spectra from InGaN/GaN MQWs sample #1212 with growth interruptions show a single emission peak of 2.65eV in the 2K PL spectrum and a 2.57eV peak in the 300K PL spectra. The difference of the emission energy is approximately 80meV, which is close to a typical blueshift (~ 70meV) in GaN PL emission peak at 2K and room temperature. This behaviour is closely correlating to that from the homogeneous layer. In contrast, the PL spectra (Fig. 5.14) from the InGaN/GaN MQWs sample #1213 without growth interruption show emission peak, which can be fitted by two Guassian peaks. In the 300K spectrum, one peak has emission energy of 2.58 eV and the other has emission energy of 2.45eV.

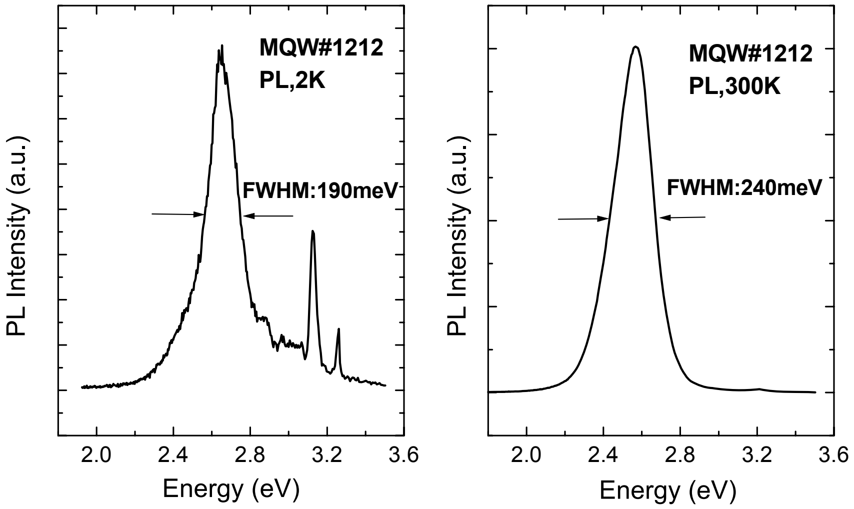

Figure 5.13 Room temperature and 2K PL spectra of $In_{0.12}Ga_{0.88}N$ MQW#1212

The peak with energy of 2.62 eV dominates the 2K PL spectrum with a weak shoulder at about 2.5eV, which is different with what is seen in the room temperature PL spectrum in which the low energy of 2.45eV is the stronger peak. The blue shift of dominant peak (170meV) between 2K and room temperature PL spectra is too large to be fulfilled only by a thermally induced blueshift.

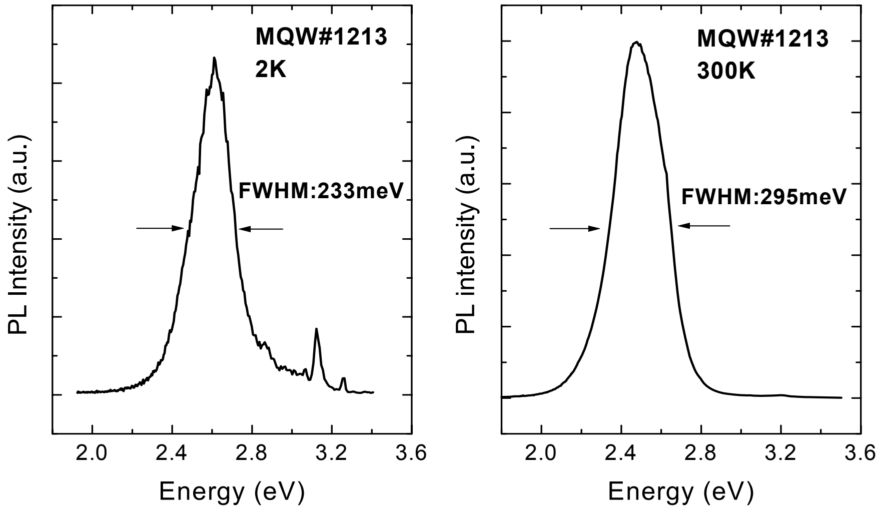

Figure 5.14 Room temperature and 2K PL spectra of $In_{0.13}Ga_{0.87}N$MQW#1213

These results coincide with the previous explanation that there are In rich phases or layers existing within the InGaN wells. At room temperature, the carriers have more opportunities to overcome the barrier of the In poor structures and jump into the In rich phases. Therefore, the high In content InGaN phases contribute more to the PL emission, which therefore yield higher red shift than that seen by only temperature induced variation at 300K. This conclusion is further corroborated by the deceasing in linewidth of the PL peak from the spectrum at 300K as compared to that at 2K. In sample #1212 with growth interruption, the FWHM of the emission peak decreased from 240meV at 300K to 190meV at 2K. This difference of 50 meV in the linewidth is close to the natural thermal broadening of 1.8kT (band to band transition), which is about 47meV [5]. However, in the PL spectra of InGaNMQW#1213 without growth interruption, the linewidth decreased from 295meV to 233meV, which is a difference of 62 meV. This is clearly larger than that of the thermal broadening energy. The different distribution of the carriers in these localized states at 2K and 300K may be the additional factor to the abnormally larger FWHM difference of the InGaN emission.

At 2K, since the thermal energy is too low to drive the carriers escaping from the localized state, the intensity distribution of the low and high energy peaks somehow reflects the volume of these two localized states in the InGaN. The dominant high energy 2.6eV emission peak may hint that the InGaN phase with 2.6eV emission has a higher volume than the InGaN phase with 2.45eV PL emission. The growth interruption helps to eliminate the InGaN phase with 2.45eV emission. This result is compatible with the conclusion drawn from the temperature dependent PL spectra on different In composition InGaN thick layer samples. It also indicates that the different In content InGaN phases also present in the InGaN/GaN MQWs structures are due to In segregation.

Figure 5.15 shows the PL spectra measured at 2K and 300K from another $In_xGa_{1-x}N$/GaN MQWs #1218 ($x = 0.16$). The well thickness is 3.7 nm and GaN barrier thickness is 11.4 nm.

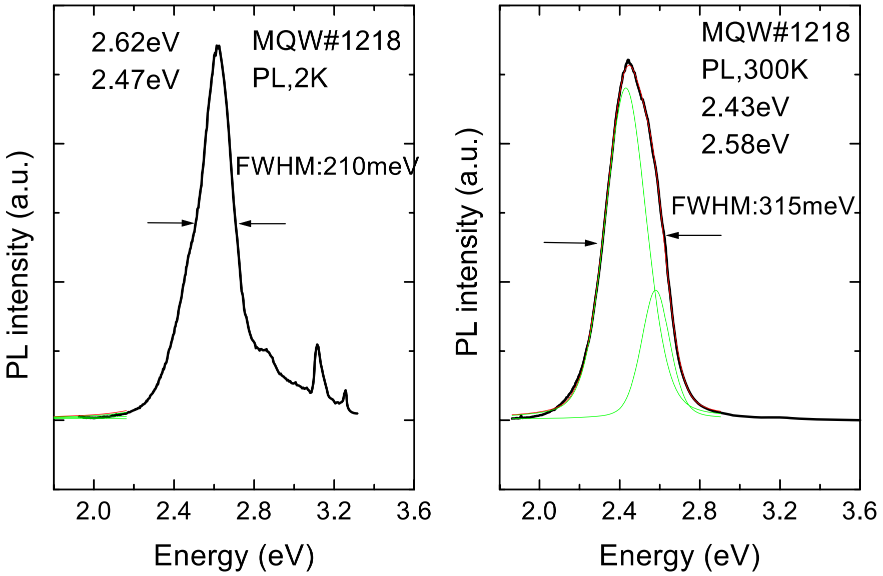

Figure 5.15 Room temperature and 2K PL spectra of $In_{0.13}Ga_{0.87}N$MQW1218

Two emission peaks are both present in the 2K and 300K spectra. The 2.43 eV and 2.58 eV peaks appear in the spectrum at 300K, and 2.47eV and 2.62eV peaks dominate the 2K PL spectrum. A blue shift of 40meV is found in all these two peaks measured at 300K and 2K. It is worthwhile to mention that the 2.62 eV dominates the 2K PL spectrum and 2.43eV peak dominates the 300K PL spectrum. The 2.47eV emission is quite pronounced in the 2K PL spectrum, which may be due to the higher In mole fraction. The large FWHM decrease of 105meV from 300K PL emission peak to that at 2K indicates that the In mole fraction distribution is the critical factor influencing the FWHM of the emission peak from this sample.

5.5.4 C-InGaN/GaN multiple quantum well with different well growth time

It has been discussed that during the deposition of InGaN quantum wells, the InGaN may have "pulling effect"[192,193], which means that the In mole fraction starts with low In concentration at the beginning and reach a constant level after some thickness of InGaN growth due to the impact of the strain [192]. The pulling effect yields indium poor and rich phases along the growth direction. It has been found in some MOCVD grown InGaN wells and layers. For testing this effect, a series of 6 folds InGaN/GaN MQWs have been grown with different well growth time under same growth parameters so that the samples correspond to the different growth stages of the InGaN.

The InGaN quantum well was grown at 610°C with growth interruption. The GaN barrier layer thickness was kept constant at 12nm in all samples. In mole fraction and well thickness versus the growth time are plotted in Fig 5.16. The In mole fraction is

16% in all the samples and the well thickness linearly increases with the growth time, yielding the growth rate of 0.83nm/min.

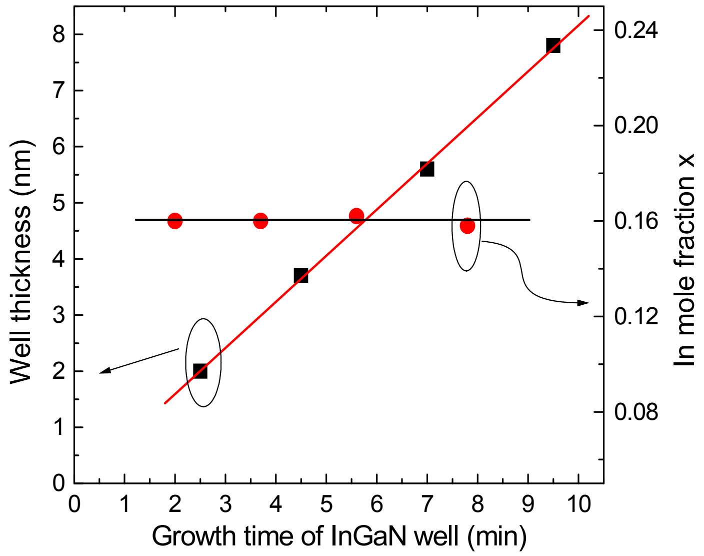

Figure 5.16 In mole fraction and thickness of the InGaN wells of InGaN/GaN MQWs sample with different growth time.

These results indicate evidently that unlike MOCVD grown InGaN wells, there is no In composition “pulling effect” existing in our MBE growth of InGaN/GaN MQWs. The room temperature PL emissions of samples with different thickness were measured and the peak energy versus the well thickness is plotted in Fig. 5.17.

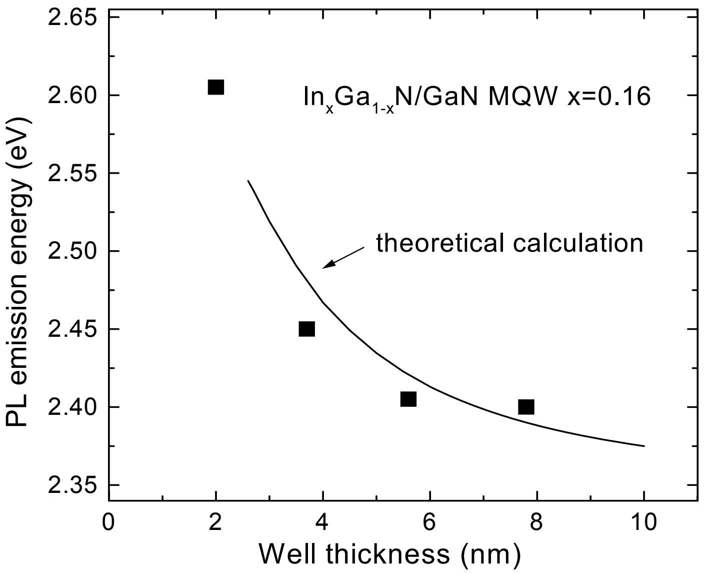

Figure 5.17 PL peak energy versus well thickness for a series of InGaN/GaN MQWs samples. The solid line is a theoretical fitting of the result.

The theoretical calculation of the blue shift due to the quantum size effect is also included in this figure (the solid line), showing a good agreement with the experimental data.

5.5.5 Comparison of single and multiple quantum wells

Multiple quantum wells enhance the light emission by the using more than one quantum well, which delivers high recombination efficiency. PL spectra from one InGaN single quantum well #1111 and another multiple quantum wells #1212 samples have been checked under the same PL setup and laser power. The #1212 MQWs sample has 12% In in the six folds of InGaN wells. For #1111SQW sample, the In concentration in the InGaN well is 7%. The well thickness is 3.5nm for MQWs sample and 4.5nm for the SQW sample. The In concentration difference may have an influence on the recombination of the carriers due to the strong confinement of the carriers in deep $In_{0.12}Ga_{0.88}N$ well.

Figure 5.18 shows the room temperature PL spectra from one InGaN/GaN SQW#1111 and another InGaN/GaN MQWs #1212. In the PL spectrum from InGaN/GaN MQW, the GaN emission is barely visible, whereas, the GaN emission peak from the InGaN SQW is rather strong.

The integrated intensity ratio of InGaN emission peak between the InGaN SQW and MQWs is 2.63, which demonstrates the enhanced light emission due to the multiple quantum well effects. However, this ratio is significantly smaller than the number of wells (6). This could be attributed to the carriers effective diffusion length being larger than the thickness of the barrier

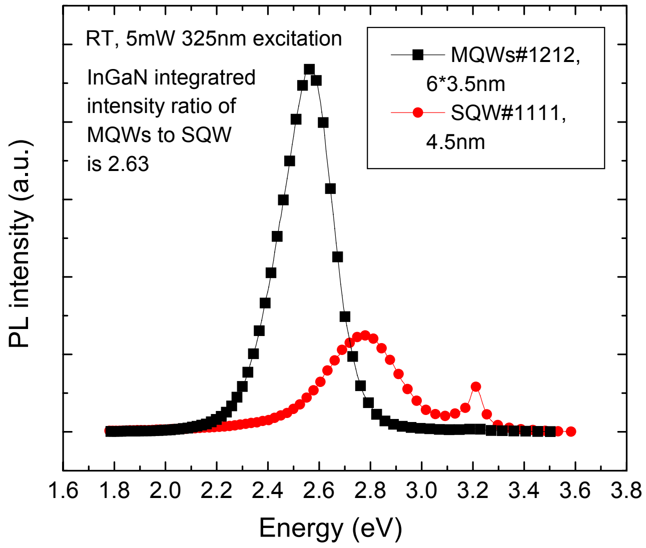

Figure 5.18 Room temperature PL spectra of $In_{0.07}Ga_{0.93}N$SQW#1111 and $In_{0.12}Ga_{0.88}N$MQW#1212

A rough estimation of the effective carriers diffusion length was performed. Assuming the same excitation efficiency for one laser photon in InGaN and GaN and the same recombination efficiency in 7% and 12% InGaN wells, if all the carriers generated in the effective diffusion length in the GaN can diffuse into the well and the carriers in the well can not diffuse out, then we have the following equation:

$$2.63*\left(2*L_d + L_{ws}\right) = \left(6*L_{wm} + 6*L_{mb} + L_d\right) \tag{5.8}$$

where L_d is the diffusion length, L_{ws} is the well thickness of the SQW, L_{wm} and L_{mb} denote the well and barrier thickness respectively. For multiple quantum well #1212 the barrier thickness is 10.5nm, which gives a diffusion length of about 17nm as calculated from equation 5.8. This value is comparable to the data in the c-AlGaN/GaN MQW [194].

5.6 Applications of c-InGaN/GaN multiple quantum wells in a resonant cavity structure

5.6.1 Resonant cavity light emitting diodes

In 1992, Schubert et al[195] proposed a new device structure, called a resonant cavity light emitting diode (RCLED), in which the active region is placed into a resonant optical cavity. The cavity is defined by a highly reflective, e.g. a distributed Bragg reflector (DBR) with high reflectivity R_1 and a moderately reflective R_2 mirror (DBR or metal mirror). The optical properties of the RCLED are superior, while the fabrication process complexity is comparable to conventional LEDs. A nitride based RCLED structure is depicted in Fig.5.19.

The placement of the active region in resonant cavity results in several clear advantages of the RCLED over conventional LEDs', which are outlined as follows:

Firstly, it is well-known that the probability for spontaneous emission is proportional to the matrix element of the initial and final electron state and proportional to the optical mode density. The optical mode density in a Fabry-Perot resonator is strongly enhanced for on-resonance wavelengths. As a consequence, on-resonance transitions of the RCLEDs are enhanced. It has been demonstrated experimentally that the spontaneous lifetime of a medium changes drastically, upon placement of the medium in a optical cavity [196,197]. Changes in spontaneous emission lifetime exceeding a factor of 10 for high-finesse optical cavities have been reported. The carrier lifetime change is due to the varying optical mode density in a Fabry-Perot cavity. While off-resonance optical transitions have a longer lifetime, on-resonance transitions have a shorter lifetime. Spontaneous emission of the RCLED is, therefore, “channeled” into the optical resonance modes of the cavity, which delivers enhanced spontaneous emission in the resonance mode.

Second, emission of light through the contact side (“top side”) is enhanced due to the highly reflective mirror adjacent to the n-type confinement layer (“bottom side”). Light emission in conventional LEDs is typically close to isotropic. However, in the RCLED structure, the bottom reflector has a higher reflectivity than the top reflector, i.e., R1>R2. As a consequence, light propagating along the optical axis of the cavity exits the cavity predominantly through the top (low reflectivity) mirror. The anisotropic emission spectrum of the RCLED can enhance the emission through the topside by a factor of two.

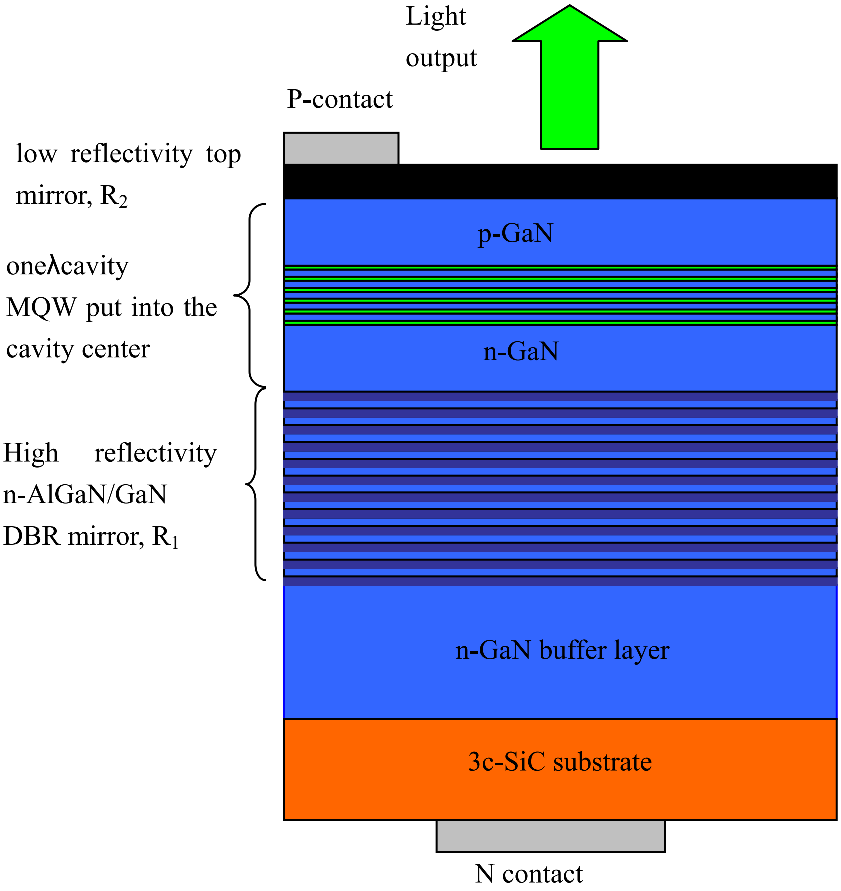
Light output
P-contact
low reflectivity top mirror, R2
oneλcavity MQW put into the cavity center
High reflectivity n-AlGaN/GaN DBR mirror, R1
p-GaN
n-GaN
n-GaN buffer layer
3c-SiC substrate
N contact

Figure 5.19 Schematic layer sequence of nitride based RCLED

Thirdly, the improved spectral purity of the RCLED makes the device well suited for optical communication purposes. Conventional LEDs have spectra linewidths determined by the density of states in the conduction and valence band and the thermal energy of carriers. Typical linewidths are on the order of 1.8 kT, where kT is the thermal energy. A better spectral purity can be achieved with the RCLED. Since the spontaneous emission from the active region is constrained to emit into the modes of the optical cavity, the finesse of the cavity allows one to estimate the linewidth of the RCLED. The cavity Q of a co-planar Fabry-Perot cavity is given by [5]:

$$Q = \frac{\nu}{\Delta\nu} = 2\pi \frac{\bar{n} L_c}{\lambda} * \left(\frac{\sqrt[4]{R_1 R_2}}{1-\sqrt{R_1 R_2}}\right) \tag{5.9}$$

where L_c is the cavity length, and Δν and ν are the bandwidth and frequency of the Fabry-Perot resonance mode, respectively. As an example, for GaAs, we choose $L_c = \lambda$, hν = 1.42 eV, and $R_1R_2 = 0.9$, which yields Q ≈ 120. The corresponding linewidth is hΔν ≈ 12 meV, which is much narrower than kT at room temperature. Due to the inherently high spectral purity of the RCLED, the device is expected to have less chromatic dispersion in silica fibers.

Note that the resonant cavity light-emitting diode is structurally related to vertical cavity surface-emitting lasers (VCSEL) with semitransparent/semireflective top contacts. However, the two device structures serve different purposes and have different design characteristics. For example, mirror reflectivities exceeding 99% are essential for low threshold operation of the lasers. For the RCLED, a top mirror reflectivity of 90% is sufficient, i.e., the requirements for the two mirrors are less stringent for the RCLED. Unlike the VCSEL, the RCLED has no threshold current to get lasing light. Both make the RCLED fabrication much easier than VCSEL. Furthermore, due to the relative broader emission spectrum of RCLED, the temperature induced emission wavelength variation is relatively small. Those advantages show RCLED as a suitable light source for communication application.

Plastic optical fibres (POF), e.g. PMMA step-index POF for local area networks application have a minimum attenuation at the wavelength of 510nm. Thus a green (510nm) emission RCLED is demanded for the light source for this application. The most promising materials for green RCLED are III-nitrides, where by varying the composition of InGaN, 510nm emission can be obtained. Naranjo et al demonstrated the feasibility of green RCLED based on hexagonal III-nitride[198].

Here we report the results from the components of cubic nitride based resonant cavity structure, i.e. c-AlGaN/GaN Bragg mirrors and a resonant cavity structures.

5.6.2 Cubic AlGaN/GaN distributed Bragg reflectors

Bragg mirror is a repeated structure, which contains two layers with different refractive indices. With the thickness of $\lambda_b/4$ of each layer, the high reflectivity with stop band center at λ_b can be obtained. Three parameters are critical for achieving high reflectivity:

1) The refractive indices contrast. Higher refractive index difference leads to higher reflectivity of the DBR mirror.
2) Number of the repeated stacks. More stacks of repeated structures lead to higher reflectivity.
3) The boundary condition. To get stop band with maximum reflectivity, the DBR mirror should end with high refractive index layer. In the AlGaN/GaN DBR, the end layer should be GaN layer. Beside these points, the interface quality also has impact on the DBR reflectivity.

In green light source application in POF based networks, the RCLED needs AlGaN/GaN DBR with stop band centre of 510nm. Due to small refractive index contrast between AlGaN and GaN at 510nm (e.g. 0.1 for $Al_xGa_{1-x}N$/GaN DBR, $x = 0.33$), high reflectivity AlGaN/GaN DBR needs more number of stacks or higher Al content, which tends to deliver cracks in the DBR structures[199].

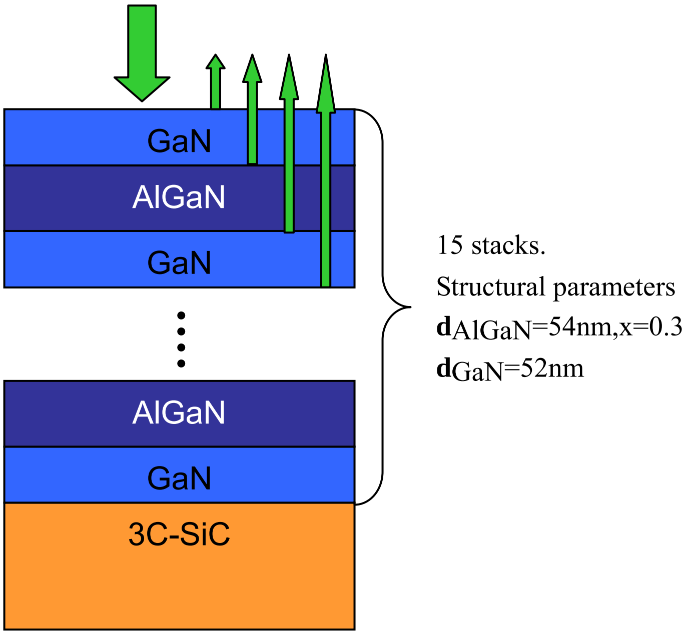
GaN
AlGaN
GaN
AlGaN
GaN
3C-SiC
15 stacks.
Structural parameters
dAlGaN=54nm,x=0.3
dGaN=52nm

Figure 5.20 Schematic drawing of cubic AlGaN/GaN DBR

DBR consisting of 15.5 stacks c-AlGaN/GaN has been directly grown on 3C-SiC (structure shown in Fig.5.20). No cracks were found from this DBR under SEM. Reciprocal space maps of the (-1-13) reflex revealed that the AlGaN layers were fully strained on GaN and the Al molar ratio is 0.31.

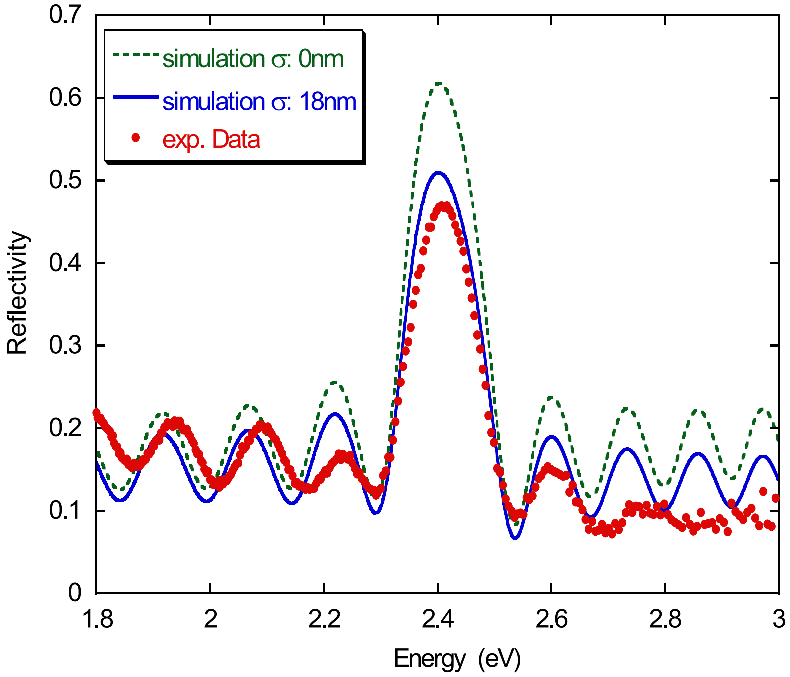

Figure 5.21 Reflectivity measurement on the 15folds c-AlGaN/GaN DBR result and the transfer matrix model simulation results

The reflectivity of this DBR structure is shown in Fig. 5.21. The maximum reflectivity of the DBR was 0.48 at the center of the stop band at 2.41eV. The transfer matrix model was used to calculate the reflectivity of our DBRs. The surface roughness influence is also considered by the equation [200].

$$R_s = R_0 * \exp\left(-\left(4\pi\sigma n/\lambda\right)^2\right) \tag{5.10}$$

R_O is the reflectivity with perfect interface. The symbol n denotes the refractive index of the incident medium. The σ denotes interface root-mean-square fluctuation from the average interface, which was measured by AFM.

Including interface roughness scattering, the simulated curve showed a good agreement with the measured data yielding the thickness of the AlGaN and GaN layers (55nm and the 52.7nm).

5.6.3 Combined structure of c-InGaN/GaN multiple quantum wells and c-AlGaN/GaN distributed Bragg reflectors

A test resonant cavity structure was grown to investigate the optical properties of the resonant cavity. Figure 5.22 shows the schematic drawing of this structure.

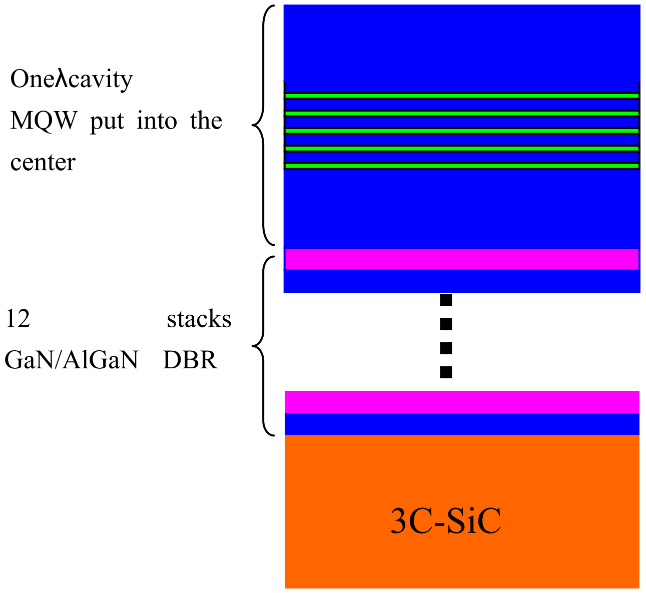

Figure 5.22 The resonant cavity structure without top mirror

A λ cavity structure without top mirror was grown on 12 stacks of c-AlGaN/GaN DBR, in which 6 folds InGaN/GaN MQWs were put into the center of λ cavity. Thickness of the resonant cavity is designed with the Bragg wavelength of λ_b = 510nm. For this resonant cavity structure, the room temperature PL spectra were measured with different angles and shown in Fig. 5.23. The solid curve was taken in the standard PL configuration, i.e. the detection direction perpendicular to the sample surface. An enhanced light emission was obtained at 526nm. When the sample was rotated for 35°, the enhanced light had blue shifted to 510nm.

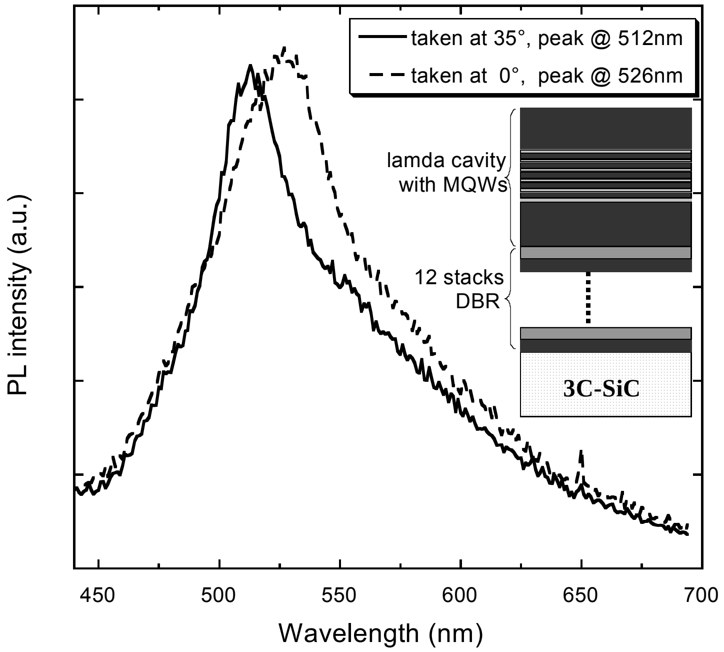

Figure 5.23 Angular dependent room temperature PL spectra of resonant cavity structure #1251. a) along the normal direction, b) along the 35° to the normal direction

This blueshift is supposed to come from the cavity effect, which is explained as following:

The air/GaN interface can be treated as a low reflectivity mirror. The DBR and the top air/GaN "mirror" formed a resonant cavity (shown in Fig. 5.24). The wavevector along the vertical direction, $k_\perp$ was selected by the cavity resonance and kept constant. If the sample is rotated from 0 ° to a non-zero angle, the horizontal component of the wavevector, $k_{//}$ is increased, yielding a larger wavevector k, i.e. a higher energy.

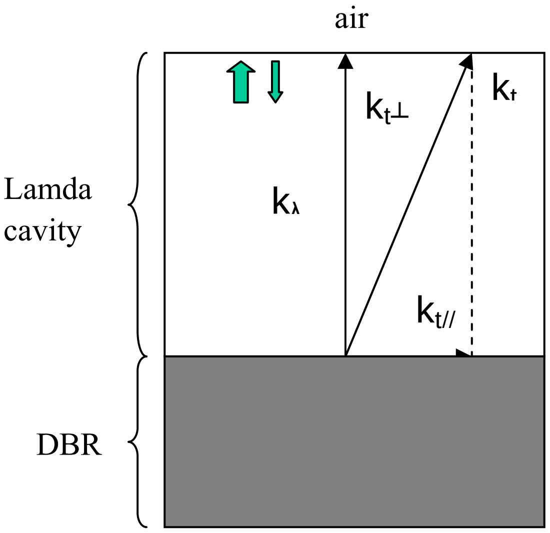

Figure 5.24 Schematic drawing of the angular dependent PL measurement.

Transfer matrix model simulation on the reflectivity from 0° and 35° to the normal direction show the blue shift of the cavity mode is 65meV, which is the same with the value shown in the PL measurement at 0 and 35°.

This structure may be considered as a first building block of a green RCLED based on cubic III-nitrides.

6. Conclusion

In this thesis, I have introduced my work on cubic III-nitrides growth and characterization, mainly on the results of cubic InGaN and c-InGaN/GaN quantum wells structures. It has been proven in the early work of our group that cubic GaN can be successfully grown on GaAs and 3C-SiC substrates by a careful control of the surface stoichiometry. Due to increased c-GaN quality by using 3C-SiC substrates with less lattice mismatch, the structural and optical qualities of c-InGaN grown on these c-GaN layers have also been improved. This helped us to have an in-depth understanding of the growth and characterization of cubic InGaN. Beside the short description on c-GaN growth in this thesis, the focus has been on growth and characterization of c-InGaN layers and on c-InGaN/GaN quantum well growth and properties. Main achievements of this work are summarized in the following:

Firstly, for c-GaN growth, the surface reconstruction of cubic GaN is a guide for adjusting the Ga flux ensuring the metal rich growth of c-GaN, which is necessary for achieving high quality c-GaN. Through plotting the surface reconstruction diagram, a relation of the Ga flux for stoichiometric growth of c-GaN versus growth temperature at constant N flux is achieved. The cubic GaN grown on 3C-SiC substrates has superior quality as compared to c-GaN on GaAs substrates due to less lattice mismatch between 3C-SiC and c-GaN. For 600nm c-GaN layers on 3C-SiC and GaAs, the FWHM of the X-ray rocking curve of the c-GaN layer grown on 3C-SiC substrate is 22 arcmin, which is approximately half of that from the c-GaN layer on a GaAs substrate (about 44 arcmin). The line width of the GaN PL emission peak at 300K also decreases from 78meV for c-GaN on GaAs to 66meV for c-GaN on 3C-SiC substrate. Thick cubic GaN layers have been grown on MBE c-GaN buffer layers by MOCVD. The thick MOCVD GaN layer has a dramatic decrease of XRD rocking curve FWHM compared to that of a MBE c-GaN buffer layer. This thick MOCVD c-GaN layer can be used as substrates for further MBE III-nitride growth.

The focus of this thesis has been on the achievement of high quality InGaN growth and the investigation of the structural and optical properties of c-InGaN. Special phenomena related to InGaN have been discussed: Alloy order-disorder, phase separation, In segregation, polarization fields, Stokes shift, and InGaN bandgap bowing. These phenomena have made it difficult to achieve high quality InGaN growth and also to understand the properties of InGaN. The impact of In and Ga fluxes on InGaN growth has been carefully investigated. The impinging In atoms onto the InGaN surface principally have three reaction pathways: they may incorporate into the InGaN layer, evaporate from the InGaN surface, or form into In droplets. With increasing In flux, the In mole fraction in the InGaN layer increases at low In flux range. At a certain In flux, the In mole fraction saturates and stays constant if the In flux increases further. Simultaneously, the density and the size of In droplets increases as the In flux increase, which is revealed by SEM and the indium Bragg peak in the XRD pattern. The growth interruption helps to evaporate the excess In on the surface. It is shown by AFM measurement that the surface roughness decreases with increasing In flux, indicating that the In works not only to incorporate as InGaN, but also creates a surfactant effect. In PL spectra, low In flux, i.e. N rich growth leads to a weak emission peak which has a large blueshift in the peak energy compared to the strong emission peak from c-InGaN samples grown under In rich condition. This demonstrates the repression effect of In segregation by N rich growth. In the InGaN samples with different Ga flux, the In mole fraction linearly increases with decreasing Ga flux. The extrapolation point at $x = 0$ shows that the total incorporated metal flux, or the InGaN growth rate, is about 60% of the GaN growth at 720°C with the same N source parameters. This phenomenon was also found in other c-InGaN samples. A model has been proposed to explain this growth rate reduction. In this model, the In floating layer on the InGaN surface due to excess In and the segregation effects prevents the In incorporation and reduce the effective N flux, i.e. the c-InGaN growth rate. Based on this model, a formula for c-InGaN growth is suggested which has proven to be feasible.

The structural and optical properties of c-InGaN have also been measured. The XRD reciprocal space map shows that InGaN layers are pseudomorphically or partially relaxed on GaN buffer layers and the In mole fraction ranges from 0 to 0.2. The TEM picture revealed that there are some column or slab-like structures along the growth direction, probably indicating the existence of the In rich phases in the c-InGaN layers. PLE measurements reveal that the InGaN emissions come from the localized structures, which have an effective gap of about 300meV lower than band gap of the “bulk” c-InGaN. The band gap of c-$In_xGa_{1-x}N$ with different x has been measured by PLE and ellipsometry and plotted with x. A small bowing parameter of only $b = 0.6$eV is obtained. Temperature dependent PL measurements revealed that there are two preferential peaks, which are located at 2.4eV and 2.6eV in the room temperature PL spectra of $In_xGa_{1-x}N$ with $0<x<0.18$. The intensity ratio of the 2.4eV peak to the 2.6eV peak increases with the In mole fraction for different samples and it also increases with the measurement temperature in the PL spectra measured at 2K-300K for c-$In_xGa_{1-x}N$ samples with $x =0.06$ and $x = 0.13$, respectively. Localized properties of both emissions were proven by the “S” shape behaviour of the PL peak energy dependence on the temperature. Depth resolved CL spectra demonstrated a thin layer with higher In content than the “bulk”, locating close to the surface of a c-InGaN layer grown on GaAs substrate. The stability of c-InGaN layers was tested by thermal annealing experiments, which suggested that the spinodal phase decomposition may not exist in these c-InGaN samples.

Cubic InGaN/GaN quantum wells have been grown and the optical and structural properties of our c-InGaN/GaN multi-quantum wells (MQWs) have been studied. The integrated PL intensity increases with the single quantum well thickness, evidently proving that the polarization field is absent in cubic III-nitrides. Growth interruptions between the c-InGaN quantum well and the barrier help to evaporate the surface excess In atoms or droplets. Two methods have been discussed on the dynamic simulation of the XRD pattern to get the accurate structural parameters of the MQWs, avoiding the influence from the broad GaN background. Room temperature and low temperature (2K) PL measurements on c-InGaN/GaN MQWs reveal the localized properties of the PL emission from the MQWs. The analysis of the c-InGaN/GaN MQWs samples with different well growth time but identical growth parameters demonstrated that the In composition “pulling effect” may not occur in these MBE grown c-InGaN/GaN MQWs. Finally, c-InGaN/GaN MQWs with green light emission was applied to a resonant cavity structure. The cavity effect was demonstrated in this structure by angular dependent PL measurements.

Bibliography

1 S. Nakamura and G. Fasol, *The Blue Laser Diode*. (Springer, Berlin, 1997).

2 Y. F. Zhang and J. Singh, J. Appl. Phys. **85**, 587 (1999).

3 A. G. Bhuiyan, A. Hashimoto, and A. Yamamoto, J. Appl. Phys. **94**, 2779 (2003).

4 J. Edmond, A. Abare, M. Bergman et al., J.Cryst.Growth **272**, 242 (2004).

5 E. F. Schubert, *Light-emitting diodes*. (Cambridge University Press, 2003).

6 S. R. Kurtz, A. A. Allerman, D. D. Koleske et al., J.Appl.Phys. **95**, 1888 (2004).

7 J. S. Lee, D. M. Liu, H. Kim et al., Appl.Phys.Lett **85**, 2631 (2004).

8 H. Morkoc, A. Di Carlo, and R. Cingolani, Solid State Electronics **46**, 157 (2002).

9 T.M. Kuan, S.J. Chang, Y.K. Su et al., J.Cryst.Growth **272**, 300 (2004).

10 W. C. Johnson, J. B. Parsons, and M. C. Crew, J. Phys. Chem. B **36**, 2561 (1932).

11 H. P. Maruska and J. J. Tietjen, Appl. Phys. Lett. **15**, 327 (1969).

12 J. I. Pankove, E. A. Miller, D. Richman et al., Journal of Luminescence **4**, 63 (1971).

13 H. Amano, N. Sawaki, I. Akasaki et al., Appl.Phys.Lett **48**, 353 (1986).

14 S. Nakamura, Jpn J. Appl.Phys. **30**, L1705 (1991).

15 H. Amano, M. Kito, K. Hiramatsu et al., Jpn. J. Appl. Phys. **28**, L2112 (1989).

16 I. Akasaki, H. Amano, M. Kito et al., J. Lumin. **48/49**, 666 (1991).

17 S. Nakamura, T. Mukai, M. Senoh et al., Jpn J. Appl.Phys. **31**, L139 (1992).

18 S. Nakamura, M. Senoh, N. Iwasa et al., Jpn. J. Appl. Phys. **34**, L797 (1995).

19 A. Bhattacharyya, W. Li, J. Cabalu et al., Appl.Phys.Lett **85**, 4956 (2004).

20 S. Nakamura, M. Senoh, and T. Mukai, Jpn. J. Appl. Phys. **30** (10A), L1708 (1991).

21 S. Nakamura, M. Senoh, S. Nagahama et al., Appl. Phys. Lett. **69**, 1477 (1996).

22 S. Nakamura, M. Senoh, S. Nagahama et al., Appl. Phys. Lett. **70**, 1417 (1997).

23 S. Nakamura, M. Senoh, S. Nagahama et al., Post deadline Papers of IEEE Lasers and Electro-Optics Society **PD1.1** (1997).

24 S. Nakamura, M. Senoh, S. Nagahama et al., MRS Internet J. Nitride Semicond. Res **4S1**, G 1.1 (1999).

25 G. Fasol, Science **278**, 1902 (1997).

26 S. F. Chichibu, T. Onuma, T. Aoyama et al., J.Vac.Sci.Technol. B **21**, 1856 (2003).

27 P. Das and D.K. Ferry, Sol. State Electron. **19**, 851 (1976).

28 M. Fanciulli, T. Lei, and T.D. Moustakas, Phys. Rev. B **48**, 15144 (1993).

29 T. Lei, T.D. Moustakas, R.J. Graham et al., J. Appl. Phys. **71**, 4933 (1992).

30 T. P. Chow and Ghezzo., presented at the Material Research Society Symposium Proceedings, Pittsburgh, PA., 1996 (unpublished).

31 V. Bougrov, M.E. Levinshtein, S.L. Rumyantsev et al., *Properties of Advanced SemiconductorMaterials GaN, AlN, InN, BN, SiC, SiGe*. (John Wiley & Sons, Inc, New York, 2001).

32 M. E. Levinshtein, S. L. Rumyantsev, and M. S. Shur, *Properties of Advanced Semiconductor Materials: GaN, AlN, InN, BN, SiC, and SiGe*. (John Wiley and Sons, New York, 2001).

33 I. Vurgaftman, J. R. Meyer, and L. R.Ram-Mohan, Journal of Applied Physics **89**, 5815 (2001).

34 T. Lei, T.D. Moustakas, R.J. Graham et al., J. Appl. Phys. **71** (10), 4933 (1992).

35 E. Ejder, Phys. Status Solidi (a) **6**, 445 (1971).

36 M. Leszczynski, H. Teisseyre, T. Suski et al., Appl.Phys.Lett **59** (1), 73 (1996).

37 Z.-J. Tian, M. W. C. Dharma-Wardana, and L. J. Lewis, Mat. Res. Soc. Symp. Proc. **395**, 473 (1996).

38 W.Qian, M.Skowronski, and G.R.Rohrer, in *III-Nitride, SiC, and Diamond Materials for Electronic Devices. Material Research Society Symposium Proceedings*, edited by R.J. Nemanich (Pittsburgh, PA, 1996), Vol. 423, pp. 475.

39 M. Fuchs, J. L. F. Da Silva, C. Stampfl et al., Phys. Rev. B **65**, 245212 (2002).

40 D. Schikora, M. Hankeln, D.J. As et al., Phys. Rev. B **54** (12), R8381 (1996).

41 H. Okumura, K. Ohta, G. Feuillet et al., J. Crystal Growth **178**, 113 (1997).

42 D.J. As, A. Richter, J. Busch et al., Appl. Phys. Lett. **76** (1), 13 (2000).

43 H. Yang, L.H. Zheng, J.B. Li et al., Appl. Phys. Lett. **74** (17), 2498 (1999).

44 T. Kitamura, S.H. Cho, Y. Ishida et al., J. Cryst. Growth **227-228**, 471 (2001).

45 D.J. As, T. Frey, D. Schikora et al., Appl. Phys. Lett. **76** (13), 1686 (2000).

46 A. Dadgar, A. Strittmatter, J. Bläsing et al., phys.stat.sol. **0** (6), 1583 (2003).

47 O. Brandt, Y. J. Sun, H. P. Schönherr et al., Appl.Phys.Lett. **83**, 90 (2003).

48 D.J. As, R. Richter, J. Busch et al., MRS Internet J. Nitride Semicond. Res. **5S1**, W3.81 (2000).

49 S. Nakamura, M. Senoh, S. Nagahama et al., Appl. Phys. Lett. **69**, 4056 (1996).

50 M. A. Hermann and H. Sitter, *Moelcular Beam Epitaxy*. (Springer Verlag, Berlin, 1989).

51 T. Frey, PhD thesis, University of Paderborn (2000).

52 A.Schmidegg, University of Linz, 2004.

53 J. Pankove, *optical processes in semiconductors*. (Dover publication, Inc., New York, 1975).

54 C. R. Wang, University of Paderborn, 1999.

55 K. Kanaya and S. Okayama, J. Phys. D **5**, 43 (1972).

56 H. Amano, N. Sawaki, I. Akasaki et al., Appl. Phys. Lett. **48** (5), 353 (1986).

57 M. E. Lin, B. Sverdlov, G. L. Zhou et al., Applied Physics Letters **62**, 3479.

58 D. J. Smitha, D. Chandrasekhar, B. Sverdlov et al., Appl.Phys.Lett **67**, 1830 (1995).

[59] T. Shibata, H. Sone, K. Yahashi et al., J.Cryst.Growth **189-190**, 67 (1998).

[60] H. Yang, S. Zhang, D. Xu et al., Jpn. J. Appl. Phys. **to be published** (2001).

[61] K.Matsubara and T.Takagi, Jpn. J. Appl. Phys. **22**, 511 (1982).

[62] R. PASZKIEWICZ, B. PASZKIEWICZ, R. KORBUTOWICZ et al., Cryst. Res. Technol. **36**, 971 (2001).

[63] H. Lu, W. J. Schaff, L. F. Eastman et al., Appl.Phys.Lett **83**, 1136 (2003).

[64] N N Zinov'ev, A V Andrianov, B Y Averbukh et al., Semicond. Sci. Techn. **10**, 1117 (1995).

[65] R. C. Powell, G. A. Tomasch, Y.-W. Kim et al., Materials Research Society Symposium Proceedings **162**, 525 (1990).

[66] S. Nakamura, M. Senoh, S. Nagahama et al., Appl.Phys.Lett **68**, 2105 (1996).

[67] S.K. Duan, X.G.Teng, Y.T. Wang et al., J.Cryst.Growth **189-190**, 197 (1998).

[68] B. Schöttker, University of Paderborn, 1999.

[69] L.M. Belyaev, *Rubby and Sapphire*. (Amerind Publishing Co., New Dehli, 1980).

[70] E.L. Kern, D.W. Hamil, H.W. Deam et al., presented at the Mater. Res. Bull., Special Issue, Pennsylvania, USA,, 1968 (unpublished).

[71] B.Yang, A.Trampert, B. Jenichen et al., Appl.Phys.Lett **73**, 3869 (1998).

[72] W. Qian, M. Skowronski, and G.R. Rohrer, presented at the Material Research Society Symposium Proceedings, Pittsburgh, PA, 1996 (unpublished).

[73] M. Kamp, C. Kirchner, V. Schwegler et al., MRS Internet J. Nitride Semicond. Res. **4S1**, G10.2 (1999).

[74] Y. Okada and Y. Tokumaru, J. Appl. Phys. **56** (2), 314 (1984).

[75] P. R. Hageman, S. Haffouz, V. Kirilyuk et al., phys.stat.sol.(a) **188** (2), 523–526 (2001).

[76] S. A. Nikishin, N. N. Faleev, V. G. Antipov et al., Appl. Phys. Lett. **75**, 2073 (1999).

[77] *Semiconductor and Semimetals*. (Academic Press, N.Y., 1975).

[78] U. Köhler, Paderborn University, 2003.

[79] H. Yang, S.M. Zhang, D.P. Xu et al., IPAP Conf. Ser. **1**, 64 (2001).

[80] H. Okumura, H. Hamaguchi, T. Koizumi et al., J. Crystal Growth **189/190**, 390 (1998).

[81] E. Martinez-Guerrero, E. Bellet-Amalric, L. Martinet et al., J. Appl. Phys. **91**, 4983 (2002).

[82] V. Holy, U. Pietsch, and T. Baumbach, *High resolution X-ray scattering from thin films and multilayers*. (Springer-Verlag, New York, 1999).

[83] D. J. As, in *Optoelectronic properties of semiconductors and superlattices*, edited by L.T. Ferguson (Taylor & Francis Books, New York, 2003), Vol. 19.

[84] A. Montaigne Ramil, K. Schidegg, A. Bonanni et al., Thin Solid Films **455**, 684 (2004).

[85] S. Nakamura, in *GaN and related materials*, edited by S.J. Pearton (Gordon and Breach Science Publishers, Amsterdam, 1997), Vol. 2, pp. 471; S. Nakamura, in *Group III nitride semiconductor compounds - physics and applications*, edited by B. Gil (Clarendon Press, Oxford, 1998), Vol. 6, pp. 391.

86 T. Frey, University of Paderborn, 2000.
87 D. Storm, J. Appl. Phys. **89**, 2452 (2001).
88 H. Chen, A. R. Smith, R. M. Feenstra et al., MRS internet J. nitride semicond. Res. **4s1,**, G9. 5 (1999).
89 O. Brandt, P. Waltereit, U. Jahn et al., Phys. Stat. Sol (a) **192**, 5 (2002).
90 J. Wu, W. Walukiewicz, K. M. Yu et al., Appl.Phys.Lett **80**, 4741 (2002).
91 T. V.Shubina, S. VIvanov, V. N.Jmerik et al., Phys. Rev. Lett. **92**, 117407 (2004).
92 F. Bechstedt, J. Furthmüller, M. Ferhat et al., phys.stat.sol. (a) **195** (3), 628 (2003).
93 W.R. Lambrecht and B. Segall, Phys. Rev. B **47**, 9289 (1993).
94 C.P. Foley and T.L. Tansley, Phys. Rev. B **33**, 1430 (1986).
95 S.K. Pugh, D.J. Dugdale, S. Brand et al., Semicond. Sci. Techn. **14**, 23 (1999).
96 S.Strite, Bull.Am.Phys.Soc **37**, 346 (1992).
97 F. Bernardini, V. Fiorentini, and D. Vanderbil, Phys. Rev. B **56**, R10024 (1997).
98 C. Adelmann, R. Langer, G. Feuillet et al., Appl. Phys. Lett. **75** (22), 3518 (1999).
99 J. W. Matthews and A. Blakeslee, J. Cryst. Growth **27**, 118 (1974).
100 R. People and J. C. Bean, Appl.Phys.Lett **47**, 322 (1985).
101 M. Marques, L. K. Teles, L. M. R. Scolfaro et al., Appl.Phys.Lett **83**, 890 (2003).
102 G.B. Stringfellow, J.Cryst.Growth **58**, 194 (1982).
103 A.Zunger and S.Mahajan, in *Handbook on semiconductors*, edited by S. Mahajan (North-Holland, Amsterdam, 1994), Vol. 3.
104 G.P. Srivastava, J.L. Martins, and A.Zunger, Phys. Rev. B **31**, 2561 (1985).
105 D. Doppalapudi, N. Basu, K. F. Ludwig Jr et al., J. Appl. Phys. **84**, 1389 (1998).
106 D. Korakakis, Jr. K. F. Ludwig, and T. D. Moustakas, Appl.Phys.Lett **71**, 72 (1997).
107 T.S. Kuan, T.F. Kuech, W.I. Wang et al., Phys. Rev.Lett. **54**, 201 (1985).
108 D. Korakakis, K. F. Ludwig, Jr et al., Appl.Phys.Lett **71** (1), 72 (1997).
109 P. Ruterana, G. Nouet, W. Van der Stricht et al., Appl.Phys.Lett **72**, 1742 (1998).
110 L.K. Teles, L.G. Ferreira, J.R. Leite et al., Appl. Phys. Lett. **82** (24), 4274 (2003).
111 I. Ho and G.B. Stringfellow, Appl. Phys. Lett. **69** (18), 2701 (1996).
112 L.T. Romano, M.D. McCluskey, B.S. Krusor et al., J.Cryst.Growth **189/190**, 33 (1998).
113 N.A. El-Masry, E.L. Piner, S.X. Liu et al., Appl. Phys. Lett. **72**, 40 (1998).
114 S.M. Bedair, in *Semiconductors and Semimetals*, edited by T.D. Moustakas (Academic Press, San Diego, 1998), Vol. 50.
115 J. Bai, T. Wang, and S. Sakai, J. Appl. Phys. **88** (8), 4729 (2000).
116 M. B. Nardelli, K. Rapcewicz, and J. Bernholc, Appl. Phys Lett. **71** (21), 3135

(1997).

117 K. Lischka, phys. stat. sol. (a) **177**, 135 (2000).

118 K.P. O'Donnell, I. Fernandez-Torrente, P.R. Edwards et al., J.Cryst.Growth **269**, 100 (2004).

119 M. Yoshimoto, H. Yamamoto, W. Huang et al., Appl.Phys.Lett **83** (17), 3480 (2003).

120 Ashraful Ghani Bhuiyan, Kenichi Sugita, Ken Kasashima et al., Appl.Phys.Lett **83**, 4788 (2003).

121 J. Wu and W. Walukiewicz, Superlattices and Microstructures **34**, 63 (2003).

122 T. Matsuoka, H. Okamoto, M. Nakao et al., Appl.Phys.Lett **81** (7), 1246 (2002).

123 T.V. Shubina, S.V. Ivanov, V. N. Jmerik et al., Phys. Rev. Lett. **92**, 117407 (2004).

124 Moustakas and Jacques T.D., in *Gallium Nitride (GaN) I* (Academic Press, San Diego, 1998), Vol. 50, pp. 127.

125 S.F. Chichibu, M. Sugiyama, T. Kuroda et al., Appl. Phys Lett. **79** (22), 3600 (2001).

126 I. Akosaki, S. Sota, H. Sakai et al., Electron. Lett. **32**, 1105 (1996).

127 K.P. O'Donnell, R.W. Martin, and P.G. Middleton, Phys. Rev. Lett. **82** (1), 237 (1999).

128 O. Brandt, P. Waltereit, U. Jahn et al., phys.stat.sol. a **192**, 5 (2002).

129 D. F. Storm, C. Adelmann, and B. Daudin, J. Appl. Phys. **89**, 2452 (2001).

130 D. F. Storma), C. Adelmann, and B. Daudin, Appl.Phys.Lett **79**, 1614 (2001).

131 A. Dussaigne, B. Damilano, N. Grandjean et al., J.Cryst.Growth **251**, 471 (2003); C. Adelmann, R. Langer, E. Martinez-Guerrero et al., J. Appl. Phys. **86** (8), 4322 (1999).

132 A. Tabata, A.P. Lima, L.K. Teles et al., Appl. Phys. Lett. **74** (3), 362 (1999).

133 N. Ridley, J. Less-Common metals **8**, 354 (1965).

134 T. Böttcher, S. Einfeldt, V. Kirchner et al., Appl. Phys. Lett. **73**, 3232 (1998).

135 E. S. Jeon, V. Kozlov, Y. K. Song et al., Appl. Phys. Lett. **69**, 4194 (1996).

136 I. L. Krestnikov, N. N. Ledentsov, A. Hoffmann et al., Phys. Rev. B **66**, 155310 (2002).

137 Y.-T. Moon, D.-J. Kim, J.-S. Park et al., Appl. Phys. Lett. **79**, 599 (2001).

138 J. Neugebauer, T. K. Zywietz, M. Scheffler et al., Phys. Rev. Lett. **90**, 056101 (2003).

139 F. Widmann, B. Daudin, G. Feuillet et al., Appl.Phys.Lett **73**, 2642 (1998).

140 X. Q. Shen, M. Shimizu, and H. Okumura, Jpn. J. Appl. Phys. **41**, L873 (2002).

141 G. Feuillet, H. Hamaguchi, H. Okumura et al., Materials Science and Engineering B **59**, 80 (1999).

142 T. Zywietz, J.Neugebauer, M. Scheffler et al., MRS Internet J. Nitride Semicond. Res **3**, 26 (1998).

143 Guido Mula, C. Adelmann, S. Moehl et al., Phys. Rev. B **64**, 195406 (2001).

144 S. Srinivasan, R. Liu, F. Bertram et al., phys.stat.sol. b **228**, 41 (2001).

145 S. Pereira, M.R. Correia, E. Pereira et al., Mater. Sci. Eng. B **93**, 163 (2002).

146 K. P. O'Donnell, P. G. Middleton, C. Trager-Cowan et al., Appl.Phys.Lett **73**, 3273 (1998).

147 A. Nakadaira and H. Tanaka, phys. stat. sol. (a) **176**, 529 (1999).

148 J. H. Van der Merwe, J. Appl. Phys. **34**, 123 (1962).

149 A.Fisher, H. Kühne, and H. Richter, Phys. Rev. Lett. **73**, 2712 (1994).

150 S. Pereira, M. R. Correia, E. Pereira et al., Appl.Phys.Lett **81**, 1207 (2002).

151 A. Krost, G. Bauer, and J. Woitok, in *Optical characterization of epitaxial semiconductor layers*, edited by W. Ritcher (Springer, 1996).

152 V. Lemos, E. Silveira, J.R. Leite et al., Phys. Rev. Lett. **84**, 3666 (2000).

153 E. Silveira, A. Tabata, J.R. Leite et al., Appl. Phys. Lett. **75** (23), 3602 (1999).

154 A. Tabata, J. R. Leite, A. P. Lima et al., Appl. Phys. Lett. **75**, 1095 (1999).

155 D.G. Pacheco-Salazar, S.F. Li, F. Cerdeira et al., submitted to J. Crytal Growth.

156 F. Cerdeira, C. J. Buchenauer, F. H. Pollak et al., Phys. Rev. B **5**, 580 (1972).

157 F. Cerdeira, A Pinczuk, J. C. Bean et al., Appl. Phys. Lett. **45**, 1138 (1984).

158 M. Hünermann, W. Richter, J. Saalmüller et al., Phys. Rev. B **34**, 5381 (1986).

159 S.F. Chichibu, K. Wada, J. Müllhäuser et al., Appl. Phys Lett. **76** (13), 1671 (2000).

160 L. Bellaiche, T. Mattila, L.-W. Wang et al., Appl. Phys. Lett. **74** (13), 1842 (1999).

161 F. Bernardi and V. Fiorentini, Phys. Rev. B **57**, R9427 (1998).

162 C. Wetzel, T. Takeuchi, H. Amano et al., J. Appl. Phys. **85** (7), 3786 (1999).

163 L.K. Teles, J. Furthmüller, L.M.R. Scolfaro et al., Phys. Rev. B **62** (4), 2475 (2000).

164 P. Yu and M. Cardona, *Fundamental of Semiconductor: Physics and Materials Properties*. (Springer, Germany, 1996).

165 O. Husberg, A. Khartchenko, D.J. As et al., Appl. Phys. Lett. **79** (9), 1243 (2001).

166 J.R.L. Fernandez, O.C. Noriega, J.A.N.T. Soares et al., Solid State Communications **125** (3-4), 205 (2003).

167 Harris G, *Properties of Silicon Carbide*. (INSPEC publication, 1995).

168 T. Yamada and K.M. Itoh, Mat. Sci. Forum **389-393**, 675 (2002).

169 A. Tabata, L.K. Teles, T. Frey et al., presented at the 25 Intern. Conf. Phys. Semicond., Osaka/Japan, 2000 (unpublished).

170 R. Goldhahn, J. Scheiner, S. Shokhovets et al., Appl. Phys. Lett. **76** (3), 291 (2000).

171 M.E. White, K.P. O'Donnell, R.W. Martin et al., Mater. Sci. Eng. B **93**, 147 (2002).

172 S.F. Li, D.J. As, K. Lischka et al., Mater. Res. Soc. Symp. Proc. **831**, E8.15.1 (2005).

173 K. P. O'Donnell, R. W. Martina, C. Trager-Cowana et al., Mater. Sci. Eng. B **82** (194) (2001).

174 K.P. O'Donnell, I. Fernandez-Torrente, P.R. Edwards et al., J.Cryst.Growth **269**, 100 (2003).

175 T. L. Tansley and C. P. Foley, J. Appl. Phys. **59**, 3241 (1986).

176 S. Yamaguchi, M. Kariya, S. Nitta et al., Appl. Phys Lett. **76**, 876 (2000).

177 S. F. Chichibu, M. Sugiyama, T. Kuroda et al., Appl.Phys.Lett **79**, 3600 (2001).

178 R. Goldhahn, J. Scheiner, S. Shokhovets et al., Appl.Phys.Lett **76** (3), 291 (2000).

179 J. Müllhäuser, O. Brandt, A. Trampert et al., Appl. Phys. Lett. **73** (9), 1230 (1998).

180 S.F. Chichibu, M. Sugiyama, T. Onuma et al., Appl. Phys. Lett. **79** (26), 4319 (2001).

181 D.G. Pacheo-Salazar, F. Cerdeira, E.A. Meneses et al., J. Appl. Phys., (submitted) (2004).

182 Y.T. Moon, D.J. Kim, J.S. Park et al., Appl. Phys. Lett. **79**, 599 (2001).

183 Q. Li, S. J. Xu, W. C. Cheng et al., Appl.Phys.Lett **79**, 1810 (2001).

184 Y. P. Varshni, Physica **34**, 149 (1967).

185 Y. P. Sun, Y. H. Cho, E.-K. Suh et al., Appl. Phys Lett. **84**, 49 (2003).

186 S.-W. Feng, E. -C. Lin, T.-Y. Tang et al., Appl.Phys.Lett **83** (19), 3906 (2003).

187 M. D. McCluskey, L. T. Romano, B. S. Krusor et al., Appl.Phys.Lett **72**, 1730 (1998).

188 R. Singh, D. Doppalapudi, T. D. Moustakasa et al., Appl.Phys.Lett **70**, 1089 (1996).

189 S. L. Chuang and C. S. Chang, Semicond. Sci. Technol. **12**, 252 (1997).

190 S. Chichibu, T. Azuhata, T. Sota et al., Appl. Phys Lett. **69**, 4188 (1996).

191 F. D. Sala, A.D. Carlo, P. Lugli et al., Appl.Phys.Lett **74** (14), 2002 (1999).

192 S. Pereira, M. R. Correia, E. Pereira et al., Phys. Rev. B **64**, 205311 (2001).

193 D. Gerthsen, B. Neubauer, A. Rosenauer et al., Appl. Phys Lett. **79** (16), 2552 (2001).

194 S.Patthast.

195 E. F. Schubert, Y. -H. Wang, A. Y. Cho et al., Appl.Phys.Lett **60** (8), 921 (1991).

196 F. De Martini, G. Innocenty, G. R. Jacobovitz et al., Phys. Rev. Lett. **59**, 2995 (1987).

197 H. Yokoyama, K. Nishi, T. Anan et al., Appl. Phys Lett. **57**, 2184 (1990).

198 F.B.Naranjo, S.Fernándenz, M.A.Sánchez-García et al., Appl.Phys.Lett. **80**, 2198 (2002).

199 S. Fernandez, F. B. Naranjo, F. Calle et al., Semicond. Sci. Techn. **16**, 913 (2001).

200 H. E. Shin, Y. G. Ju, H. W. Song et al., Appl.Phys.Lett **72**, 2205 (1998).

List of publications

1. **Shunfeng Li,** Donat J. As, Klaus Lischka, "*The influence of the metal fluxes on the composition of cubic InGaN*", to be submitted.

2. **Shunfeng Li**, J. Schörmann, A. Pawlis, D. J. As, K. Lischka "*Cubic InGaN/GaN multi-quantum wells and AlGaN/GaN Bragg reflectors for application in resonant cavity LEDs*", Microelectronics Journal, Vol. **36**, 963(2005)

3. **S. F. Li,** D. J. As, K. Lischka, D. G. Pacheco-Salazar, J. R. Leite, F. Cerdeira, E. A. Meneses, "*Strong room temperature 510nm emission from cubic InGaN/GaN multiple quantum wells*''. MRS Symp. Proc. Vol. **831**, (2005) E.8.15.1

4. D. G. Pacheco-Salazar, **S. F. Li**, F. Cerdeira, E. A. Meneses, J. R. Leite, L. M. R. Scolfaro, D. J. As, K. Lischka, "*Growth and characterization of cubic InxGa1-xN epilayers on two different type of substrates*", J. Crystal Growth (in press).

5. **Shunfeng Li**, Jörg Schörmann, Alexander Pawlis, Donat J. As, and Klaus Lischka. "*Cubic InGaN/GaN multiple quantum wells and AlGaN/GaN Bragg reflectors for green resonant cavity LED* ". Proceedings of 13th semi-conducting and insulating materials conference, 2004, Beijing, China.

6. D. G. Pacheco-Salazar, F. Cerdeira, E. A. Meneses, J. R. Leite, **S. F. Li**, D. J. As, K. Lischka "*Optical measurement on c-InGaN layers deposited on SiC substrates*", submitted to J. Appl. Phys.

7. A. Montaigne Ramil, K. Schmidegg, A. Bonanni, H. Sitter, D. Stifer, **Li Shufeng**, D. J. As, K. Lischka. "*In situ growth monitoring by spectroscopy ellipsometry of MOCVD cubic GaN (001)*". Thin solid films, **455-456**, 684(2004).

8. B. Qu, **S. F. Li**, G. X. Hu, X. H. Zheng, Y. T. Wang, S. M. Lin, Hui Yang, J. W. Liang, "*Surface roughness and high density of twins and hexagonal inclusions in cubic GaN epilayers*", Science in China A, **44**, 796(2001).

9. Xu Zhongying, Liu Baoli, **Li Shunfeng**, Yang Hui, Ge Weikun. "*Steady and transient optical properties of cubic InGaN epilayers*" J. Infrared Millim. Waves. **19**, 11 (2000).

10. **S. F. Li**, Hui Yang, D. P. Xu, D. G. Zhao, X. L. Sun, Y. T. Wang, S. M. Zhang "*Growth of high quality cubic phase InGaN films*", Chinese journal of Semiconductor, **22**, 6 (2000)

11. **S. F. Li**, Hui Yang, D. P. Xu, S. M. Zhang, D. G. Zhao. "*Electrochemical C-V measurement of cubic phase GaN LED*", The seventh national conference proceedings on thin solid films, Oct, 2000.

12. Hui Yang, Shuming Zhang, Dapeng Xu, **Shunfeng Li**, Degang zhao,Yi Fu,Yuanping Sun, "*MOCVD Growth of Cubic GaN: Materials and Devices*", Invited talk at IWN2000, Nogoya, Japan.

13. Dapeng Xu, Hui Yang, D. G. Zhao, **S. F. Li**, Y. T. Wang and R. H. Wu, "*Room temperature optical transition in Mg-doped cubic GaN/GaAs (100) by MOCVD*", J. Appl. Physics Communication. **87**, 2064(2000)

14. Dapeng Xu, Hui Yang, **S. F. Li**, D. G. Zhao, H. Ge, R. H. Wu, "*Pulsed excimer laser annealing of Mg-doped cubic GaN*", J. Crystal Growth, **209**, 203(1999).

15. Dapeng Xu, Hui Yang, J. B. Li, **S. F. Li**, Y. T. Wang, D. G. Zhao, R. H. Wu, "*Effect of Si doping on cubic GaN films grown on GaAs (001)*", J. Crystal Growth, **206**, 150-154(1999).

Acknowledgements

The last page of my thesis is written, but I can still remember the hard times when I worked with this topic. The things, which impressed me most during last three and half years is the help, encouragement and advice from my friends and colleagues. Because of that, I would like to express my acknowledgments here.

Firstly, I would like to thank Prof. Dr. K. Lischka who gave me the opportunity to work in this group. My work was perfomed under his direct supervision. Plenty of valuable discussions and advices from him support this chanllenging work on the research of cubic InGaN.

The same gratitude goes to Apl. Prof. Dr. D. J. As, who has also given a lot of good advices and knowledge. Thanks also go to Dr. D. Schikora for his help and discussion about the growth.

Part of my work comes from the successful collaboration with Prof. J. R. Leite's group in Sao Paulo university of Brasil and Prof H. Sitter's group in Linz Univeristy of Austria. I would like to acknowledge the people from these two groups for their valuable work and discussion, especially Dr. D. G. P. Salazar, Prof. F. Cerdeira, Prof. J. R. Leite in Sao Paulo University and Dr. K. Schmidegg, Dr. A. Bonanni, Prof H. Sitter in Linz University.

I am also very grateful to the optoelectronic staff, B. Volmer, I. Zimmermann, S. Igges for their technical and bureaucratical help. This kind of work is quite a problem for a foreign student, I guess. I am one case.

My thanks also go to my colleagues, the Ph.D students, O. Husberg, S. Potthast, J. Schörmann, C. Arens, S. Preuss, and Dr. A. Pawlis, who helped with discussing the results, which mostly leading good ideas for my further work. My gratitude also goes to my former colleagues, Dr. M. Bartels, Dr. A. Kharchenko, Dr. U. Köhler for their help when I started my work. I would like also thank the diploma student M. Schnietz, Master student, M. Panfilova for their valuable work. I am also grateful for the work of visit student, M.Sc E. Decuir on reading and correcting my thesis.

I would like thank my friends, Dirk and Angelina Wehling for their warm-heartedly help during last three years.

Morever, I want to thank my wife, Jia Yang. Her love, encouragement helped me go through many difficulties during my work.

There are still many friends around whom I cannot all mention due to the limited page. I want to say thanks to all of them here.

At last but not least I would like express my thanks to my and my wife's parents for their love and support during my studying.

In memory of my grandmother

Curriculum Vitae

Name:	Shunfeng Li
Gender:	Male
Birthday and place:	Feb. 11, 1974; Hebei, P. R. China
Marital status:	Married

Education

1980 – 1986	Junior school “6.1” junior school, in 1980 – 1985. Mashi Street junior school, in 1985-1986
1986 - 1989	Middle school The 4th middle school of Xingtai
1989 - 1992	The 1st high school of Xingtai.
1992 - 1997	Study in Beijing University, Physics department.
1997	Bachelor of Science
1997-2001	Master student in Institute of semiconductors, Chinese Academy of Sciences. Supervised by Prof. H. Yang
2001	Master of Engineering.
2001-2005	Ph.D student and Wiss. Mitarbeiter in Universität Paderborn. Supervised by Prof. Dr. K. Lischka